Durham University

Durham E-Theses

Aspects of, and new approaches to, the design of direct drive generators for wind turbines

Gordon, Paul

How to cite:

Gordon, Paul (2004) *Aspects of, and new approaches to, the design of direct drive generators for wind turbines*, Durham theses, Durham University. Available at Durham E-Theses Online: http://etheses.dur.ac.uk/1741/

Use policy

The full-text may be used and/or reproduced, and given to third parties in any format or medium, without prior permission or charge, for personal research or study, educational, or not-for-profit purposes provided that:

- a full bibliographic reference is made to the original source
- a link is made to the metadata record in Durham E-Theses
- the full-text is not changed in any way

The full-text must not be sold in any format or medium without the formal permission of the copyright holders.

Please consult the full Durham E-Theses policy for further details.

Academic Support Office, Durham University, University Office, Old Elvet, Durham DH1 3HP
e-mail: e-theses.admin@dur.ac.uk Tel: +44 0191 334 6107
http://etheses.dur.ac.uk

Aspects of, and New Approaches to, the Design of Direct Drive Generators for Wind Turbines

Paul Gordon

A copyright of this thesis rests with the author. No quotation from it should be published without his prior written consent and information derived from it should be acknowledged.

A Thesis presented for the degree of
Doctor of Philosophy

New and Renewable Energy Group
School of Engineering
University of Durham
England

2004

1 3 JUL 2004

Aspects of, and New Approaches to, the Design of Direct Drive Generators for Wind Turbines

Paul Gordon

Abstract

This thesis investigates the design and construction of permanent magnet direct drive generators for large wind turbine applications. Present generator structures are large diameter to give a reasonable airgap speed, and are strong enough to withstand substantial airgap magnetic forces. This can result in large, heavy and costly direct drive machines.

The effect of the build up of tolerances on the balance of magnetic forces in a direct drive double airgap machine is investigated.

Two main approaches to the design and construction of these machines are proposed and considered. The Segmental Electrical Machine (SEM) combines modularity and the use of laser cut plate to reduce manufacturing cost and improve transportation for an iron cored direct drive machine. The Spoked Lightweight Machine (SLiM) uses a lightweight structure and an ironless stator, with less serious magnetic force issues, to give drastic reductions in weight.

Declaration

The work in this thesis is based on research carried out in the New and Renewable Energy Group, School of Engineering, University of Durham, England. No part of this thesis has been submitted elsewhere for any other degree or qualification and it all my own work unless referenced to the contrary in the text.

Copyright © 2004 by Paul Gordon.

"The copyright of this thesis rests with the author. No quotations from it should be published without the author's prior written consent and information derived from it should be acknowledged".

"Please accept my resignation. I don't want to belong to any club that will accept me as a member"

Groucho Marx (1895-1977)

Acknowledgements

Many people have helped me out whilst I've been writing this thesis.

Thanks to:

Ed Spooner, for giving me the opportunity, Jim Bumby, for taking over the supervision, and both of them for their technical help and nagging.

Markus Mueller, Peter Tavner and the rest of the NaREG for general help and a friendly working atmosphere.

Roger Little, Ted Jones, Brian Blackburn, Colin Wintrip, Bernie McEleavey, Trevor Nancarrow, Mike Wilson and the other mechanical, electronic and civil workshop technicians, for all their work and advice on various bits of hardware.

Many good friends too numerous to mention but especially Kath Kulczyk, Steve Anderton, Grant Ingram, Nick Baker, Dilshat Djumanov and Rachel Freer, for their support, advice, nonsense, great cooking, good company and flavoured vodka.

Stuart Barnett for taking the mickey.

The Gordons: Mum, Dad, Andy, Matt, Jan, Clare, Alan, John, Wendy, for all their support and encouragement.

Contents

Declaration **iii**

1 Introduction **1**

1.1 Wind Power 1

1.2 Wind Turbine Technology 1

1.3 Direct Drive 2

1.4 Scope of Thesis 4

2 Segmental Construction of an Electrical Machine **6**

2.1 Modular Electromagnetic Construction 6

2.2 Segmental Construction of Modular Machines 7

2.3 Laser-Cut Plate 9

2.4 Tolerance Chains 9

2.5 Test Machines 11

2.5.1 1st Linear Prototype (LP1) 13

2.5.2 2nd Linear Prototype (LP2) 13

2.5.3 Fishplates and Splitting the Machine 15

2.5.4 Access for Splitting Machine 17

2.5.5 Circular Prototype 18

2.5.6 Assembly Procedure 19

2.6 Discussion & Conclusions 21

3 Double Airgap Machines **22**

3.1 Experimental Rig 22

3.2 Experimentation 24

3.3 Experimental Errors 30

3.4 Biot-Savart model of the airgap-closing forces 31

3.5 Discussion & Conclusions 35

3.5.1 Magnetic Forces 35
3.5.2 Influence on Machine Structure 38

4 Ironless Stator SLiM **39**
4.1 Bicycle Wheels 39
4.2 SLiM Structural Configuration 42
4.3 Torque Force Models 47
4.4 Rim Design 51
4.4.1 Wheel Buckling 52
4.5 Aerodynamic Forces 53
4.6 Ironless Stator Field-Current Interaction Forces 55
4.6.1 2D Analysis 56
4.6.2 3D Analysis 63
4.6.3 Estimate of Net Radial Force 67
4.7 Discussion & Conclusions 67

5 Ironless Stator Electromagnetics **69**
5.1 2D Analytical Model of the Magnetic Field 69
5.2 3D Analytical Model of the Magnetic Field 74
5.3 Convergence of Models 80
5.4 Experimental Measurement of Magnetic Field 85
5.4.1 Sensor Position Within Probe 86
5.5 Discussion & Conclusions 87

6 SLiM1 Prototype **91**
6.1 Design 91
6.2 Rotor Back Iron Thickness 95
6.3 Open Circuit Voltage, V_{oc} 98
6.3.1 Open Circuit Voltage Measurements 98
6.3.2 Open Circuit Voltage Modelling 98
6.4 Inductance 102
6.5 Power Measurements 105
6.6 Discussion & Conclusions 107

7 Case Study **109**
7.1 Model Summary 110
7.2 Discussion & Conclusions 111

8 Conclusions & Further Work **114**

8.1 Conclusions 114

8.2 Further Work 115

References **117**

Chapter 1

Introduction

1.1 Wind Power

The use of wind turbines to produce electricity is seen as a remedy for a wide range of electricity related issues including concerns about operational safety and waste disposal of nuclear power, man-made climate change (the 'Greenhouse Effect') and the Kyoto agreement, local air quality issues, fossil fuel depletion, energy security of supply, and the catch-all, 'sustainability'.

Whatever the details that define it, and including consideration of various limiting factors, be they economic, technical or environmental, the global potential for electricity production from wind turbines is huge. Both on-shore and off-shore wind energy potentials are of the order of current world energy consumption.

Wind turbines installed to date capture only a tiny fraction of this potential, although the industry is expanding quickly. During 2002, global installed capacity grew by 30% to 32GW [1], nearly exclusively on-shore. Most development is taking place in Europe, where off-shore is receiving a lot of interest. Already several pilot off-shore farms have been operating for several years, and in the UK, with some of the best off-shore and on-shore wind resources and other favorable factors, an initial 13 sites are being licensed in English and Welsh waters totalling 1.5GW capacity [2].

1.2 Wind Turbine Technology

Windmills have been used for thousands of years and originate from the Near and Middle East. More than 200,000 wooden-sailed horizontal axis windmills were constructed in North-West Europe prior to the Industrial Revolution, and in the USA

eight million wind pumps had been installed by the end of the 1930s. The first significant use of wind turbines for electricity generation was the installation of around 15,000 wind turbines in California during the first half of the 1980s, and since then there has been growth of wind turbine use in many parts of the world.

There are a multitude of designs for wind machines and for modern wind turbines including Darrieus, Savonius, H-VAWT, V-VAWT (all vertical axis machines), multi-rotor concepts (ie shared tower), diffuser-concentrators, and horizontal axis machines with any number of blades from 1 upwards. The vast majority of commercial designs have been 3 bladed, upwind, geared, horizontal axis machines, although direct drive machines are capturing significant market share at present. Wind turbine size has grown very quickly, from around 50-100kW during the early 1980s to 200kW in the early 1990s, to 3MW and beyond nowadays. These largest machines are partly being developed with the off-shore market in mind.

1.3 Direct Drive

The first commercial wind turbines used electrical generators that were simply adapted from the designs that existed for other applications. As the wind industry grows, generators are evolving in order to meet the specific demands of the sector. One major shift in generator design has been from geared (high speed) to direct drive (low speed).

Direct drive generators have an increased radius to gain the benefits of a higher airgap speed, and a decreased axial length. They tend to have a high level of integration with the hub structure that supports the wind turbine blade roots.

Direct drive wind turbine systems have been very successful to date. For example Enercon, a German manufacturer of direct drive wind turbines systems, has had a considerable portion of market share in recent years. However, as wind turbines scale up to multi-MW sizes, direct drive generators are becoming exceptionally heavy and large, leading to problems during construction, transportation and installation, and impacting on the rest of the wind turbine structure due to their contribution to tower top weight.

Enercon's larger wind turbines are good examples of the state of the art for multi-MW sizes. Their 2MW E66 wind turbine has a 5m diameter direct drive generator with it's rotor integrated into the turbine rotor hub. There are no published figures on the generator weight alone, but the nacelle weight is 95t which is 50% more than geared machines of the same power ratings. The generator weight alone has been

estimated to be 70t [3], which can be compared with the 25t geared generator of the NEG-Micon 2.75MW wind turbine. Enercon has been testing it's 4.5MW E112 wind turbine for some time now. The generator is 10m diameter, and the tower top weight is 500t. However, this is rumoured to be a derated 6MW machine. Another example of a large direct drive generator is the one for the (almost) commercial Zephyros 1.5MW Z72. The generator is 4m diameter and weighs 50t.

With the scaling up continuing past these existing sizes, construction of these large machines would require high roofed workshops and large capacity cranes, limiting the use of existing fabrication facilities due to these specialised requirements, and would likely result in new dedicated manufacturing and assembly plant. Any design where the coils need installing on the machine before vacuum-impregnation then requires a huge vacuum impregnator, such as that employed by Enercon.

Transportation requires good factory site access, special transport vehicles, police escort, road closures, and journey distances many times the straight line distance. For off-shore, land transportation could be avoided by manufacturing/assembling on the dock side, but this has obvious drawbacks. From the dock to the off-shore site in general the bigger the component, the more expensive the vessel required to shift it, and the bigger the crane required to load it. Furthermore, the majority of generators built would be for export and shipping overseas is a complex and costly operation unless the parts can be fitted into a standard container.

Generally, large cranes have been used to lift the complete tower head assembly onto the top of the tower. On-shore, this requires strong access roads on the site. Off-shore, due to the swell, the top of a crane on a floating vessel would sway too much to be useful, so the vessel has legs to the seabed that it jacks itself up onto. Over the last few years there has been a move towards using cranes mounted on the wind turbine tower top to winch tower head components up eg Zephyros Z72.

Zephyros has also limited it's generator diameter to 4m specifically to aid transportation, whilst Enercon has designed the 4.5 MW E112 generator to allow splitting into quarters for transportation and lifting.

It is normal practice to cast, then machine, the structural components of smaller electrical machines, but this would not be possible at these sizes due to cost of machine tools capable of large diameters. A standard solution to this seems to be to precisely weld the structures together. It is important to note that whilst the large diameter of these generators leads to increased structural weight, it is the strength requirements at this diameter which leads to the large weight. Setting aside strength requirements due to integration with the rotor hub, the strength is required

to withstand the magnetic forces, both torque-producing and airgap-closing forces due to the stator and rotor iron circuit, the latter being a significant factor.

Whilst some of these issues are affected by other aspects of the wind turbine system, the majority lead to costs that will be reflected in the final price of the generator, and in turn to the energy produced.

Finally, for permanent magnet machines with stator and rotor iron. of these huge sizes, rotor threading is a hazardous procedure due to the huge attractive forces present when a complete permanent magnet rotor is presented to a complete stator.

1.4 Scope of Thesis

Chapter 2 reports on the **S**egmental **E**lectrical **M**achine, a novel method of constructing direct drive wind turbine generators, which combines modularity and the use of laser-cut plate in order to reduce manufacturing cost and improve transportation. The work resulted in the successful demonstration of an early-stage design with tolerance variation investigated. It showed the structural strength, and therefore weight, impacts of the airgap closing force, and highlighted the practical problems of creating a constant airgap length when building a machine of this design. These variations in airgap length will lead to the airgap closing forces varying around the machine, exacerbating structural problems. The work involved examination of laser cut plate to establish cutting accuracy and other characteristics, the building of two small rigs to test and compare possible design features and the build-up of tolerances, a plywood prototype to test further design features and finally a 2 metre diameter prototype, which was rotated using a drive motor, to check on tolerances, strength and vibration.

Chapter 3 investigates one possible solution to the generator strength and weight issues which is the use of a double sided airgap so that the magnetic forces cancel. However, experimental work on this arrangement shows that tolerances create large Unbalanced Magnetic Pull (UMP). The test rig uses an arrangement of spring balances and weights to measure and counterbalance the UMP present when a linear section of rotor is moved off-centre from a pair of linear steel stators. The magnetic forces are calculated using Biot-Savart, combined with the method of images.

In Chapter 4 a radical departure from existing designs of direct drive generator is proposed in the form of the **S**poked, **Li**ghtweight, **M**achine structure, named SLiM, used in conjunction with an ironless stator electromagnetic topology. General

design issues are discussed, and calculation techniques are developed to allow a design study in Chapter 7. Without an iron stator the magnetic field is no longer channelled around the coil region, and so the coil current is in the full magnetic field, resulting in various electromagnetic forces. The general characteristics of these forces is investigated here. Due to the novelties of SLiM, there is little literature available.

Chapter 5 presents a novel 3D analytical solution to the field of an ironless stator PM machine, as the 2D solution cannot take account of edge effects which are important in axially short machines. This 3D solution is validated by experimental work which includes variation of magnet thickness, magnet pitch and rotor iron edge effects.

Chapter 6 describes the SLiM1 prototype, and presents calculations developed to model it's electro-magnetics. SLiM1 is a simple demonstration machine built partly from bicycle wheel components, with coils fitted and rectified in pairs onto a DC bus. Open circuit voltage and coil inductance are measured, and models developed for both. Power tests are conducted. Airgap tolerances are measured, and their influence on machine performance examined.

Chapter 7 presents a case study for a 2MW machine, where basic parameters of two alternative SLiM designs are calculated.

Chapter 2

Segmental Construction of an Electrical Machine

A design and construction scheme was devised which addresses some of the problems of building direct-drive wind turbine generators by taking the modular electromagnetic approach of [4],[5] and extending it into the structural design, called the Segmental Electrical Machine [6], [7]. The aim of the work was to show that the use of accurately laser-cut flat plates can form the basis for the construction of a dynamic structure. Laser-cut plate is available in ever increasing thicknesses at low cost, and can be ordered and delivered in a few days, and bolted together to form the machine. Consequently, machine tools of extremely large capacity are not essential for the construction of the very large diameter generators required. Furthermore, it is possible to design the machine so it can be split into subassemblies for ease of transportation and installation, being reassembled at a convenient location eg on-site, or perhaps at the tower top, thereby avoiding many of the problems outlined in section 1.3. These two themes, of segmental construction and use of laser cut plate, were focussed on, so no magnetic analysis was undertaken. Also, partly as no coils were fitted to the stator structure, mechanical resonances were not investigated.

2.1 Modular Electromagnetic Construction

Fig.(2.1) shows the modular construction of the electromagnetic generator parts, previously developed at Durham, which allows a large proportion of the generator to be constructed from smaller modules. It's advantages over conventional designs include ease of construction, low maintenance, size and weight. The modules can be used to construct a whole range of generator sizes. This modular concept can be

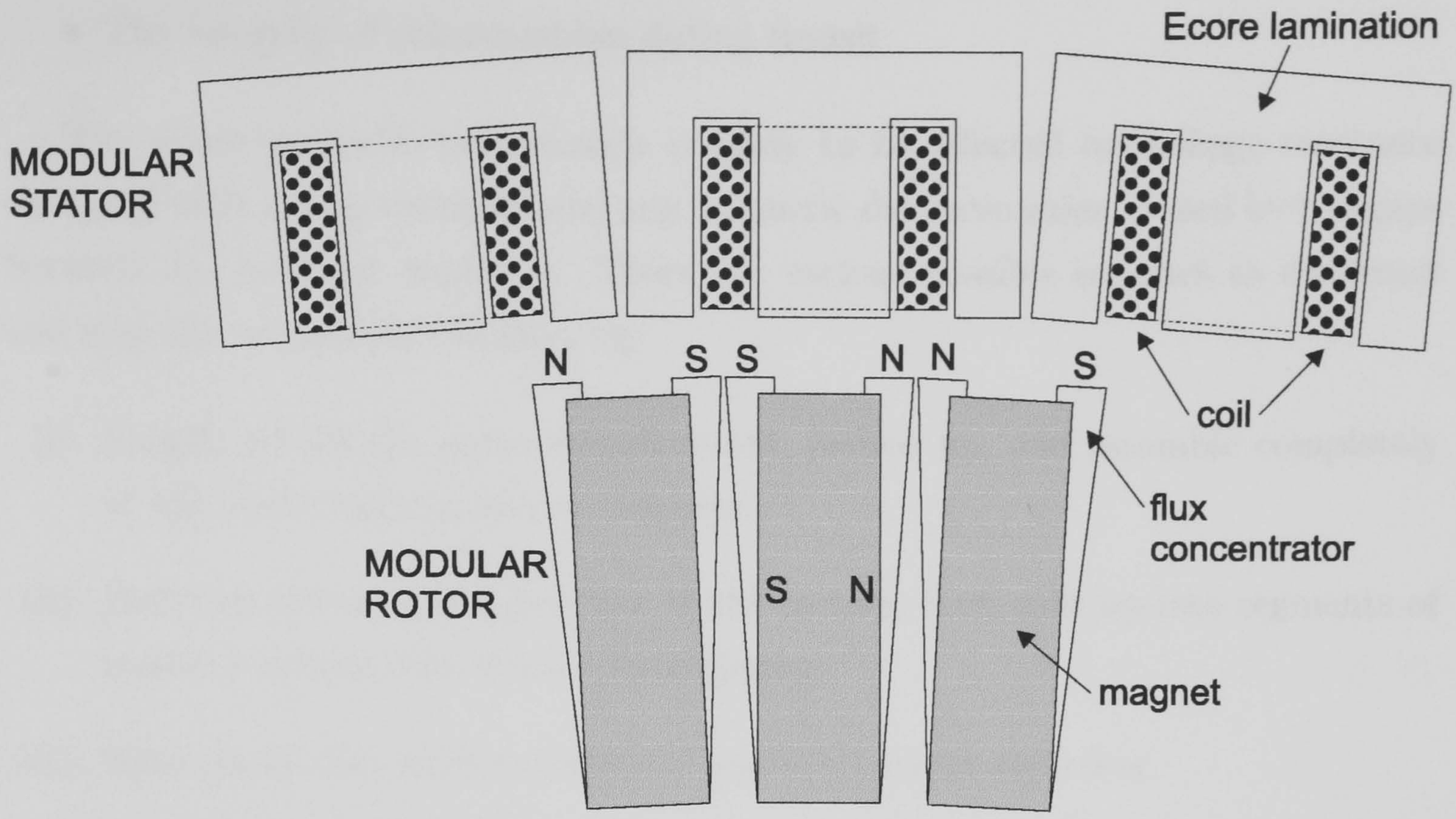

Figure 2.1: Modular Construction

used on the largest forseeable wind turbine generator sizes.

The modular concept demonstrates that it is possible to build the electromagnetic parts of a machine from discrete components, but the structural members of the generator are still machine diameter in size. However, the modular concept can be extended into the structural elements, using segmental construction.

2.2 Segmental Construction of Modular Machines

In designing a large generator to be assembled from a number of subassemblies, the following practical mechanical details must be considered:

- Design for assembly from parts which can be made by laser cutting
- Design for ease of assembly at the foot of the tower or, preferably, after lifting
- The accumulation of tolerances leading to random errors in the airgap
- The overall structural stiffness in resisting the airgap forces
- Magnetic forces during assembly between adjacent subassemblies
- Magnetic forces during transportation

- The integrity of subassemblies during transit

The electromagnetic performance is likely to be affected by leakage reactance changing with airgap variation and any magnetic discontinuities caused by the gaps between the laser-cut segments. There are various possible schemes to construct and ship the sections of machine, eg:

(i). Simply get all the parts manufactured, packed up, and assemble completely at the tower head,on-site or near-site.

(ii). Build up the complete machine in the factory, then split up into segments of stator and segments of rotor for shipping

(iii). Same as (ii) but with segments of combined stator and rotor.

Scheme (i) would create a huge amount of assembly out of the workshop environment, and with hundreds of small parts, and many more bolts. This would also be an issue for QA and machine testing. Schemes (ii) and (iii) involve some duplication of effort ie building up completely, splitting into segments, and then re-combining on/near site. Scheme (iii) was chosen because the rotor segment fits nicely into the stator segment, and the airgap is kept intact with magnets on one side and Ecores on the other. This almost completely contains the very large magnetic forces from the permanent magnets, which would cause large problems for transportation and re-assembly, without the need for adding magnetic keepers. Separating the two for transportation and then recombining would lead to similar problems as encountered with rotor threading.

The structural topology of most proposed types of direct drive generator uses a stator supported in a single bearing cantilever fashion which is believed to be necessary to reduce machine length and complexity, so this feature was adopted for the segmental machine. This is particularly vulnerable to distortion due to the attractive force across the airgap. This force is affected by the tolerance of the airgap.

At the time of the work, large hydro-electric generators were the only generators known to the author that are constructed and shipped in several parts, to be combined during installation. These correct the airgap length using shims.

2.3 Laser-Cut Plate

At the time of the work, laser cutting was possible from the supplier for plate up to 25mm thick and routinely up to 12mm, in sheets up to 2m x 3m. It competes with a variety of other processes depending on the type of material, tolerance and-or cut quality required and thickness of material. Important characteristics for this application of laser cut plate are the:

- Tolerance of the cut, as this affects airgap tolerance
- Squareness of the cut. If the profile through the plate is too steep there is a possibility of local yielding, and joints would become less stiff, affecting the ability of the structure to resist the magnetic forces
- In-and-out-of-plane distortions, mainly from stress releases from the original cold rolling of the steel. These can create assembly problems and distortions in the assembled machine, the latter increasing tolerances.

General tolerances from the supplier for mild steel of various thickness' are presented in the table within Fig.(2.2). To examine squareness of cut, samples were mounted on a machine tool travelling table and a dial indicator was run over the cut surface at two positions on each sample, see Fig.(2.2). To examine distortion, two thin rings of 10 and 15mm thick plate and about 300mm diameter were laser cut, and then cut through at one point. This sample shape is considered to be the worst possible case. In-plane distortions were up to 3mm for both 10mm and 15mm thick, and up to 1.4mm/2mm for out-of-plane distortions for 10mm/15mm thick.

2.4 Tolerance Chains

Examination of the tolerance chain within a design can show the worst case situation. Consider an existing commercial machine, the 2MW DD-WTG Enercon E-66, which has a generator diameter of about 5m and an airgap length of about 0.6m. Taking account of the maximum plate size of 2m x 3m mentioned previously it would be possible to build this diameter machine from 8 segments, each comprising 2 layers of plates in the radial direction with, for example, 20mm thick plate. If e, the tolerance of each plate, is ± 0.5mm, then the airgap tolerance is $4e(1 + b/a)$, the cantilever design amplifying the stator tolerances and being responsible for the b/a part, see Figure 2.3. Therefore for tolerance purposes a should be large. Large a

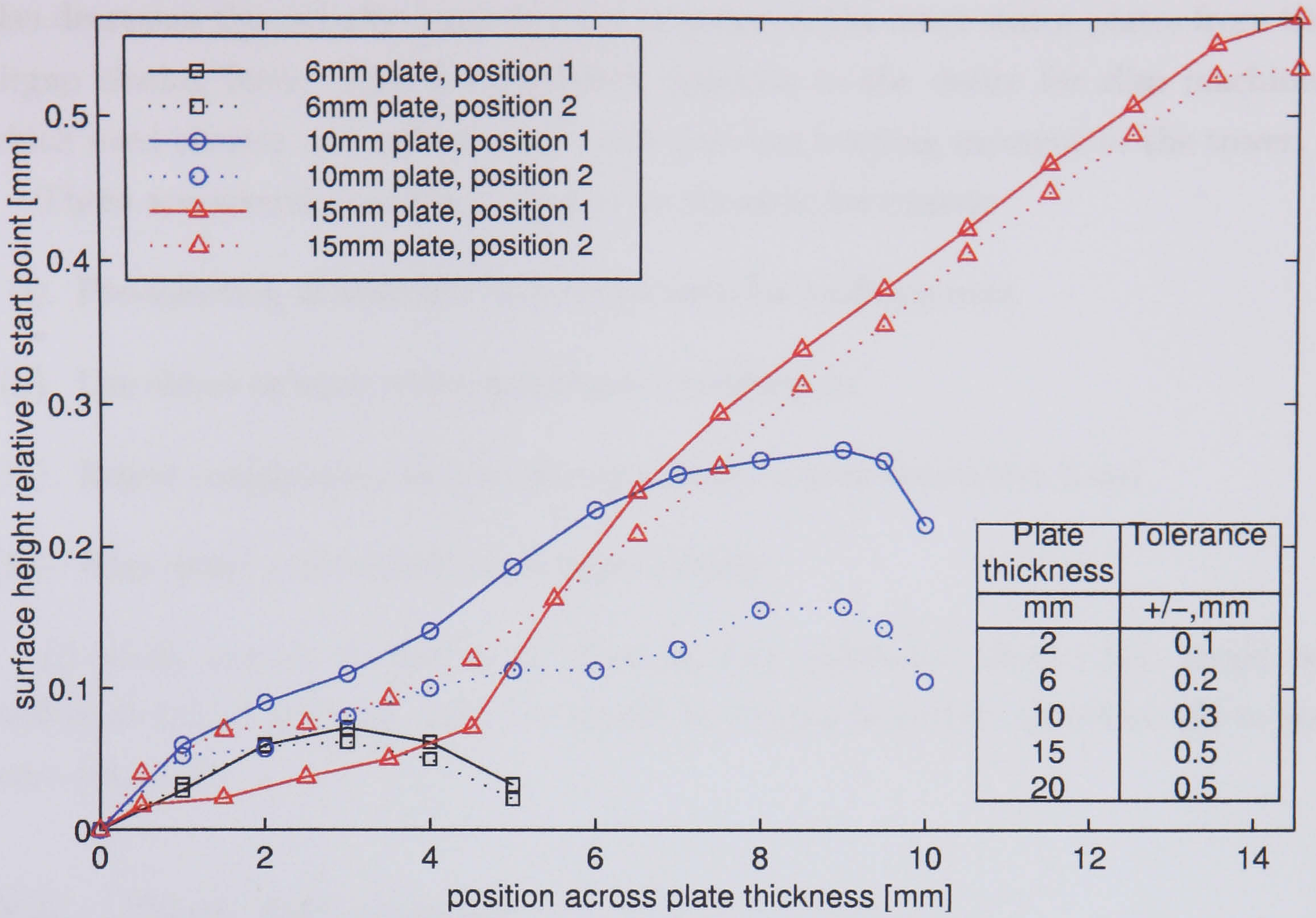

Figure 2.2: Profile across laser-cut edge

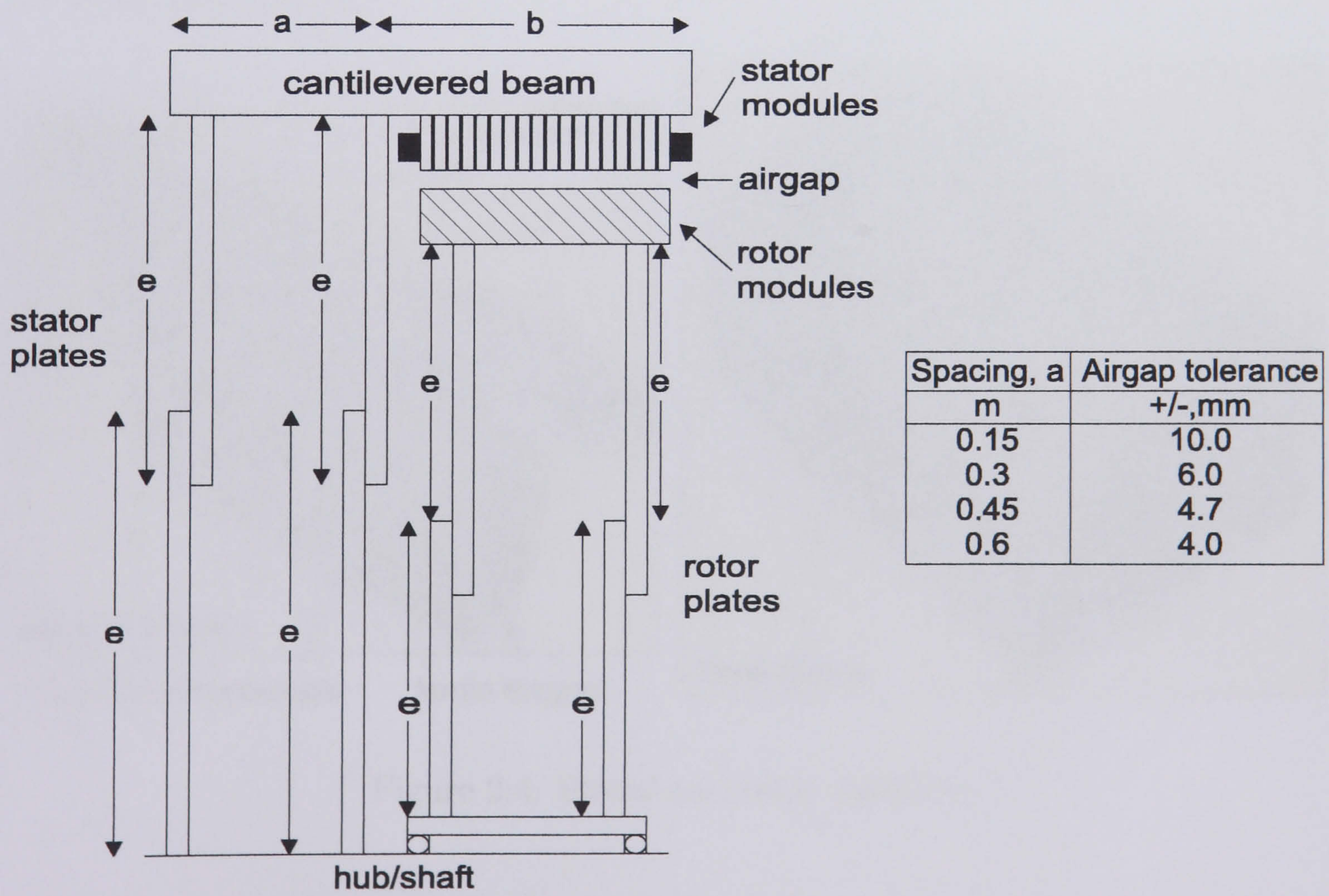

Figure 2.3: Tolerance build-up

also decreases the radially-inwards force pressing on the inner stator plates from the airgap closing force. This is completely opposite to the desire for slim machines which need shorter and lighter shafts and give less bending moment to the tower.

There are several possible strategies to alleviate tolerances:

(i). Pre-selection of matched component sets for each segment

(ii). Use shims or some other adjustment mechanism

(iii). Reject components with tolerance outside a more restrictive band

(iv). Edge grind components after laser-cutting

(i) would require holding a lot of stock, and additional labour, (iii) would be inefficient use of material, and (iv) would be labour intensive, therefore (ii) is the most appealing.

2.5 Test Machines

Various machines have been constructed, all based on the existing rotor and stator modules, see Fig.(2.4).

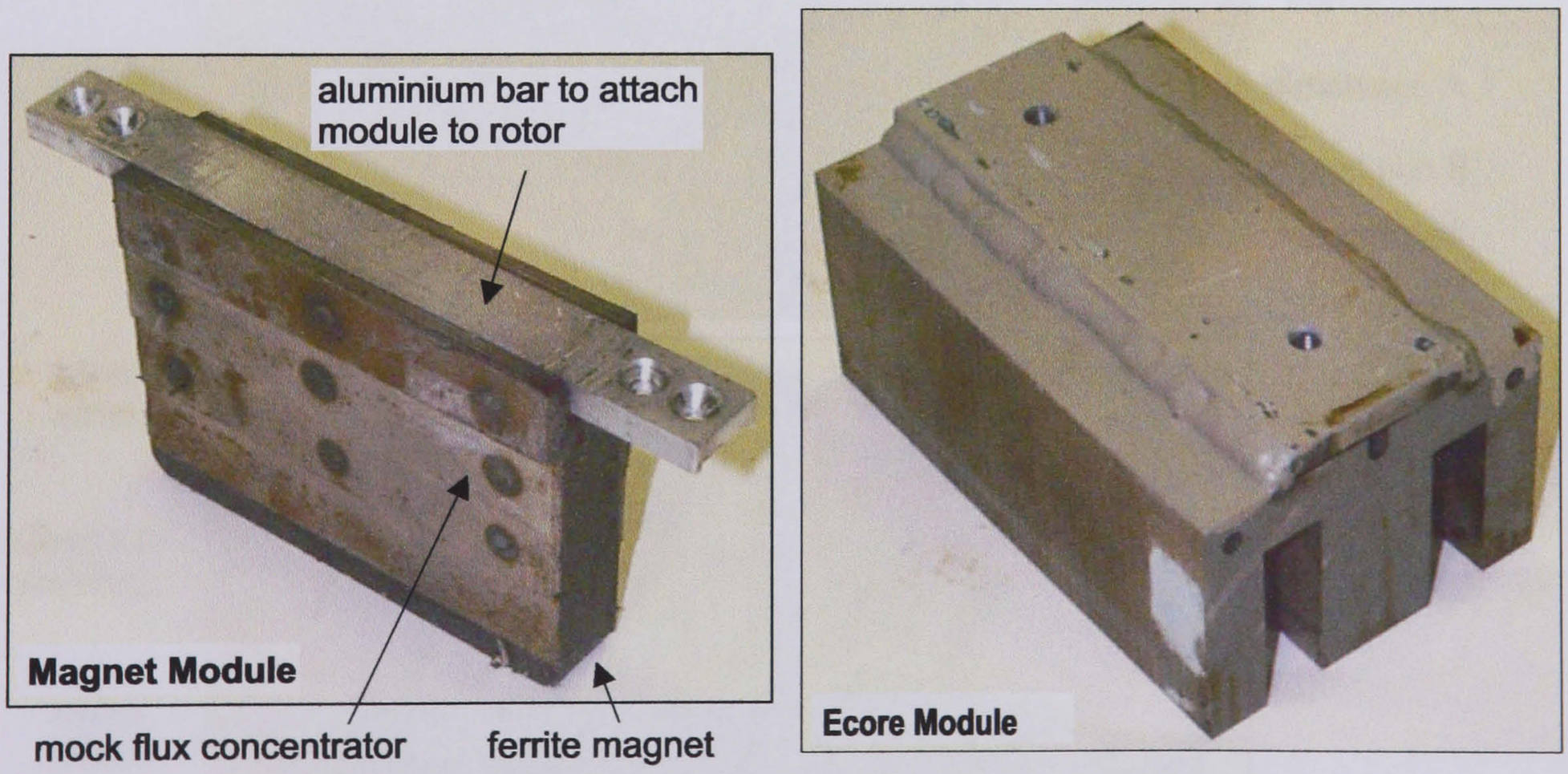

Figure 2.4: Stator and rotor modules

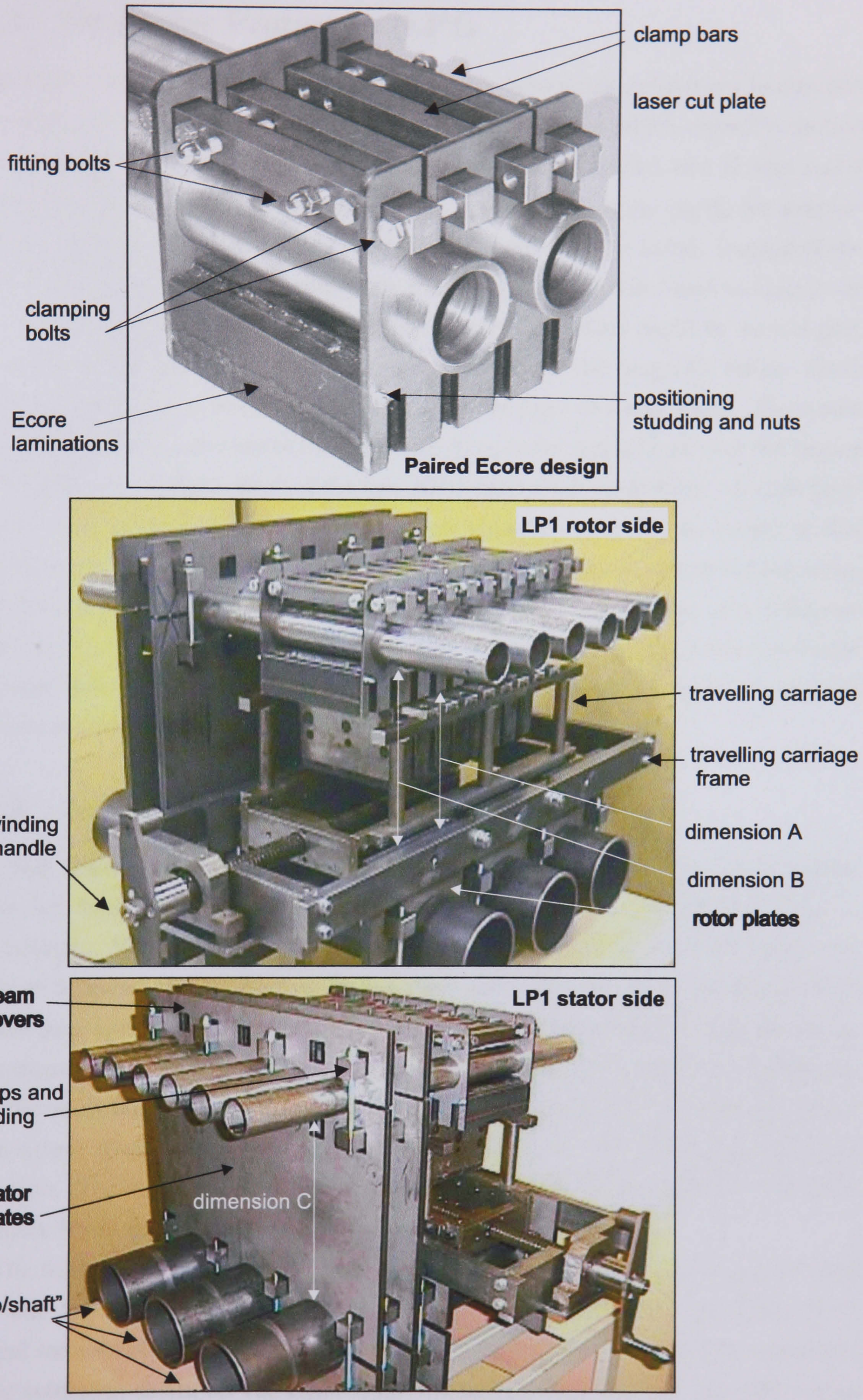

Figure 2.5: LP1

2.5.1 1st Linear Prototype (LP1)

In previous work, mounting single Ecore modules onto single cylindrical beams had been problematic due to twisting from the magnetic forces which caused variation of the airgap, so a new paired design was tried, which coupled two Ecores and 2 mounting beams together, see Fig.(2.5). The machine was linear partly for simplicity, but mainly so that an available travelling carriage could be fitted. Instead of the rotor rotating on a circular machine, the travelling carriage was fitted to stationary rotor plates. Magnets were then added to the carriage, which could be wound past the stator to test how the Ecore module pairs resisted the magnetic forces. Both stator and rotor plates were fitted to large tubes in place of a hub/shaft. The stator laser-cut plates had cut-outs to fit the beams into, cover plates to go over the beams and holes for the clamps. Each of the two stator layers was made from a double layer of 6mm plate because thicker plates had a less square cut, and it was unclear at this stage how stiff the stator would be when resisting the magnetic airgap-closing force. Extensive measurements were made of the machine in the manner of a tolerance chain, but vertical movement on the travelling carriage running rails was discovered at a later date, invalidating much of it. However, the remaining valid data indicated tolerances depended partly on the fitting of the beams.

2.5.2 2nd Linear Prototype (LP2)

The 2nd machine used skimmed, and therefore more accurate, beams to isolate errors due to the laser cutting, and single layers of 6mm plate which proved to be stiff enough. Various design alterations were tried, and then measurements were made at 3 places on the machine to see their effect on tolerances, see Fig.(2.5) to see the location of these dimensions on the machine. Dimension A includes errors from stator plates, cantilever effect, rotor plates and the Ecore assembly. Dimension B is the same but without Ecore assembly errors. Dimension C has only the stator plate errors. Results are shown in Fig.(2.6) on which the vertical bars show standard deviation. The starting setup was with stator plates 55mm apart, with both front and back beam covers fitted and uncut, and with 'loose' bolts.

The tolerance chain approach of Section 2.4 can be adapted for 6mm plate and only one layer of plate for comparison with the measurements, see Table (2.1). Several samples of dimension C are seen to be greater than the worst case calculated in the tolerance chain, all the remaining measurements at A, B, C are well within these bounds. Of note is that the measured dimensions are generally below the

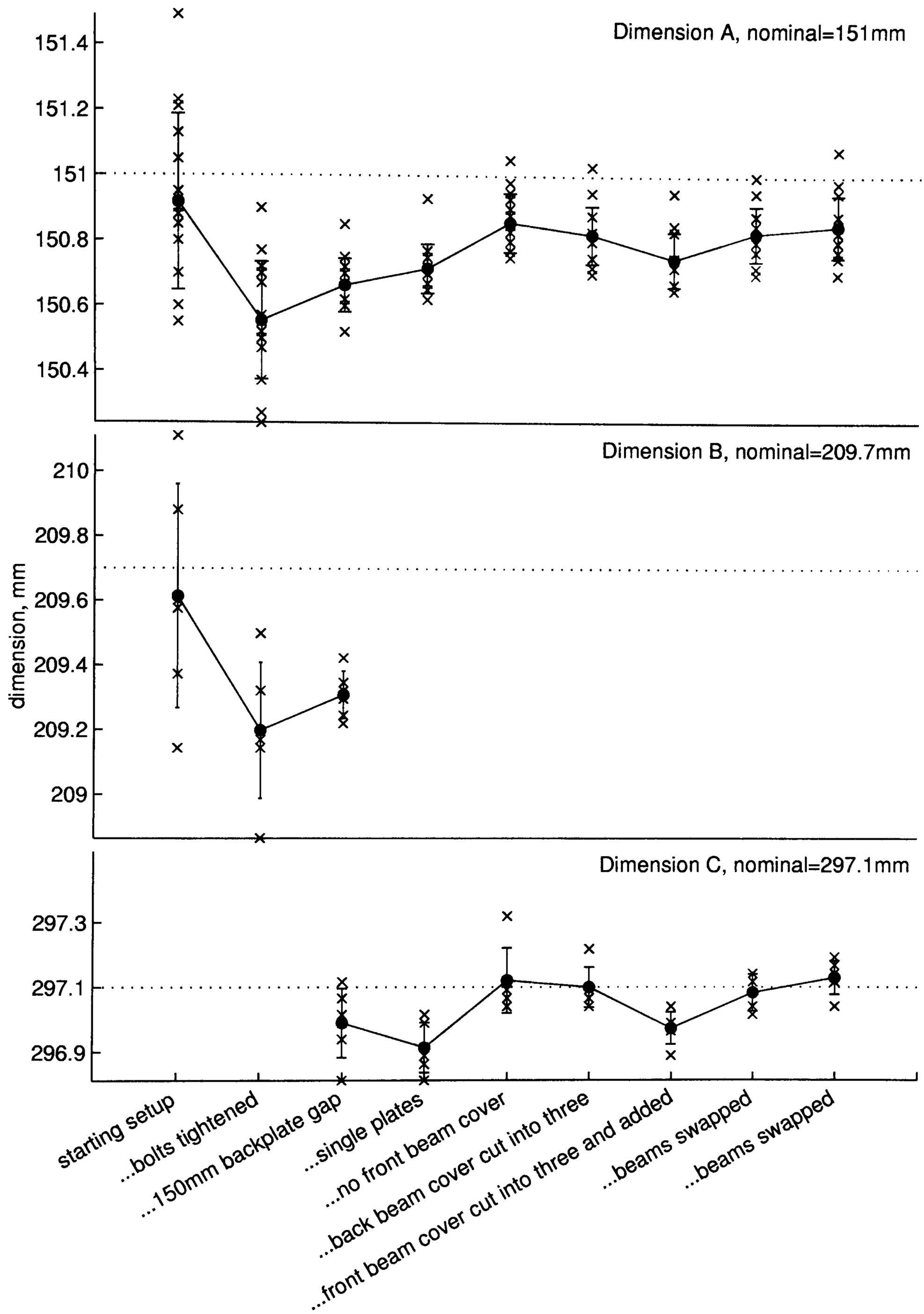

Figure 2.6: Factors affecting tolerance in LP2

nominal, which might be due to the laser-cut plates being generally smaller. This raises further questions about the nature of the laser-cutting errors-they don't appear to be random on a point to point basis. Errors decrease when the stator plates are moved apart, in agreement with tolerance chain arguments. Bolt tension in the beam clamps had a big effect, so the next machine had oversized cut-outs to help the beams to seat at the bottom of the cut-outs. Again, the travelling carriage error stopped airgap measurements at this stage.

stator spacing	Tolerance, +/-mm		
mm	Dimension A	Dimension B	Dimension C
55	2.6	2.4	0.2
150	1.3	1.1	0.2

Table 2.1: Tolerance chain results for LP2

2.5.3 Fishplates and Splitting the Machine

Fig.(2.7) shows various features of this stage of the work. LP2 was dismantled and all the LP2 plates were cut down the middle, so the machine had two halves. Then it was rebuilt with fishplates connecting the various plate-halves together. If the airgap were packed, fishplates unbolted from one set of plates, and the clamps undone from the shaft, then that half of the machine would be free to be lifted away. However, without the support of the shaft, the segment would distort. Therefore, a replacement for the shaft was required, to be fitted before splitting started. Two different approaches were tried, one using pairs of opposing stepped dowels, the other using large studding and nuts. Access to inner surfaces of the machine for splitting the segments is a problem, so the fishplates on the outer plates had clearance holes for an extended Allen key to unbolt the fishplates on the inner plates. The rotor plate design was tested at this stage, by machining the features required for magnet module mounting. This allowed measurement of the airgap tolerance, with a mixture of laser cut and machine cut in the machine. The airgap had a range of 2.7-3.4mm, from a nominal of 3mm.

Welded nuts were discarded from the fishplate design due to concerns about stress build up during welding for a practical machine, and holes in the fishplates were discarded because of weakness concerns. Opposing dowels were discarded as

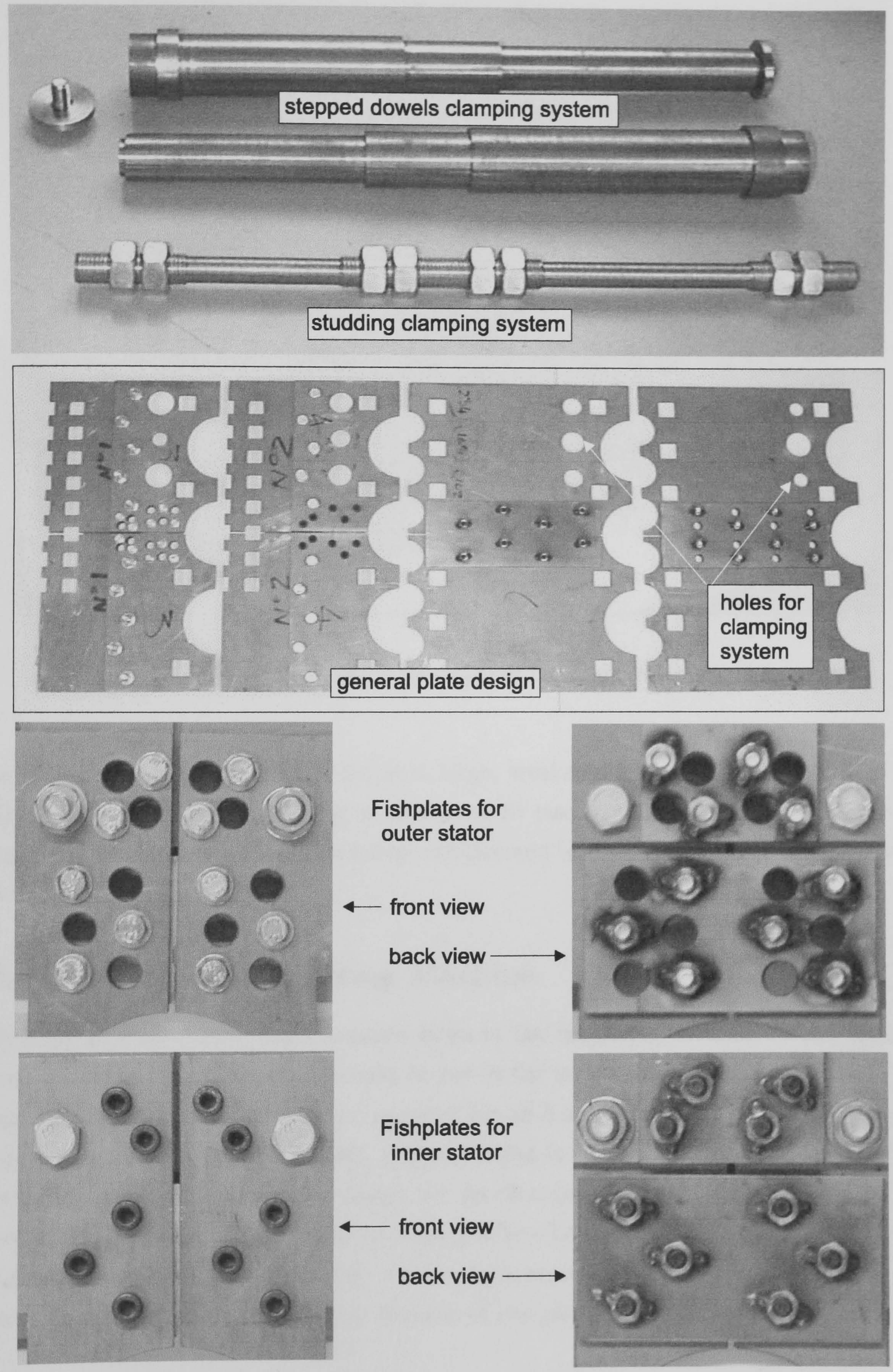

Figure 2.7: LP2 design features

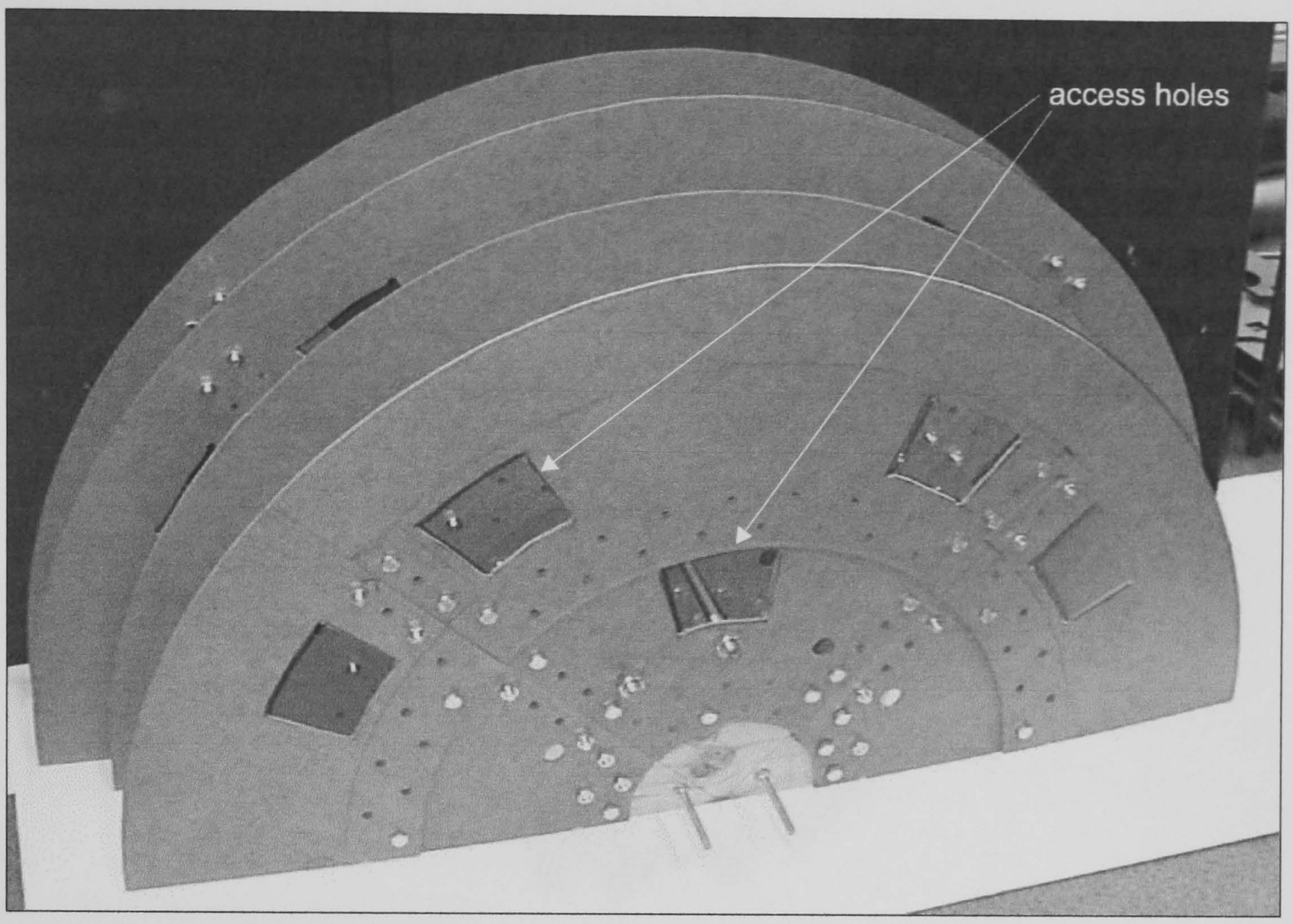

Figure 2.8: Wooden mock up of circular prototype

a clamping system because it required large, weakening, holes at one end of the machine, and careful machining of dowels to fit laser-cut holes. Also, plates were not fully constrained at the dowel step, which could lead to small distortions making refitting difficult.

2.5.4 Access for Splitting Machine

Instead of welded nuts and clearance holes in the fishplates, clearance holes large enough for hands and spanners could be put in the main plates to gain access to the internal surfaces. These holes are required for all 3 actions: fitting of the clamping system, unbolting from the shaft, and unbolting from the adjoining segments. A wooden mockup based on the design for the 2m diameter circular prototype was built, and a trial run performed, to identify where holes are needed in the plates to allow access, see Fig.(2.8).To undo the two innermost layers, fishplates with tapped bolt holes were spot welded to the far side of the plates so no access was required.

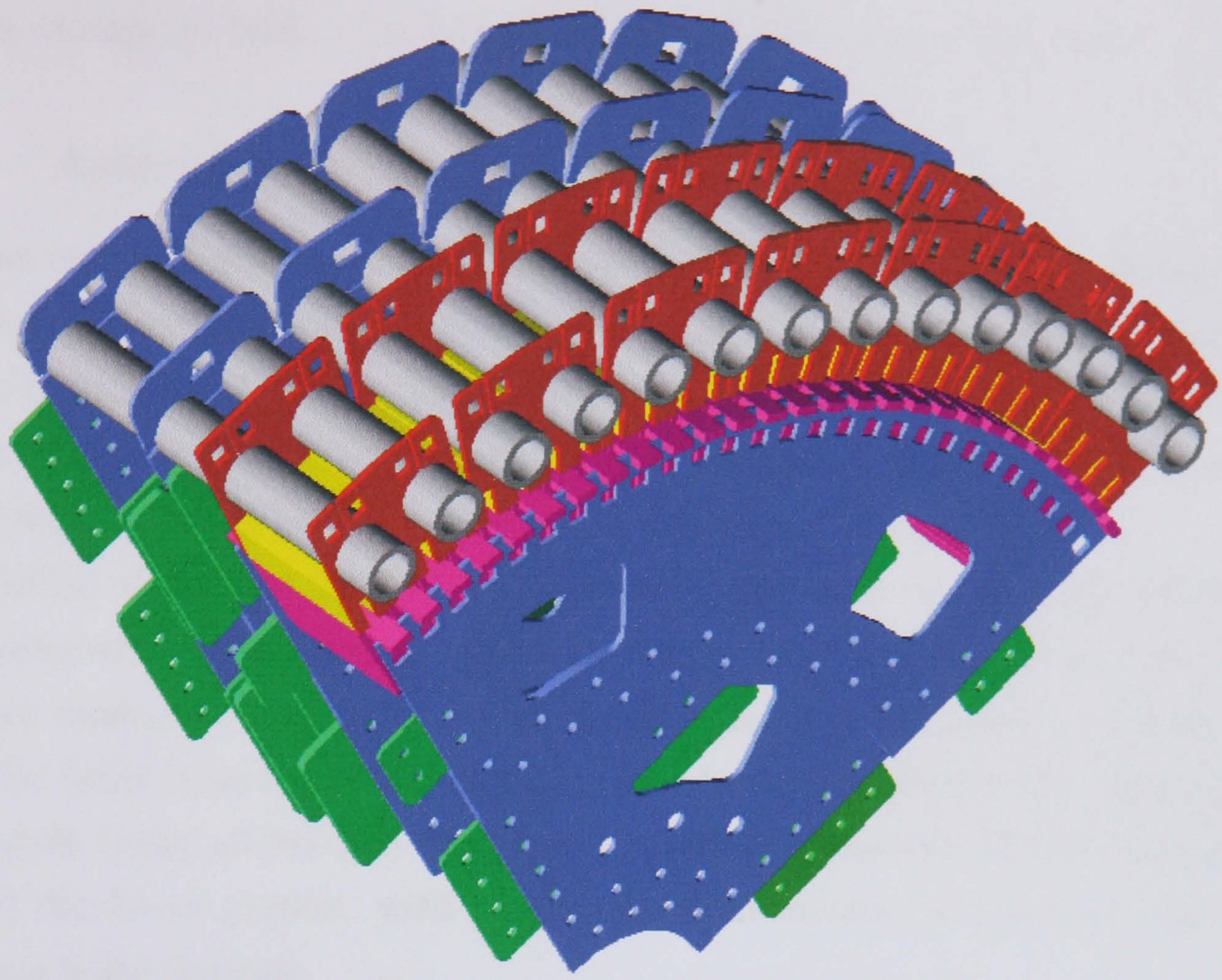

Figure 2.9: Segment of circular prototype

2.5.5 Circular Prototype

Fig.(2.9) shows the final design for the circular prototype. It was designed to be of sufficient scale to bring out the problems likely to be encountered in practice. A rotor diameter of approximately 1.6m was chosen corresponding to a pole number of 108 with 56 Ecore modules, and was large enough to allow holes in the machine plates for hands and tools. No windings were fitted since the porpoise was simply to explore the problems of assembling the structure, but if there were the machine would be approximately 80kWe @ 50 rpm. From experience of the previous prototypes, a stator plate spacing of 150mm was chosen, with which a nominal airgap of 3mm was aimed for. Seamless, high quality, thick wall tubes were used to eliminate tolerance contributions and deflections from them. The rotor magnet modules gave a flux density of 1.1 T in the airgap. The radial force due to this flux density at open circuit is approximately 280 kN/m^2. With coils fitted, the machine would have weighed 1,300kgs, of which 25% is magnets (which would be considerably less with neodymium magnets), a further 20% is laminations and coils, and 30% is beam weight, although the beams were oversized and would not weigh as much in a commercial machine. The remaining 25% is laser-cut plates and fishplates, Ecore

hangers, clamps ad bolts. The hub/shaft components are not included.

2.5.6 Assembly Procedure

The laser cut rotor and stator sector plates were assembled onto the machined collars with little difficulty. Generally, a little movement was possible at the bolted joints prior to tightening. This was inevitable, as bolt holes needed to be slightly oversized to guarantee a fit with the tolerances of laser cut plate. In practice this movement proved to be an advantage, allowing small adjustments to the plates.

Addition of the first few magnet modules to the rotor was proving difficult due to the magnetic forces between adjacent modules and also the plates. Some simple jigs were made, see Fig.(2.10), which transformed the task into a relatively easy one. The brass 'blank' module and 2 smaller brass side pieces were used to guide the module being added into the correct position. Magnetic keepers significantly reduced the forces present, with handles for manoeuvring and access slots to add the fixing bolts through.

During addition of the final E-core modules to the stator, the innermost upper stator plate buckled, closing the airgap. A set of 10mm thick plates was ordered for this layer, to replace the original 6mm plates. Various features on these plates were opened out a small amount to take account of the change in quoted tolerance of the laser cutting from $\pm$ 0.2mm to $\pm$ 0.3mm.

A dial gauge was used to fit the plates and get them as concentric as possible, although this did not give an absolute measurement of the radius being adjusted. During fitting of the stator plates, the dial gauge was used on the outside edge of the lower plates which were adjusted to minimise eccentricity, then this was repeated for the upper plates. This resulted in a radial variability of less than 0.4mm for all stator plates, upper and lower.

The beams were then added without the Ecore modules, so that the structure had maximum stiffness before adding the Ecores and hence applying magnetic forces. Measurements were taken of the radial distance from a selection of the magnets on the rotor to the bottom of the beams on the stator. This showed that eccentricity in the rotor at the airgap was $\pm$ 0.5mm, and eccentricity of the stator and beams at the airgap was also $\pm$ 0.5mm. Both these eccentricities were centered around the nominal. For comparison, a tolerance chain analysis gives stator tolerance, (axially half way along the airgap) of $\pm$1.7mm, and for the rotor, $\pm$0.4mm. These two combined, plus Ecore hanger tolerance of $\pm$0.2mm gives an expected worst case

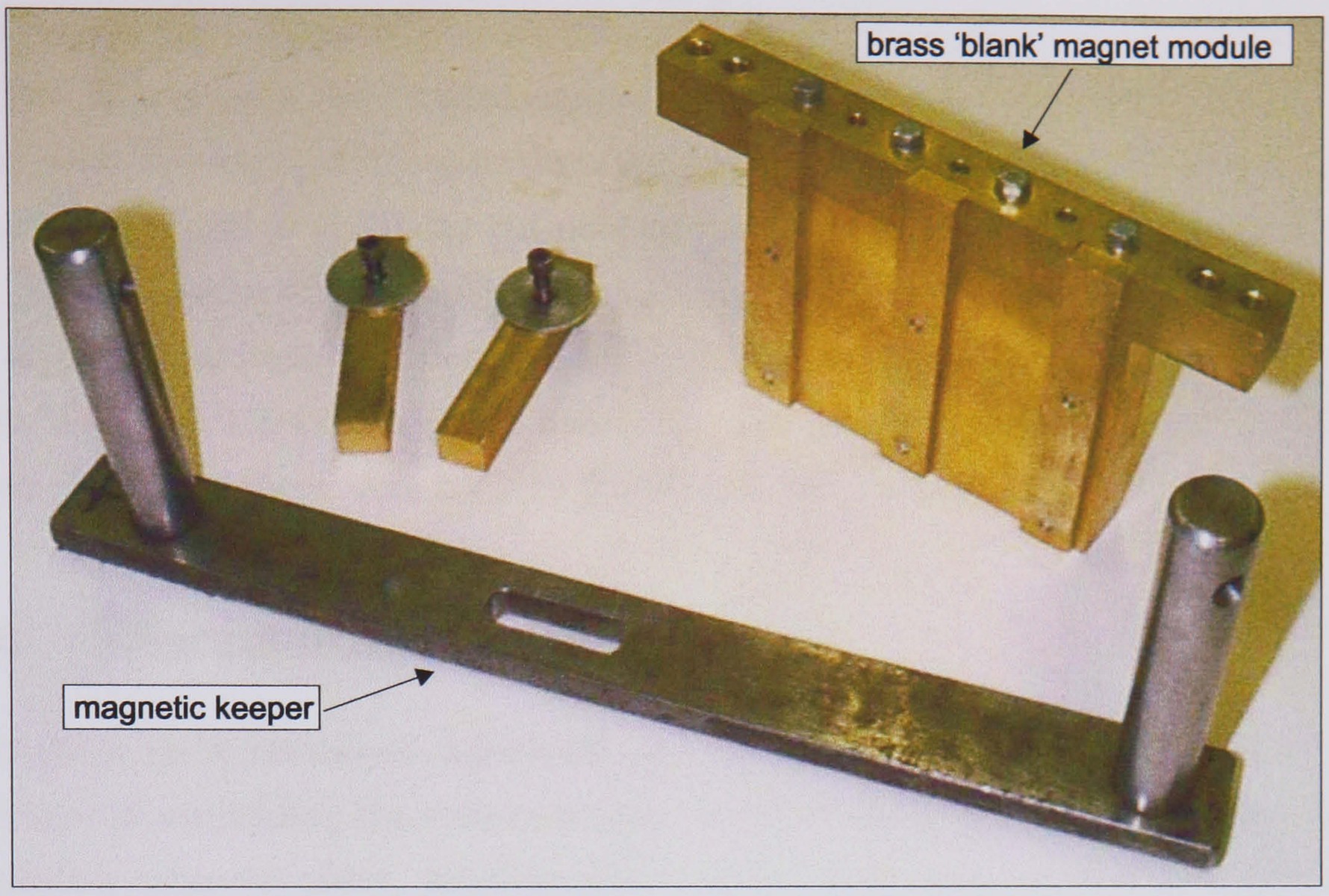

Figure 2.10: Jigs for magnet installation

Figure 2.11: Circular prototype

tolerance at the airgap from laser-cutting errors of ±2.3mm.

The E-core pairs were added one-by-one evenly around the stator, but as this progressed the airgap started to decrease until in places it closed. To correct this. shims were placed in the beam cut-outs on the inner stator plate to pack the beams up. This was successful in roughly controlling the airgap sizes. but at the same time the airgaps were found to alter over time. The airgap size after shimming settled to be in the range 1.8-4.5mm (3mm nominal). The machine was driven up to 50 rpm (open circuit, as there were no coils fitted) and ran successfully.

2.6 Discussion & Conclusions

This work on a combined segmental and modular design has demonstrated the principal of assembling large electromagnetically modular generator structures from accurately laser-cut plate, avoiding the need for large diameter machine tools and for transport and lifting of the complete machine. Connecting the segments together using fishplates has proved successful, and access for splitting via large holes in the main plates has proved practicable. On LP2, two approaches were tested for the clamping and stiffening of the separated segments, and both worked well, although the studding approach is preferable. Airgap tolerances on the LP2 prototype were acceptable and generally much less than the tolerance chain worst case analysis, and this is also true on the circular prototype until the addition of the Ecores. Shimming of the beams on the circular prototype allowed a reasonable airgap to be maintained. The airgap shrinkage and drift over a few days afterward is of concern. One possible cause is a multitude of mechanical degrees of freedom from the design of the joints between the beams and the stator plates. Another could be that the 6mm plates were not stiff enough. Further work would probably solve these issues.

The problems encountered during assembly are greatly amplified by the use of a cantilevered stator. An arrangement in which the stator beams are supported at both ends would be more resistant to distortion and would be less sensitive to the tolerances in the laser-cutting process.

Whilst demonstrating the structural concepts successfully, the work emphasized the large magnetic forces trying to close the airgap, due to the ironed stator and rotor, creating structural problems (plate buckling), and requiring heavy structures. The work also highlighted the build up of tolerances leading to a variable airgap length and varying magnetic forces. Vibrations and resonances were not addressed.

Chapter 3

Double Airgap Machines

At the airgap of an electrical machine, there are torque forces, airgap-closing forces and centering forces, the latter tending to line the stator and rotor up. In single airgap machines the structure has to withstand the entire airgap closing force, and for a radial airgap configuration this force cancels at the hub. In a single airgap axial machine, this cancelling would not occur. Airgap-closing forces can be cancelled more locally by adoption of a double sided airgap, which could be radially or axially arranged. If the airgaps are symmetrical the forces cancel out completely leaving zero airgap-closing force, but in reality the variations in the airgap length due to mechanical tolerances create residual force. The forces created by airgap tolerances, be they airgap-closing or centering, are termed Unbalanced Magnetic Pull (UMP), with the airgap-closing force being of most concern as it can be a run-away effect if the structure is not stiff enough. This work investigated how significant these UMPs are in a double airgap PM machine by developing a test rig which could measure these forces directly, for a linear section of machine. A model of the airgap-closing force were developed and compared with the experimental data.

3.1 Experimental Rig

The double sided airgap arrangement of a real machine was represented by a linear portion of rotor and 2 linear portions of stator. The stators were two 4 inch square, 5mm wall thickness, mild steel box sections. Three different rotors were tested:

(i). eight 4" x 4" x 1" ferrite magnets attached to an aluminium rotor structure

(ii). eight 4" x 4" x 1" ferrite magnets enclosed in a composite non-magnetic rotor structure

(iii). six pairs of 6" x 4" x 1" ferrite magnets, each pair with a separate steel rotor support sandwiched between them.

Fig.(3.1) & Fig.(3.2) show the rig and some examples of airgap positions, Fig.(3.3) shows the principle of operation and Fig.(3.4) indicates the main flux paths, with a simplified representation of the rotor and stator. The definition of the axial and radial directions define the rig as a double sided axial airgap machine, but this is an arbitrary choice for labelling purposes only. The two fundamental requirements were that it is possible to vary the position of the stators w.r.t. the rotor, and that the rotor was free to move in a horizontal direction in response to a centering force, and a vertical direction to an airgap-closing force ie the response to the two different forces was decoupled. To achieve this the rotor was suspended from the rig frame using clevises and two lengths of studding so it was free to swing. The stators were connected to slots in the frame with studding and nuts, so their position w.r.t. the rotor could be changed. Any airgap-closing force pulling the rotor down would make the rotor structure rotate about axis A and would be counterbalanced by a spring balance attached to the rotor lever arm. Any centering force pulling the rotor to the left would make the rotor structure rotate about axis B, but due to the freedom to rotate at axis A, the rotor itself would rotate about axis C, which was vertically above the centre line of the rotor. This centering force will be counterbalanced by the two spring balances which are attached to the rotor with wires passed over two pulley wheels on the frame.

A simple calculation was performed to establish that the flux path through the box section was not saturated. Mild steel saturates at approximately 1T. Eq.(3.1) was used to calculate the magnetic field density within the magnet, B_g and at the airgaps,

$$B_g = \frac{B_{rem} t_m}{t_m + 2t_g} \tag{3.1}$$

where B_{rem} is the magnet remanence, 0.4T, t_m is magnet thickness, t_g is the nominal airgap each side. Eq.(3.2) was used to calculate the magnetic field density in the box section wall, B_s,

$$B_s = \frac{B_g A_m}{2A_s} \tag{3.2}$$

where A_m is the surface area of one magnet and A_s is the combined cross section of all 4 walls of the box section. These calculations assume no leakage fluxes, infinite permeability of the steel whilst not saturated. The maximum flux density is found

to be acceptable at 1T, for the rotor with six pairs of 6" x 4" x 1" magnets with a nominal airgap of 12.1mm. However, at each end of the rotor, the flux from half of the end magnets has to be transmitted by the frame. Mainly this is of substantial cross section to transmit this flux without saturation, but the M16 studding that supports the stator box section is up to 8 times too small a cross section for this porpoise and would saturate for all three rotors at their nominal airgaps. This error is neglected in the modelling work.

3.2 Experimentation

To take a force measurement the procedure was:

(i). set the rotor and stators so that both gaps are at the nominal airgap length chosen, and there are no nett magnetic forces. The weight of the rotor will be held on the upper stop-spring. To balance the weight, the lever arm spring balance is tensioned until the lever arm tips over and just rests on the lower stop-spring. The spring balance reading is noted for subtraction later. Also, the weight of the centering spring balances pulls the rotor to the right, so two sets of counterweights are used to balance this.

(ii). adjust the position of the stators to approximately the position required, using the studding for vertical positioning, and the slots and chain drive for horizontal positioning. Any resultant airgap-closing forces will have the lever arm pressing on the upper stop-spring, and any centering forces will have pulled the rotor to the left.

(iii). adjust the tension in the centering spring balances to re-align the rotor horizontally, and in the lever arm spring balance until the arm tips back to the lower stop-spring. Measure the actual airgap position and spring balance forces.

Experimental results are shown in Fig.(3.5) to Fig.(3.9). For the radial offset tests with a steel rotor structure, if the stators are moved one way then this steel structure encroaches on the airgap. Therefore Figs.(3.8) & (3.9) show results from offsetting the stators both ways.

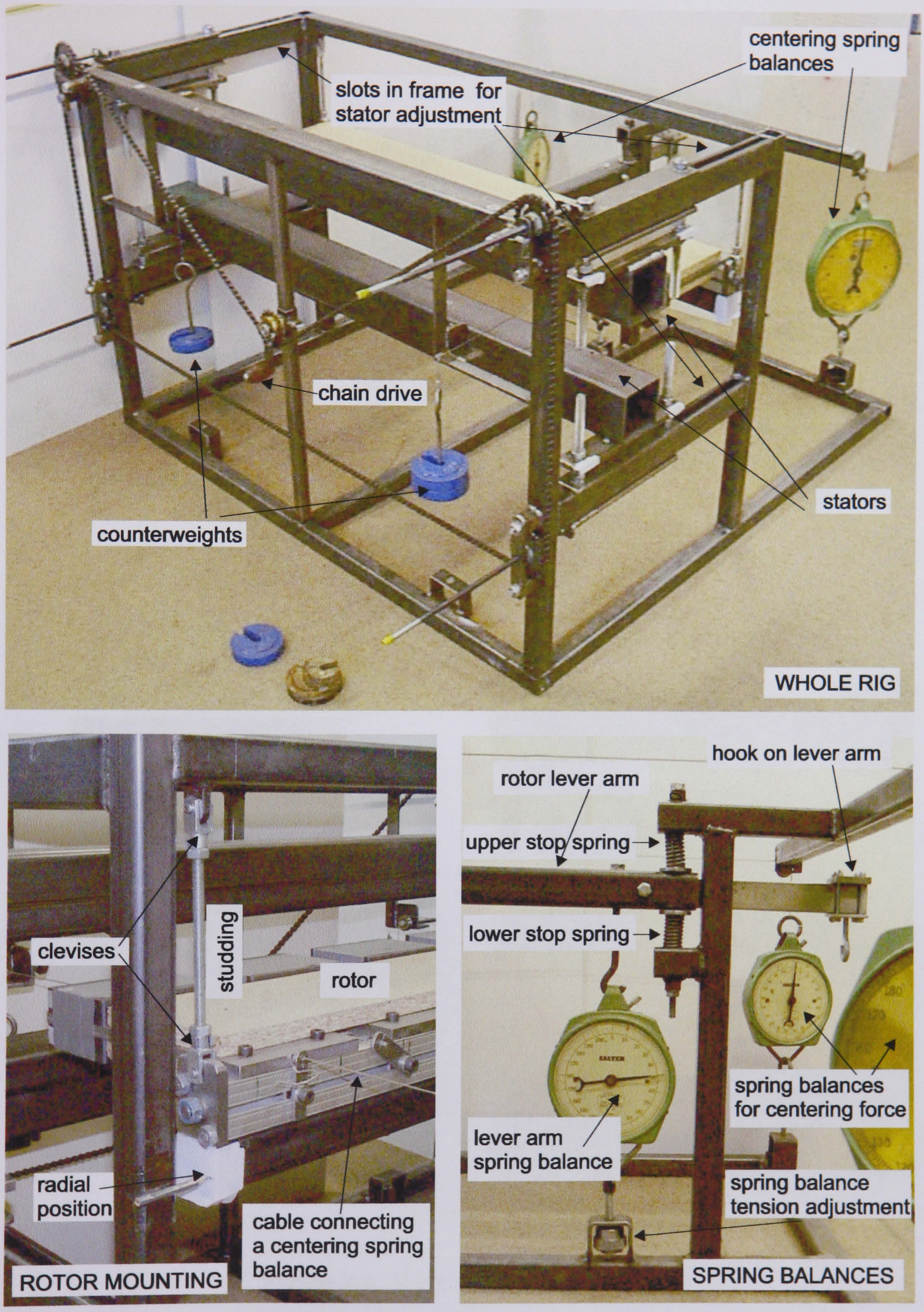

Figure 3.1: Experimental rig

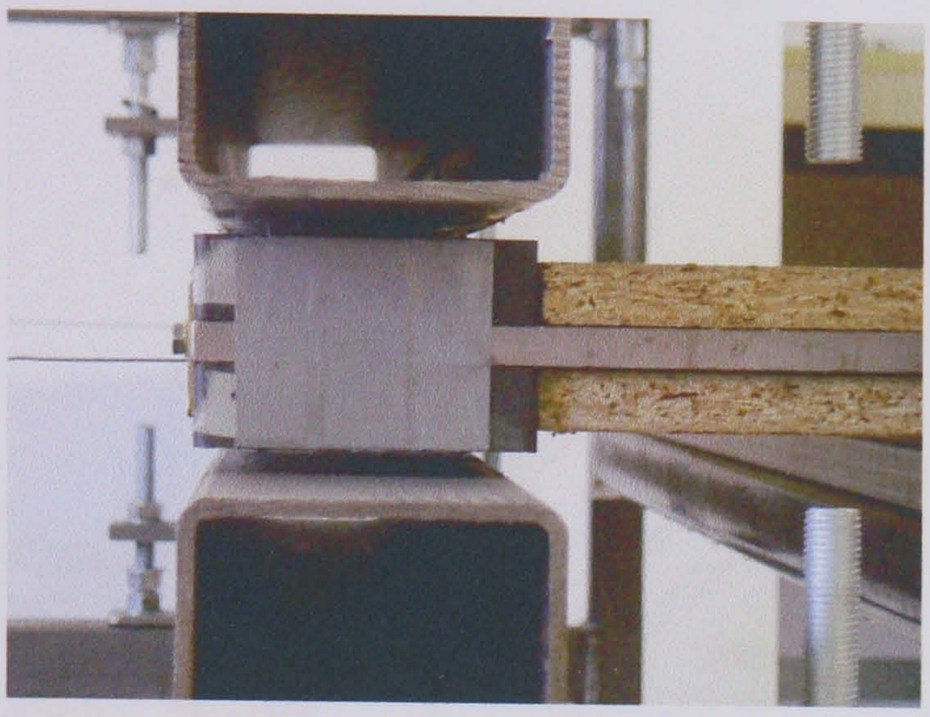

Centred airgap

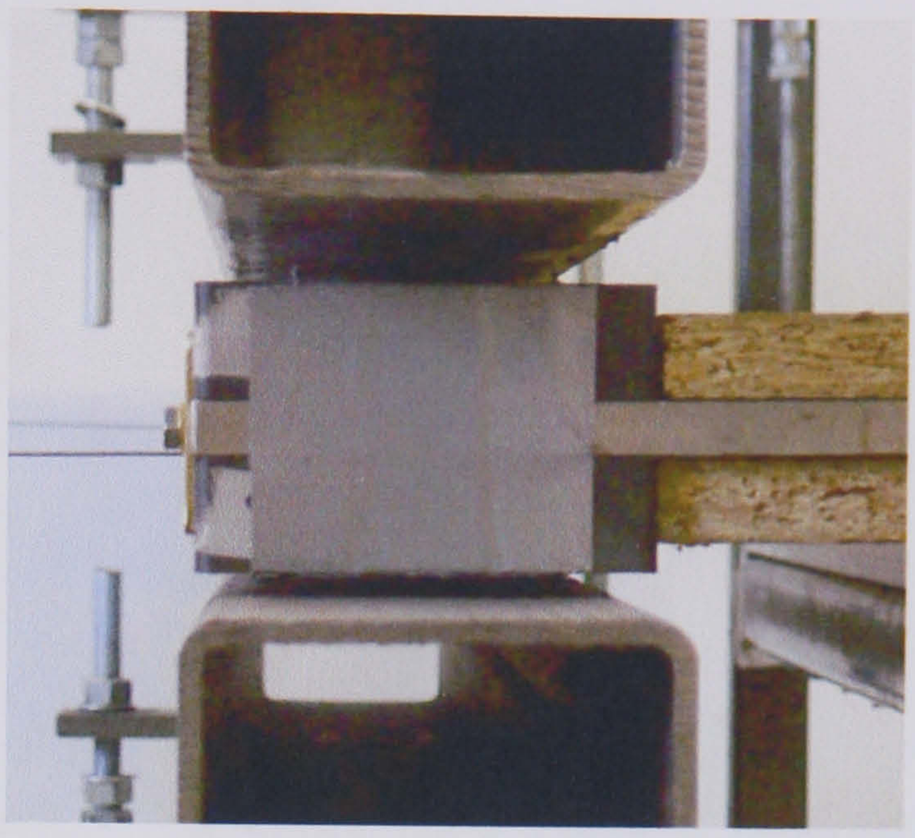

Axially displaced airgap

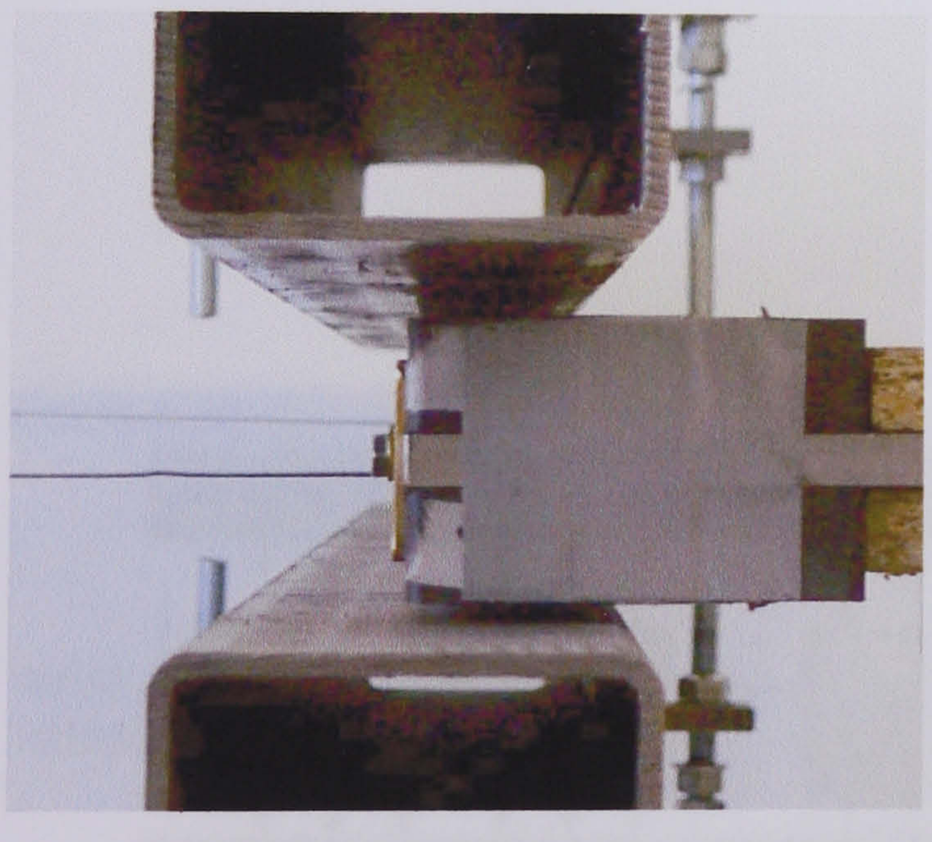

Radially displaced airgap

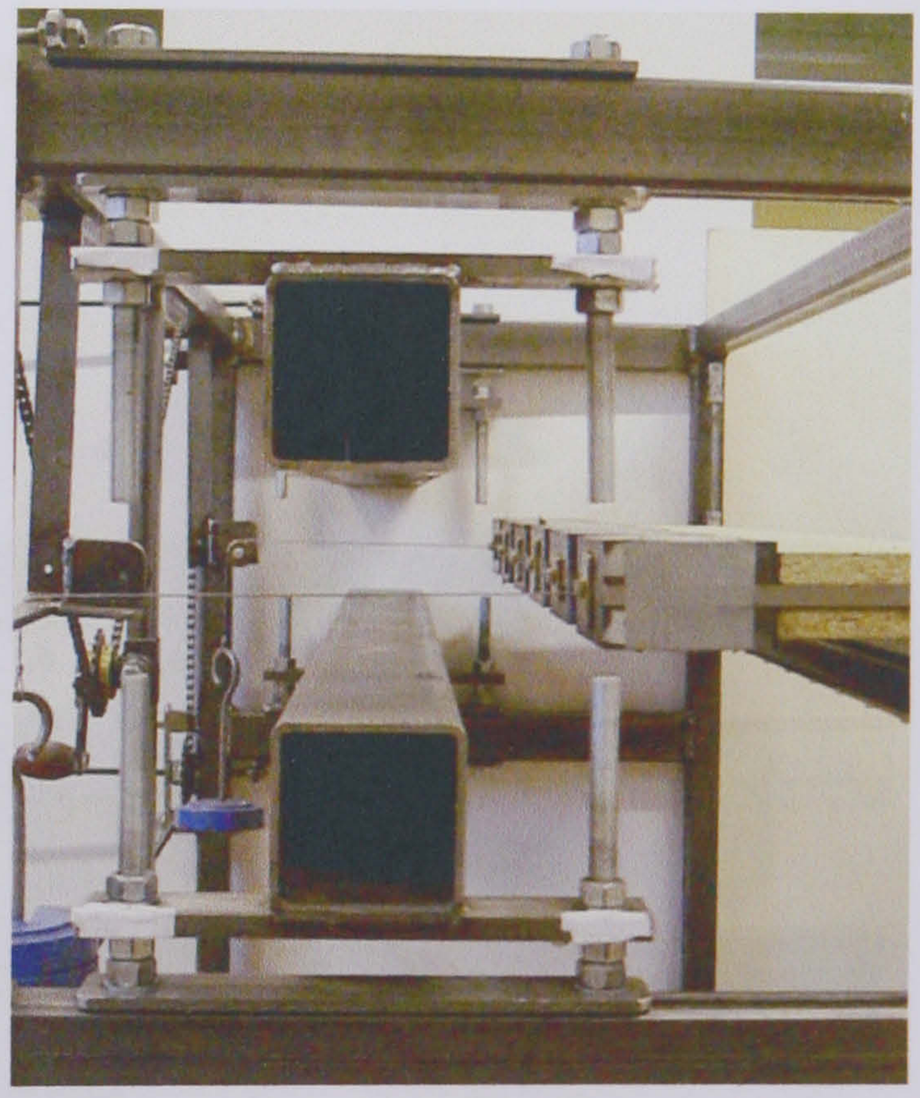

Stators wound all the way out

Figure 3.2: Various airgap positions

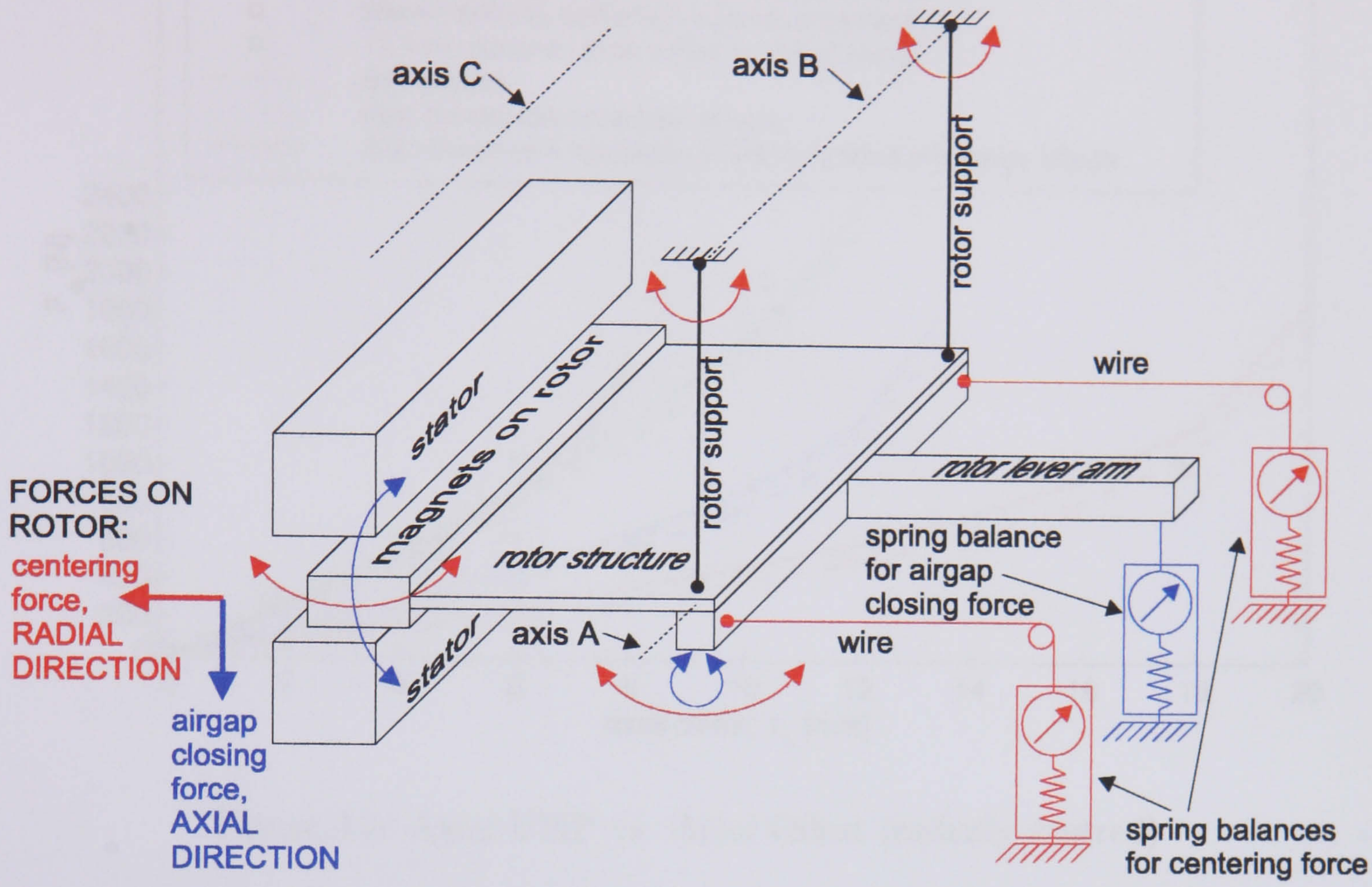

Figure 3.3: Main features of experimental rig

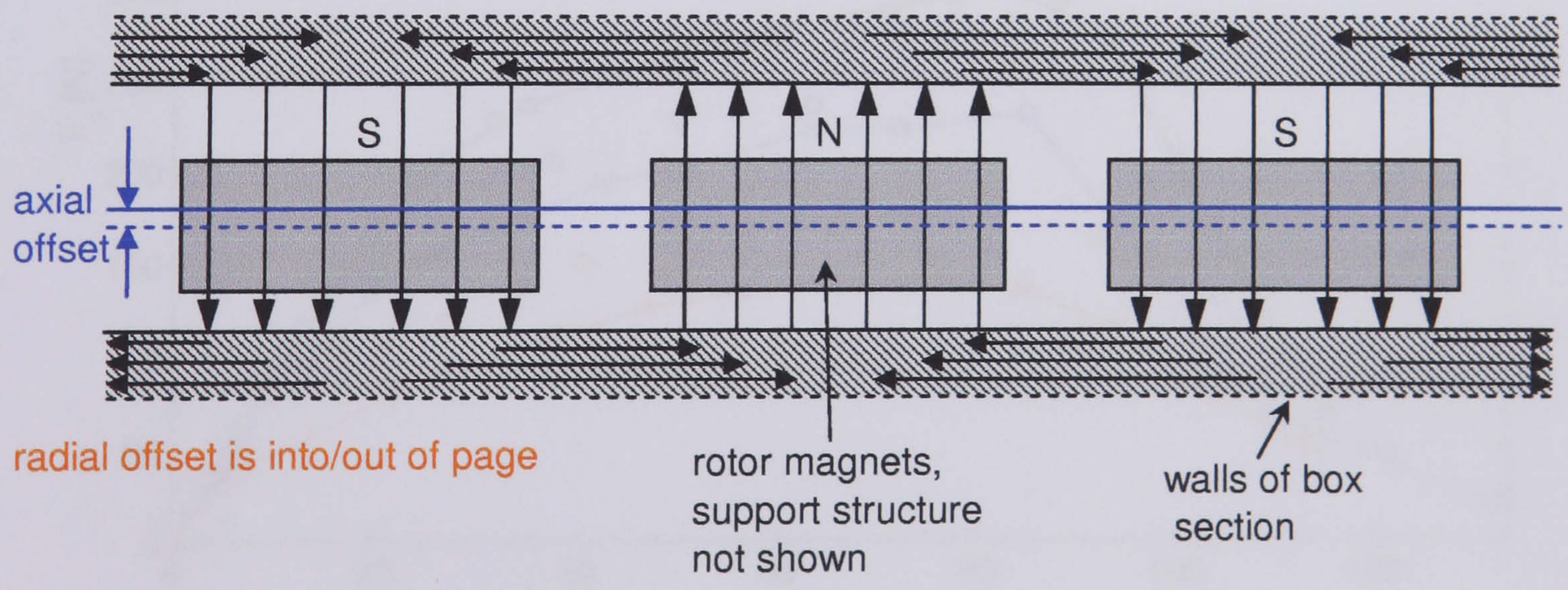

Figure 3.4: Indication of main flux paths

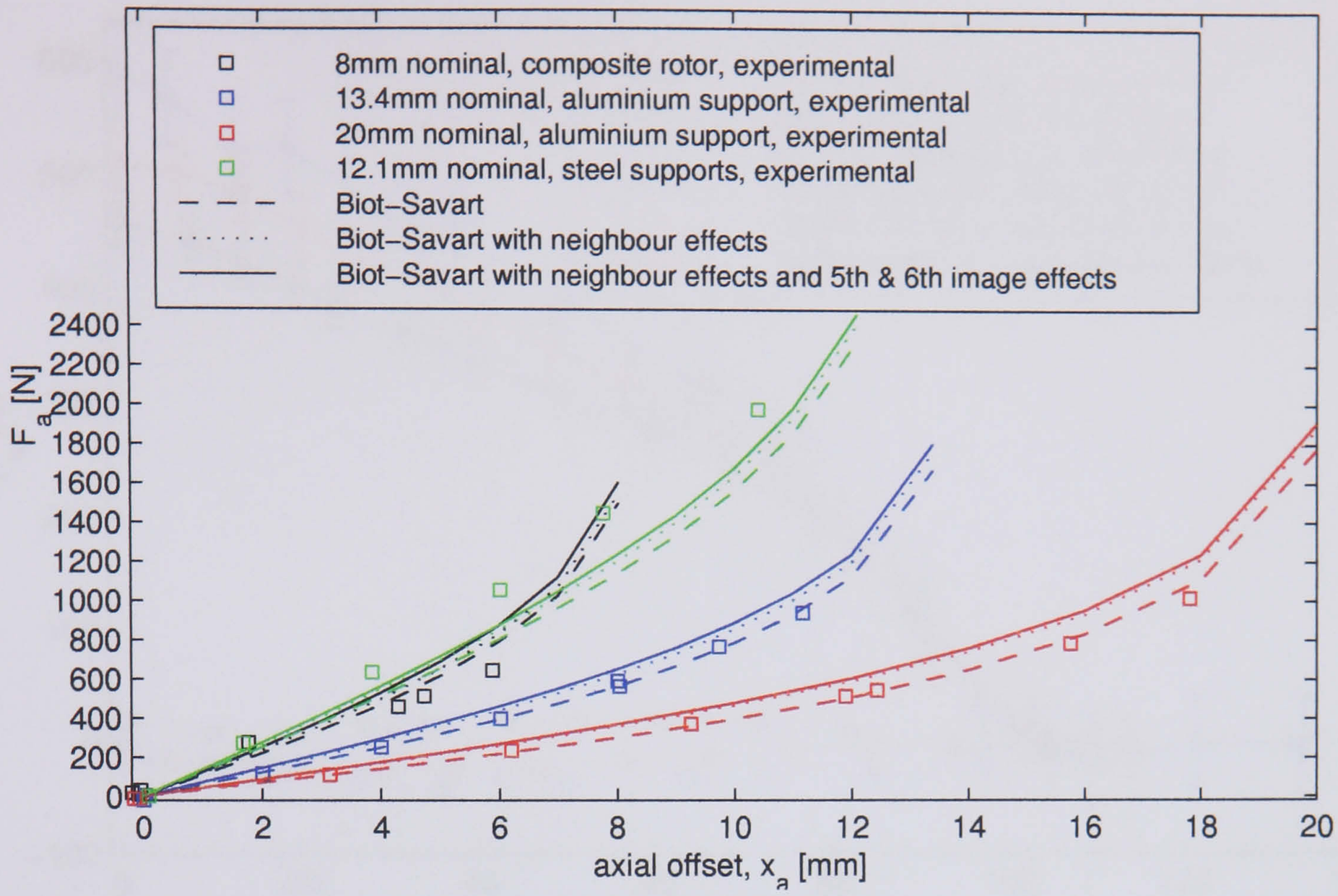

Figure 3.5: Axial UMP vs. Axial Offset (radially centred)

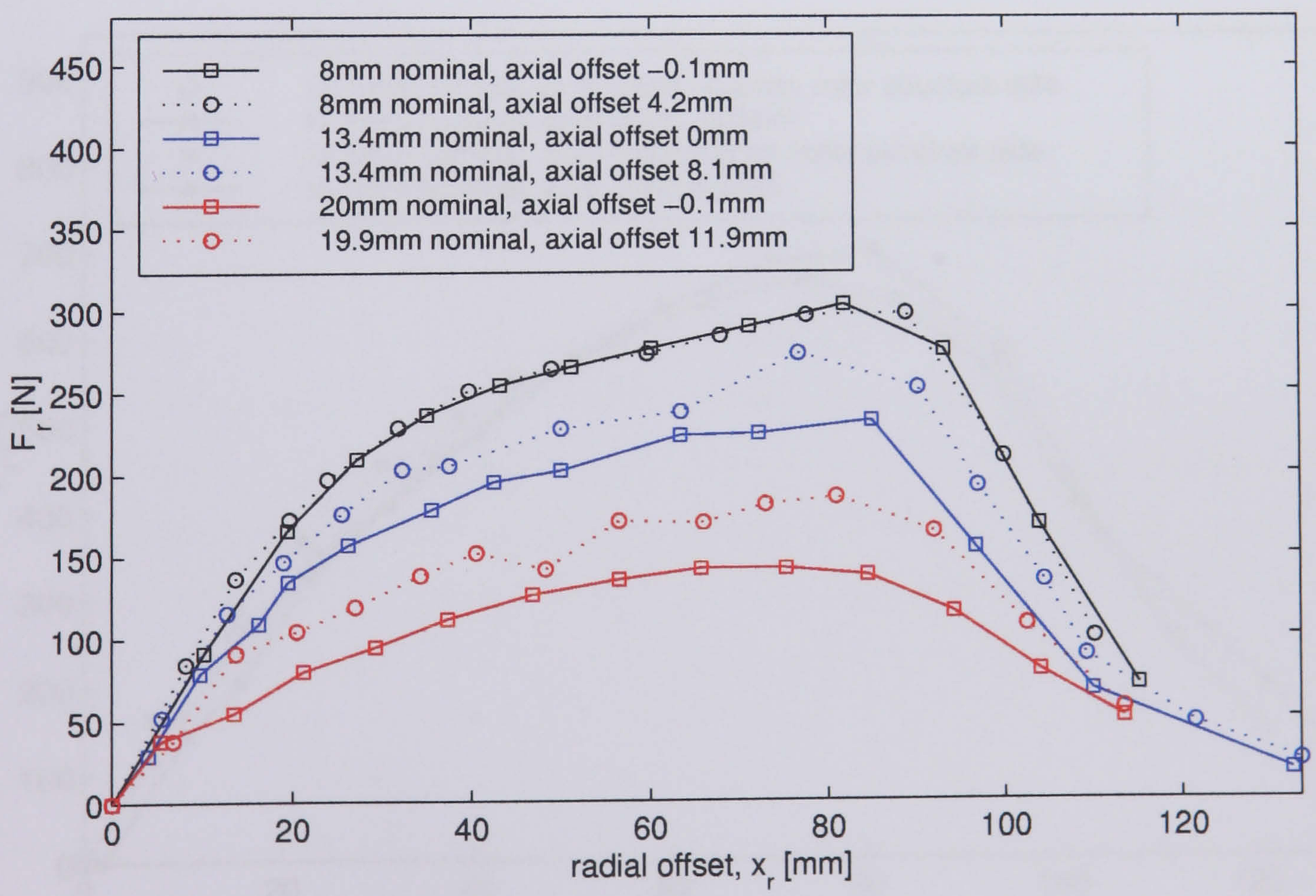

Figure 3.6: Radial UMP vs. Radial Offset (non-magnetic rotor support)

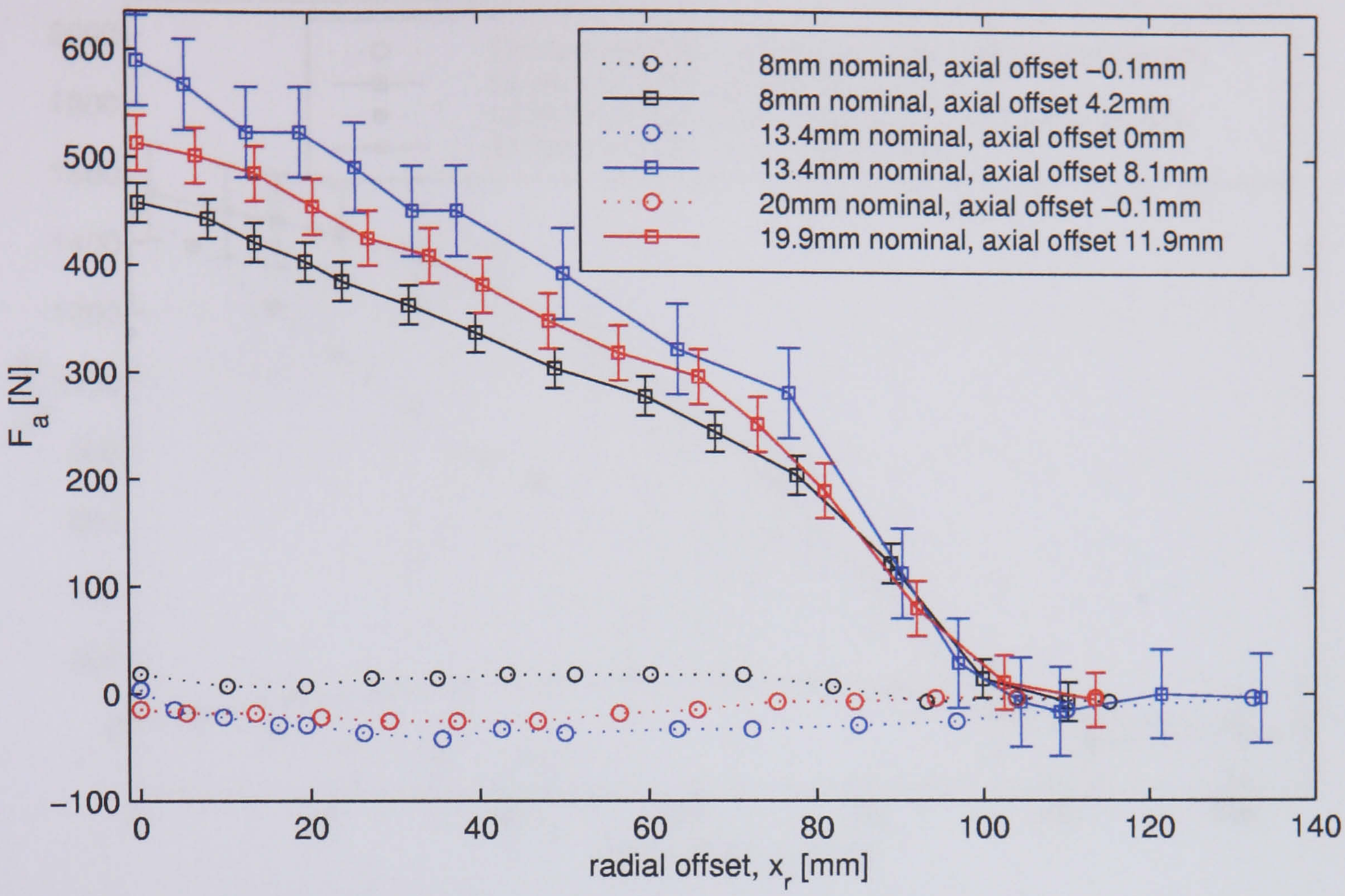

Figure 3.7: Axial UMP vs Radial Offset (non-magnetic rotor support)

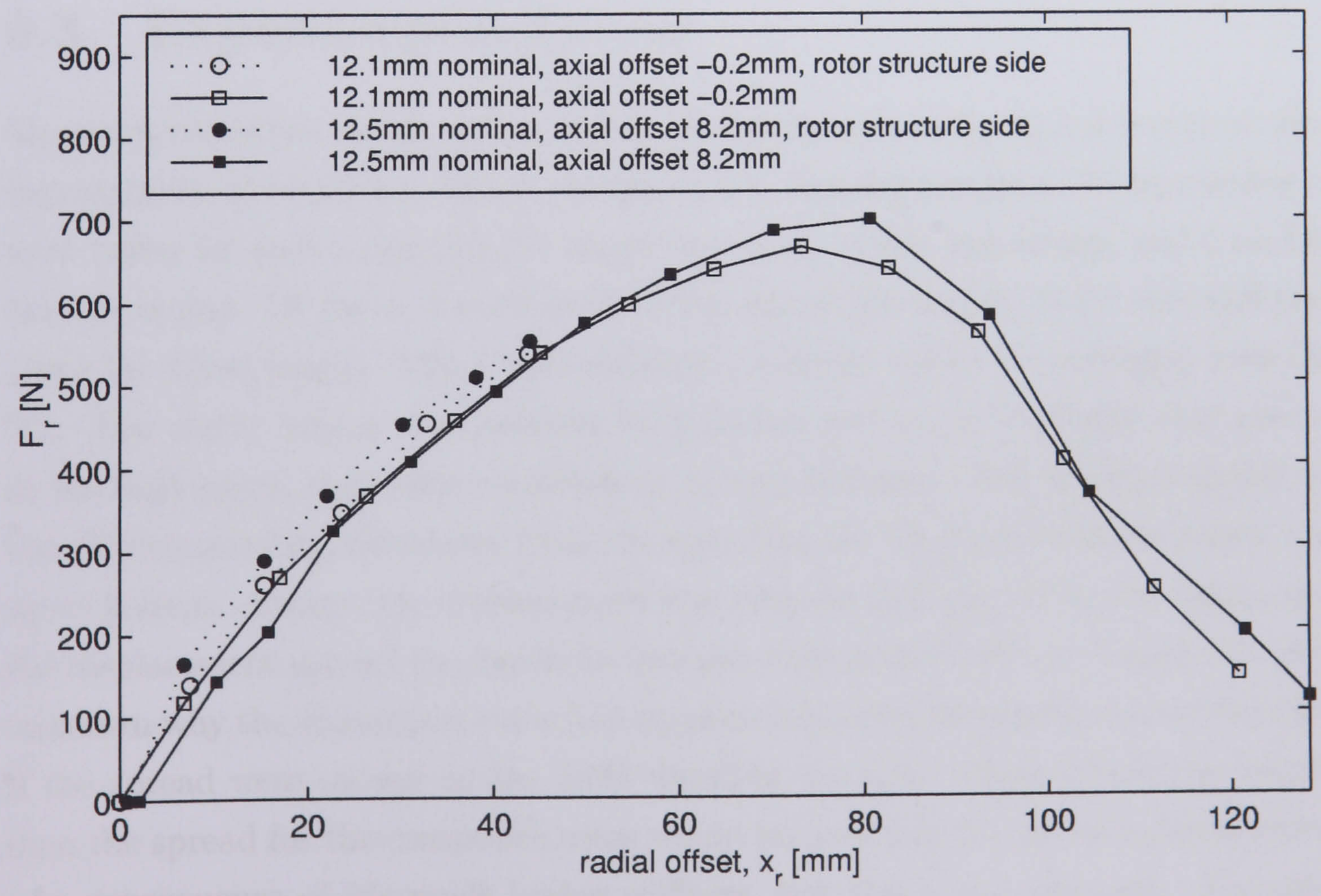

Figure 3.8: Radial UMP vs. Radial Offset (magnetic rotor support)

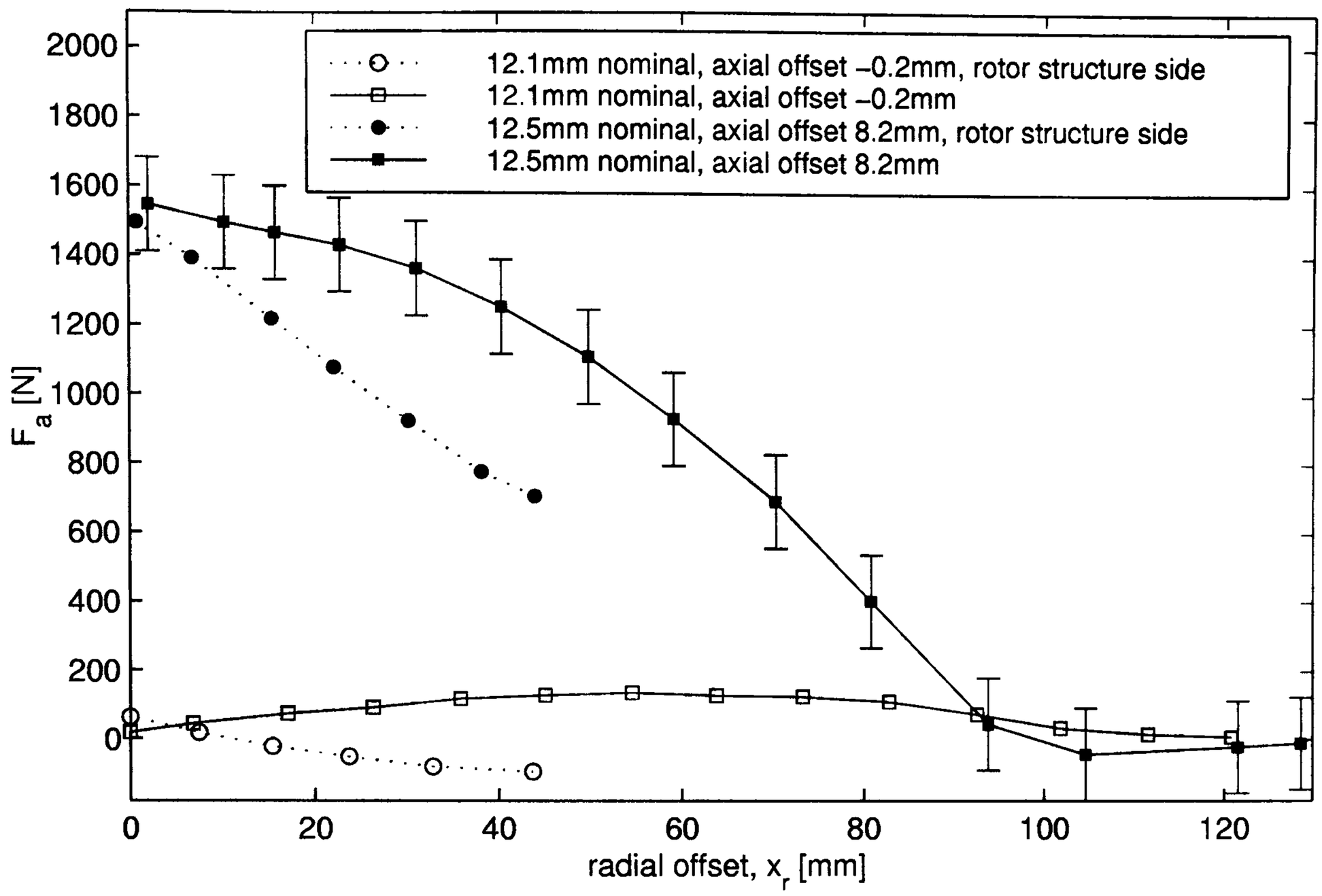

Figure 3.9: Axial UMP vs Radial Offset (magnetic rotor support)

3.3 Experimental Errors

Measurement of the airgap length used telescopic gauges and a digital vernier to give repeatability of ±0.02mm. When the airgap was radially centered, 10 measurements were taken for each airgap length measurement, 5 on the top airgap, and 5 on the bottom airgap. Of the 5, 4 were at the 4 corners of the airgap, and 1 was half way along the beam length. The 4 were averaged, and the result was averaged with the 5th. The stator beams were concave by 0.14mm, and as the readings were always at the high point, they were corrected by adding 0.07mm. The resulting spread on the displacement x_a, calculated from the spread in the 10 airgap measurements, was up to 2.4mm. Always, the displacement was greatest half way along the beam, and the displacement spread was found to increase with axial UMP, see Fig.(3.10). It is unknown why the aluminium rotor had significantly lower spread than the other two. If the spread were caused by the UMP bending the rotor along the airgap length, then the spread for the composite rotor would be less than for the aluminium rotor, as a consequence of it's much higher stiffness, but this is not the case. The steel stiffness is very low as it is composed of individual elements, and not a large plate. This is pursued no further as the small spread size and averaging process should

result in negligible errors.

For the tests which were not radially centered, radial airgap offset, x_r, was measured at both ends and then averaged, the spread in the offset from one end to the other was at most 2.5mm. It was not possible to accurately measure the axial position of the rotor once it started to clear the stator beams in these tests. The non-zero axial force for the axially centered tests of Fig.(3.7) and Fig.(3.9) is evidence of drift in the axial position of the rotor.

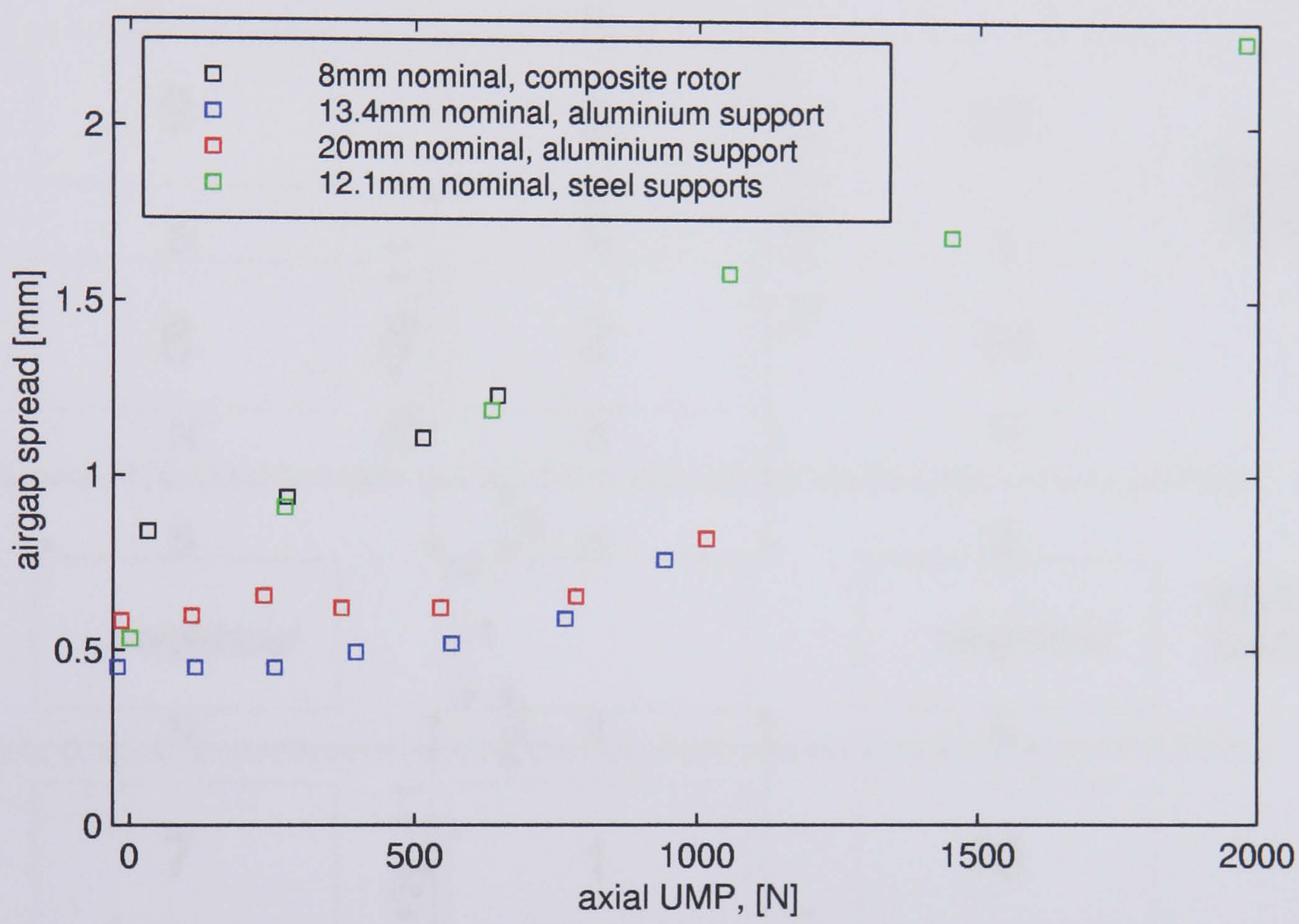

Figure 3.10: Variations in airgap spread

3.4 Biot-Savart model of the airgap-closing forces

Each permanent magnet on the rotor, which normally has a relative permeability of 1.05, can be represented as a region of permeability μ_0 with it's magnetization represented by current sheets around it's edges. Each stator can be represented by an infinite boundary of infinite permeability. When there is one plane boundary the method of images allows such a boundary of a region containing currents to be replaced by a mirror image of those currents reflected in the boundary, the symmetry of the real and image current distribution creating the same flux distribution, with flux lines normal to the removed boundary surface. With two parallel plane bound-

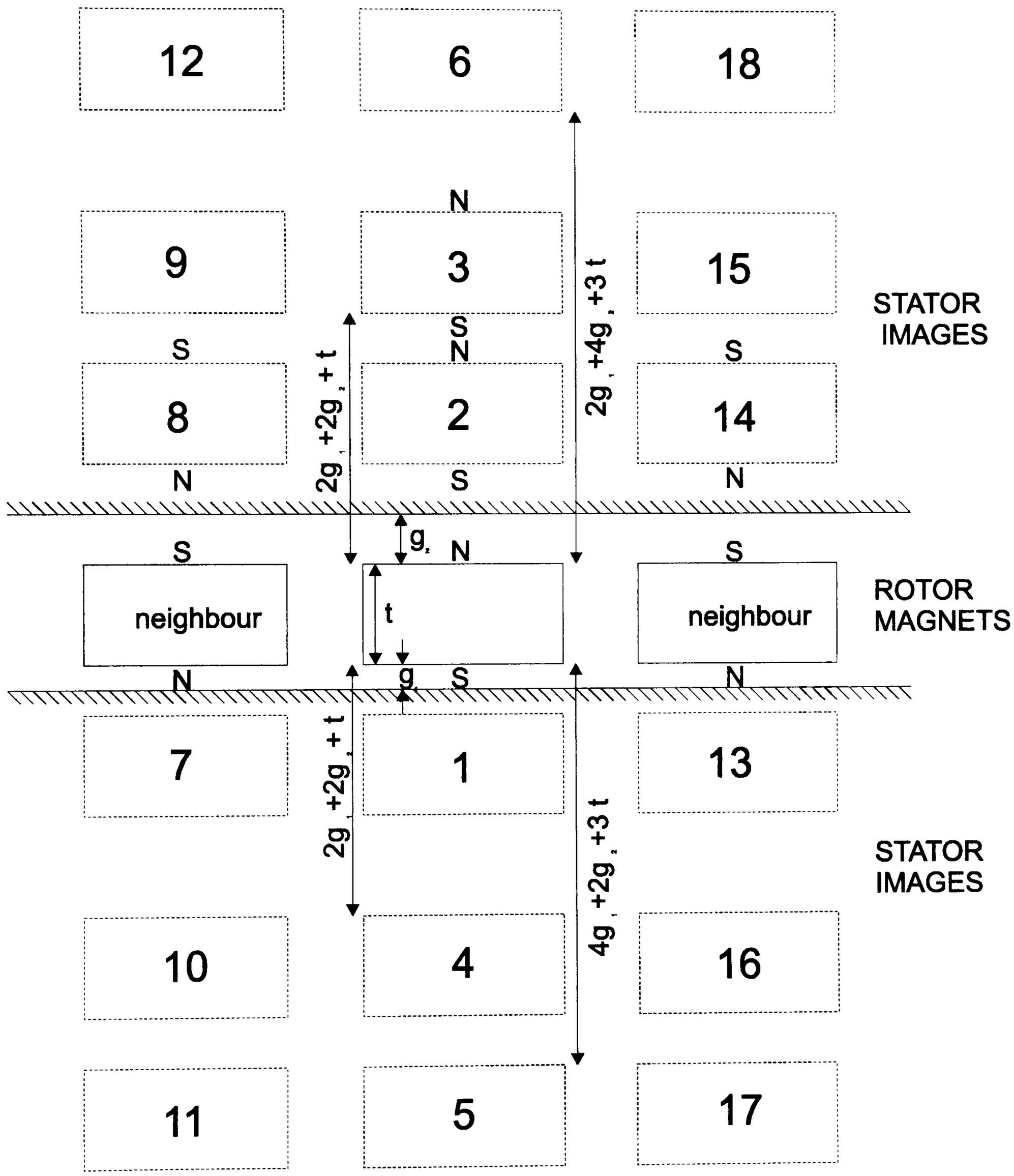

Figure 3.11: Method of Images Applied to a Double Airgap Machine

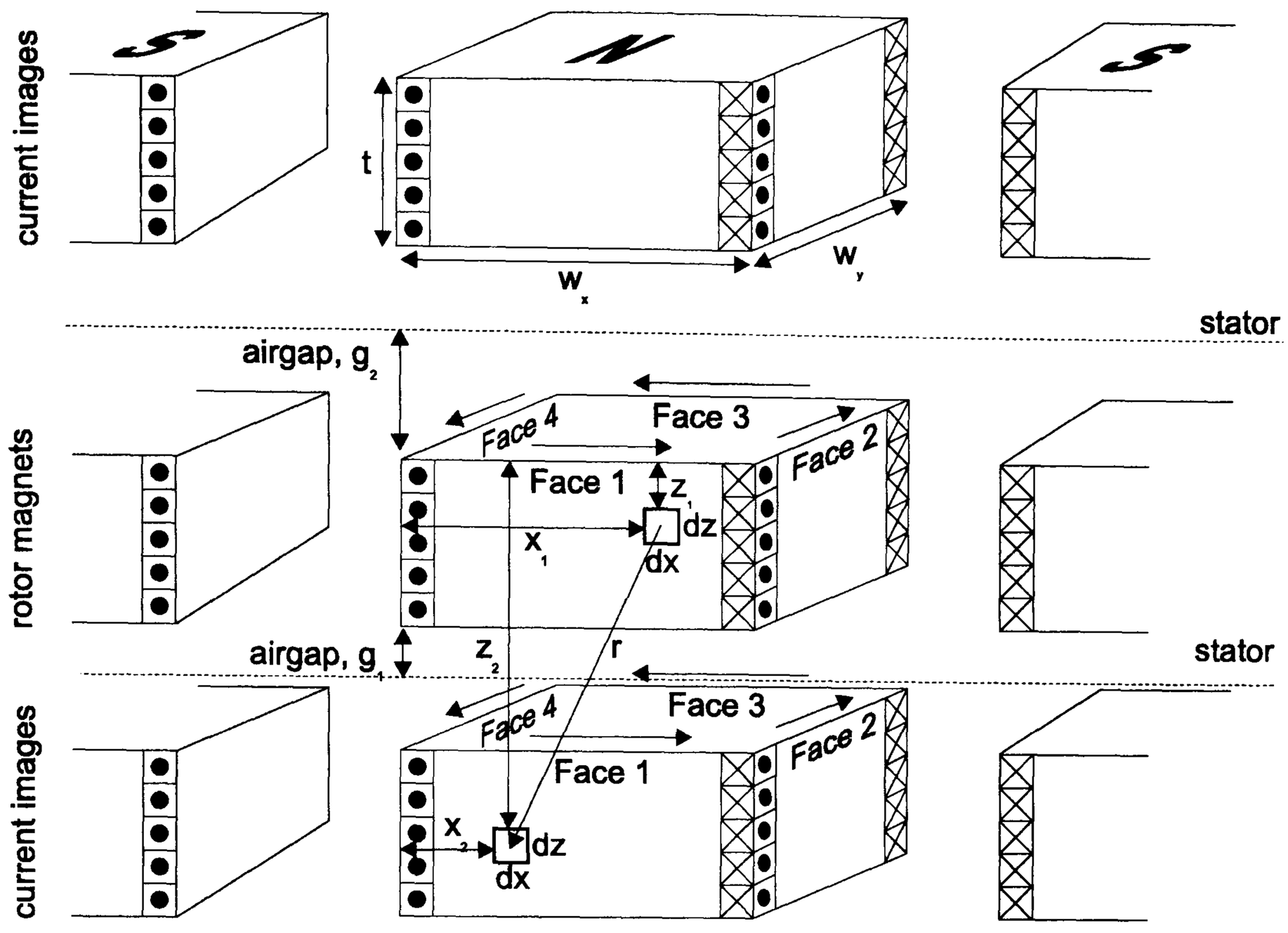

Figure 3.12: Details of Biot-Savart Calculation

aries, an infinite series of images is needed to create the same flux distribution, see [8]. Fig.(3.11) shows a truncated set of images. The Biot-Savart equation:

$$d\mathbf{F_2} = \frac{\mu_0}{4\pi r^2}\mathbf{I_2}dl_2 \wedge (\mathbf{I_1}dl_1 \wedge \hat{\mathbf{r}}_0) \tag{3.3}$$

where $d\mathbf{F_2}$ is the force acting on the image element at position 2 due to the current element at position 1, can be used to calculate the axial UMP by summing the forces between current elements and image current elements. Each current element in a single rotor magnet is attracted or repulsed by each current element in its images 1 to 6 in Fig.(3.11), but as it is $\propto 1/r^2$ the effect of distant images is small. Similarly, the effect of the images of neighboring magnets needs to be accounted for. Because the permeability of the magnets is being ignored, neighbours do not change the reluctance of the magnetic circuits, and the fluxes simply superimpose (assuming no saturation effects in the steel), adding or subtracting. Nevertheless this gives a different magnetic field distribution and in principle, different UMP.

Fig.(3.12) shows some of the calculation details for one face of a magnet and image 1. Each of the $\mathbf{I_1}$ and $\mathbf{I_2}$ of Eq.(3.3) is replaced by B_r/μ_0, and dl_1 and dl_2 are the current element lengths which are either dx or dy depending on the

face. Considering the current elements of Face 1, and applying the geometry of the arrangement to Eq.(3.3), results in:

- An attractive force with all the mirror image elements of Face 1:

$$dF_2 = -\frac{{B_r}^2 dz^2 dx^2}{4\pi\mu_0 r^3}(z_2 - z_1)\hat{\mathbf{z}} \tag{3.4}$$

  where

$$r = \sqrt{(x_2 - x_1)^2 + (z_2 - z_1)^2} \tag{3.5}$$

  this is a downwards force (-ve sign) on the image current elements of the stator which means an upwards force for the rotor magnet.

- A repulsive force with all the mirror image elements of Face 3 which is the same as Eq.(3.4) except it is an upwards force (+ve) on the image current elements, and with

$$r = \sqrt{(x_2 - x_1)^2 + w_y^2 + (z_2 - z_1)^2} \tag{3.6}$$

  There is also a force to the right on the image current elements of the stator, but this is cancelled by the force between the current elements of *Face 3* with the image current elements of Face 1.

- A force to the right on the image current elements of Face 2, which is cancelled by a force to the left on the image current elements of Face 4.

These results for the effect of Face 1 current elements are replicated for the other 3 faces. For magnets where $w_y = w_x$, as for the aluminium and composite rotors, then the results for Face 1 are multiplied by 4, otherwise the calculation is re-done once for Face 2 and Face 4, with w_y replacing w_x.

This procedure is repeated for as many of the images as is required. Fig.(3.5) shows the results of 3 levels of approximation:

(i). **Biot Savart:** This only calculates the effect of image 1 as detailed above and then image 2, the UMP being the difference between the two forces

(ii). **Biot Savart with neighbour effects:** This adds in the effects of images 7, 8, 13, 14, noting that as the neighbouring magnets are of the opposite polarity forces are reversed eg whilst image 1 pulls the rotor down, image 7 pushes it up.

(iii). **Biot Savart with neighbour effects and 5th & 6th image effects:** This includes the effects of images 11, 12, 17, 18. Images 3, 4, 9. 10, 15, 16 are not calculated because the opposing pairs, eg 3 and 4, cancel out because they are the same distance from the rotor.

All calculations were performed to a relative convergence of 1%.

3.5 Discussion & Conclusions

3.5.1 Magnetic Forces

The experimental work on axial UMP forces show they are approximately proportional to axial offset. Biot-Savart calculations give close agreement to the experimental results, show that neighbour effects are small, and that the use of the first two images is adequate for calculations. However, there is no experimental data for when the rotor is very close to one stator ie when the offset is greater than approximately 80% of the nominal. The Biot-Savart calculations indicate that in this region, extrapolation of a straight line fit to the experimental data could underestimate the axial UMP forces by up to 30%. Ensuring that the rotor does not deviate by more than 80% of the nominal airgap would protect the structure from the predicted elevated axial UMP values.

The Biot-Savart calculations when the offset is equal to the nominal give the airgap closing force for a single sided machine, although not necessarily one that is equivalent to the double sided one in terms of output or optimized parameters.

For the 2 aluminium rotor tests, the radial centering forces are increased when the rotor is offset axially, but this effect is not seen for the other two rotors. This effect means that axial offset not only increases the airgap-closing axial force, but also any airgap-centering radial force due to radial offset. For all rotors the radial centering forces softly peak just before the magnets fully clear the airgap. For comparison, this maximum radial force ranges from 30 to 90% of the size of the axial forces when a radially centered rotor is displaced axially by half of the nominal airgap. The vector sum of the radial plus axial forces for the rotors when displaced both ways is shown in Fig.(3.13).

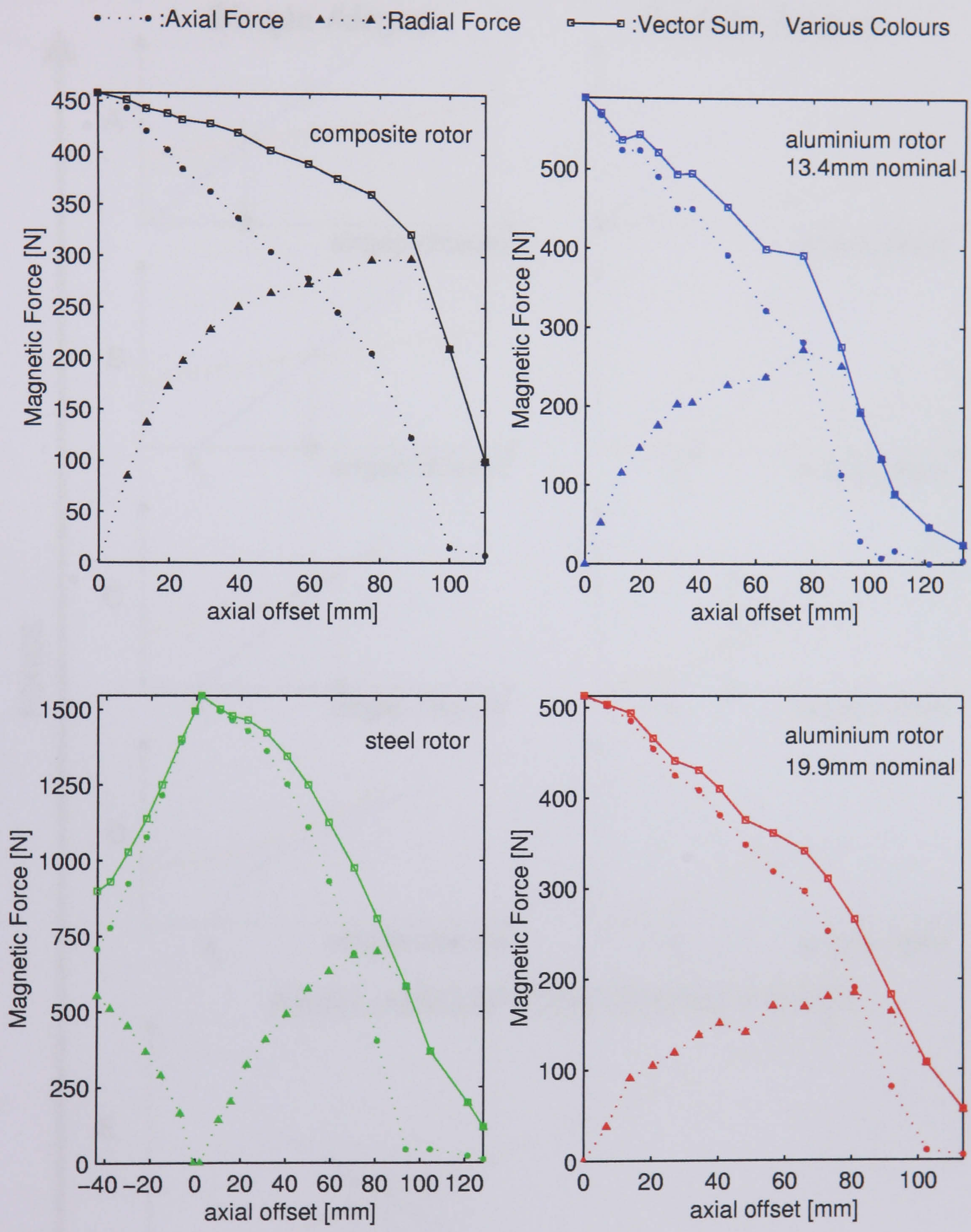

Figure 3.13: Combined Axial and Radial Forces when Axially and Radially Offset

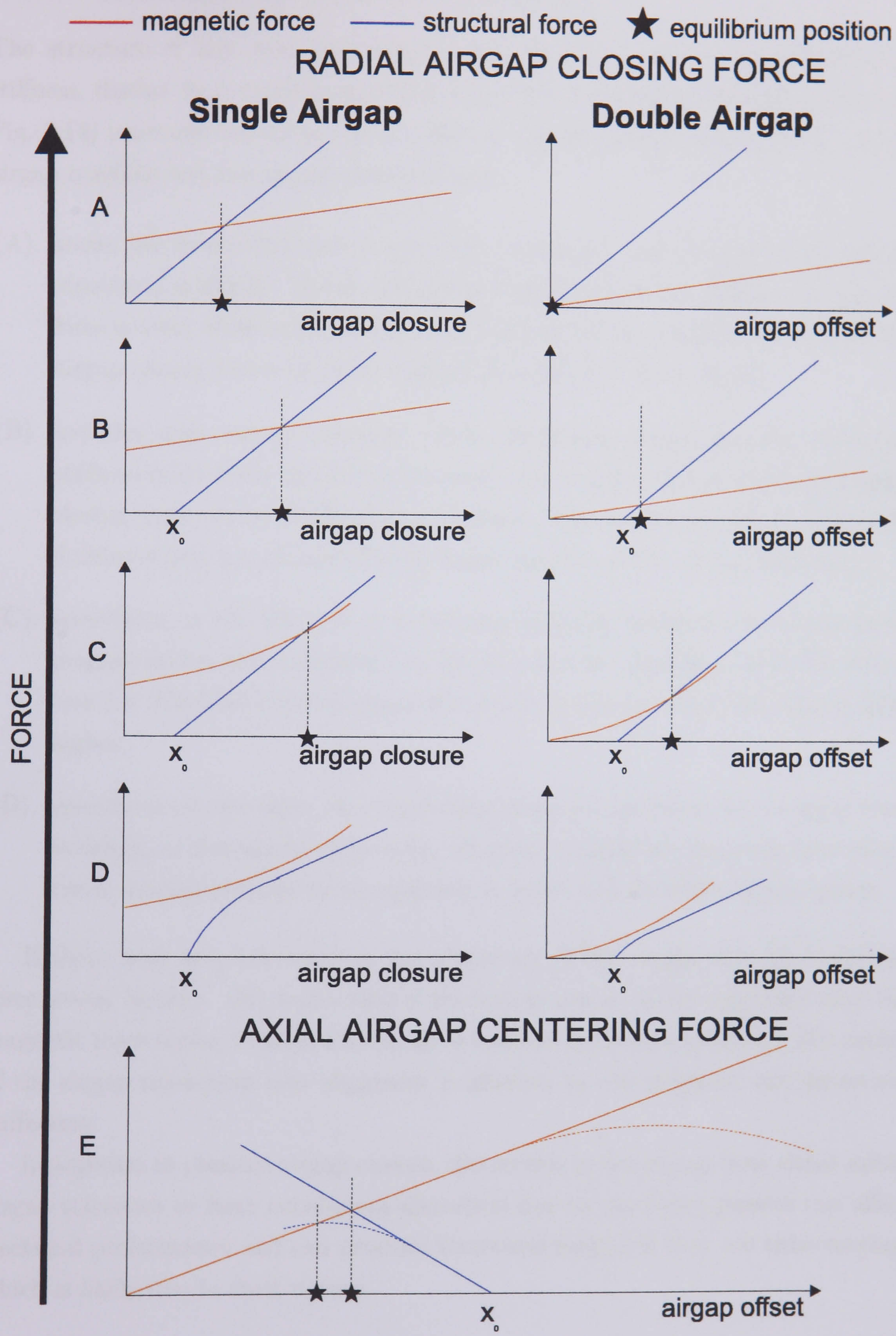

Figure 3.14: Magnetic Airgap Forces and Structural Restoring Forces

3.5.2 Influence on Machine Structure

The structure of any electrical machine will to some extent, depending on it's stiffness, distort as it establishes a restoring force to balance the magnetic forces. Fig.(3.14) contrasts the situation of a double airgap machine with that of a single airgap machine wrt the airgap closing forces:

(A). shows the theoretical case of zero airgap tolerance and constant magnetic and structural stiffness. The double sided machine needs no stiffness as the nett force is zero, whereas the single sided machine needs a stiffness that resists the airgap-closing forces at some reasonable reduction of the airgap.

(B). includes some airgap tolerance. Now the double airgap machine structural stiffness must resist the UMP, although this is less than the complete airgap-closing force of the single airgap machine. The latter now has an airgap reduction which has changed by the same amount as the airgap tolerance.

(C). speculates on the effect of an increasing magnetic stiffness due to non-linear magnetostatic effects as shown in the Biot-Savart calculation of UMP of Section 3.4. For both types of airgap this drives the airgap reduction/airgap offset higher.

(D). speculates on the effect of a decreasing structural stiffness, for example from buckling, or non-elastic behaviour, all quite possible for likely machine structures, leading perhaps to no equilibrium point and therefore airgap closure.

If there were zero tolerance on the alignment of the airgap then the centering force would be zero. (E) shows that if the airgap has an initial tolerance then the magnetic force trying to align the airgap is resisted by structural forces. The extent of the airgap movement into alignment is affected by the magnetic and structural stiffnesses.

In addition to possible airgap closure, distortions in the airgap from either initial airgap tolerance or from subsequent distortion due to the forces present can affect electrical performance and can produce structural fatigue if they are time-varying, which is likely due to their nature.

Chapter 4

Ironless Stator SLiM

Faced with the problems outlined in the Introduction relating to size and weight, the strength requirements evidenced in Chapter 2, and UMP arising from airgap tolerances investigated in Chapter 3, a radical departure from existing designs of direct drive generator is proposed in the form of a lightweight, spoked, prestressed structure used in conjunction with an ironless stator electromagnetic topology [9].

With prices for neodymium magnets dropping so quickly, the economic necessity for low reluctance magnetic circuits is diminishing. The ironless stator completely eliminates the airgap closing forces as the reluctance in the magnetic flux path no longer decreases as the airgap length decreases. Avoiding this large component of the magnetic forces nicely compliments the new structural approach.

The **S**poked, **Li**ghtweight, **M**achine structure, named SLiM, proposed for both the stator and the rotor, is similar to that employed in, for example, bicycle wheels, which demonstrate high stiffness and strength combined with low weight. Fundamentally, these attributes are achieved by avoiding buckling of slender structural members by prestressing.

4.1 Bicycle Wheels

Due to the similarity of the SLiM concept to a bicycle wheel, it is useful to consider their design and characteristics. A bicycle wheel is a prestressed structure. Prestress is achieved by shortening the spokes once the wheel has been built using special elongated nuts called 'nipples' which sit in holes in the rim and draw the threaded spoke ends through. This creates large amounts of tension in the spokes and compression, and some bending, in the rim. The porpoise of the prestress is to avoid compressive forces in the spokes during normal operation, thus allowing the use of many thin

spokes which would buckle under compressive forces to support a reduced stiffness rim. Bicycle wheels use this strategy to great effect, being strong, light, easy and cheap to build, the only disadvantage is that they have a large number of parts.

Setting aside modern departures such as composite (eg tri-spoke) wheels, traditional spoked designs vary in many aspects. For same diameter wheels, rim stiffness can vary greatly, due to material choice (normally steel or aluminium, but recently carbon fibre composite in high-end racing wheels) and cross section. For example the steel touring rim used by [10] has an in-the-plane-of-the-wheel second moment of area, I, of 752mm^4 which when multiplied by E, Young's Elastic Modulus, gives a bending stiffness, EI, of 158 compared with the lightweight aluminium rim used by [11] with an I of 1200mm^4 giving an EI of roughly half that at 84. Steel spokes are used, either 1.6 or 2mm diameter, sometimes butted which means their midsection is reduced by 0.2mm. Spoke number varies from as few as 16 (high performance road wheels with blade spokes and deep section rims) to 40, but is mostly 36. Various spoke patterns are in use, including simple radial, but most wheels use tangential spoking, which describes how the spokes leave the hub at an angle to the radius. The wheel in Fig.(4.1)(a) is termed a 3X (spoken "three cross") wheel because each spoke crosses 3 other spokes from its side of the hub as it extends from the hub to the rim. 2X and 4X patterns are also used. This is a good point to introduce another way of describing spoking patterns which is used for SLiM and is shown

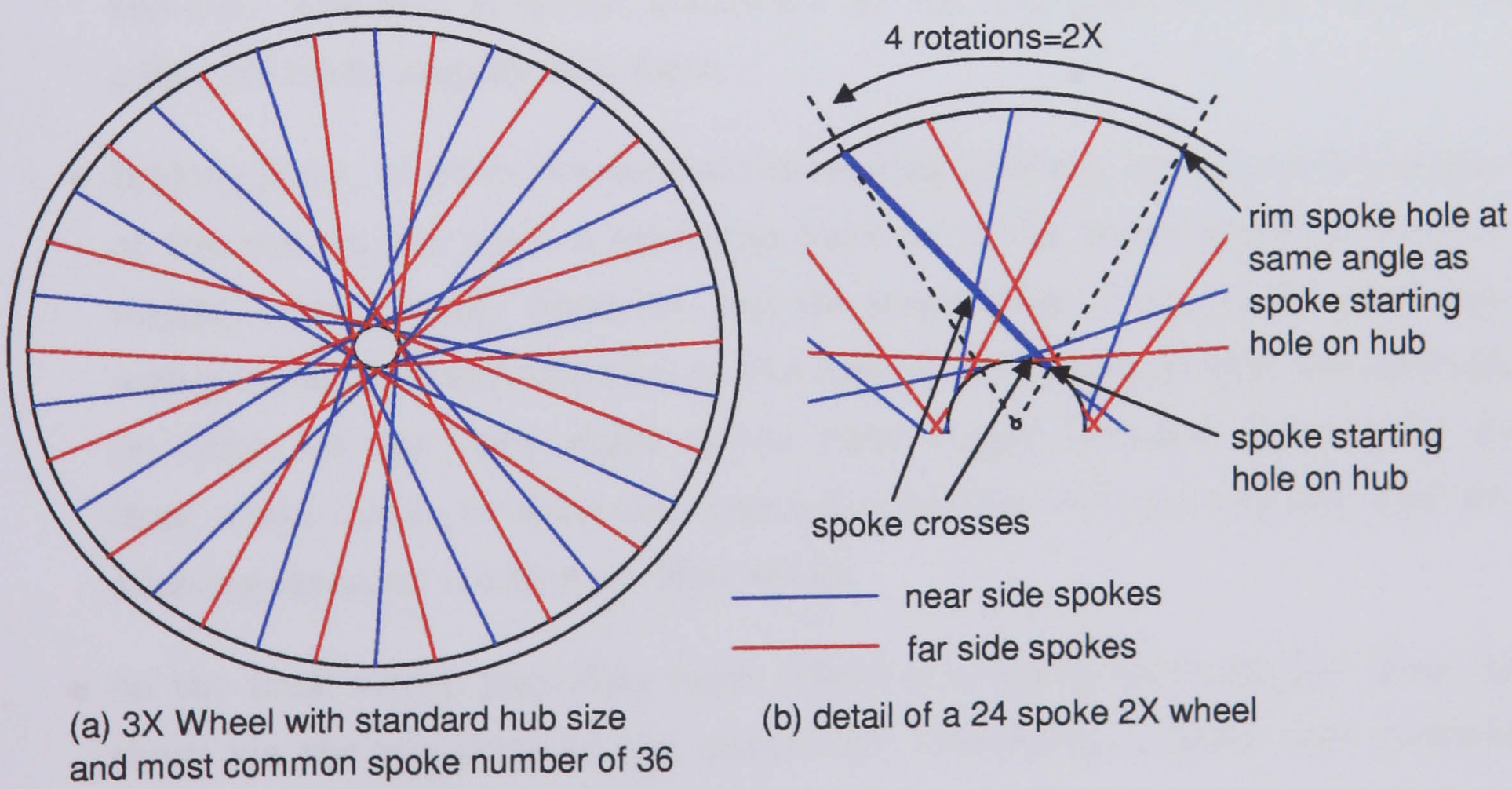

Figure 4.1: Typical Bicycle Wheel Spoke Patterns

in Fig.(4.1)(b), using 'rotations' which describe how to count around the rim spoke holes to find the correct attachment point for the spoke. 2X, 3X, 4X correspond to 4, 6, 8 rotations. This method is preferable as it is more generic across different spoking types.

All these traditional spoking designs have single spoke holes on the hub and rim, and the hub holes are rotated by half a hole pitch between the two sides of the hub, thus allowing simple and cheap spoke end connections and only one spoke length. There are various less common spoking patterns including:

- designs where 2 spokes meet at one point on the rim
- new rear racing wheel designs with tangential spoking on only one side of the wheel, and radial spoking on the other side. This means that the torque is being transmitted through only one side of the wheel.
- new racing wheel designs where the spokes laterally cross, presumably to increase lateral stiffness whilst not increasing wheel axle length.

Most good quality bicycle wheels have axial and radial tolerances at the rim in the region of ± 1mm. Bicycle wheels are subjected to various forces:

- rider weight force, which is a point compressive load between the rim on the road and the axle. Because the wheel is turning it is effectively moving around the rim. The load is spread somewhat by the tyre pressure, but bumps and going off curbs amplify this force.
- braking force, which is (for normal rim braking systems) an anti-clockwise force at the rim on the road, a clockwise force in at the brake which is normally roughly diametrically opposite, and the momentum of the bicycle and rider acting in the forward direction at the axle. This braking action will normally be larger on the front wheel as the rider weight transfers more on to the front wheel during braking thus increasing friction between tyre and road and allowing stronger braking on that wheel.
- on the back wheel, pedalling force, which is a torque force applied from the chain via the sprockets to the wheel hub, reacted by a point anti-clockwise load at the rim on the road.
- during turning the wheel tips and rider weight is reacted at the rim on the road by a force which is no longer purely radial, as it now has a lateral component.

Ref.[12] measures the stiffness of a bicycle wheel to forces similar to those found during use. This experimental work was investigating the effect of spoke pattern (radial, 1X, 2X, 3X, 4X), and found for a lightweight road wheel the following stiffness':

- 2300N/mm to point radial loads for deflection range 0 to 0.5mm, but this decreased with increased radial deflection up to 2.6mm for all wheels. The 3X wheel was loaded further and it's stiffness dropped to 250N/mm at the maximum tested deflection of 4.5mm, that is 1.5% of the wheel radius.
- 100N/mm to point axial loads for almost the entire measured range of 0 to 6.5mm, but tailing off to around 65N/mm for the last 1mm of deflection.
- torsional loads: 16Nm/degree for a radial spoking wheel, up to 320Nm/degree for 3X wheel. This was linear over the test range which was up to 50Nm for the radial spoking, 70Nm for the 1X, 2X, 3X spoking and 80Nm for the 4X spoking.

This gives a first indication of the relative stiffness', radial vs lateral vs torsional, of a SLiM structure of bicycle wheel size. As will be shown later, the exact details of how the stiffness' and buckling stability of these type of structures scale is not simple, and is dependent on the forces acting on them. The rim lateral stiffness will be proportional to I, the 2nd moment of area. Assuming a rim made of a prismatic beam this is proportional to m^4. The spoke stiffness in tension is, by comparison, proportional to cross sectional area divided by the length ie to m.

Considerable experimental and modelling work has been done on prestressed spoked wheels, mainly focussed on responses to the type of forces outlined above, either as bicycle wheels or as early prestressed spoked aeroplane wheels [13], [14], [15], [16], [17], [11], [10]. These are considered no further here, although they would perhaps be suitable for future work on the SLiM concept.

4.2 SLiM Structural Configuration

There are many ways in which the SLiM and ironless stator concepts can be combined, Fig.(4.2) shows some possible configurations. The choices can be classified thus:

- radial/axial airgap

- single/double sided airgap
- cantilevered/double sided stator/rotor
- internal/external rotor

It is hard to differentiate between all these choices at this early stage. However, some observations are:

- From experience of bicycle wheels, the axial tolerance of the rim might be harder to control than the radial tolerance. If this is true, a radial airgap, see Fig.(4.2)(b)&(d), would have a higher tolerance, allowing short, constant length airgaps, which are desirable.
- For a traditional machine using iron in the stator, the airgap could be arranged so these forces are in the direction of maximum structural stiffness i.e. radially in a bicycle wheel and in a SLiM, but with no iron, this force due to iron cores attracting has disappeared.
- A double sided airgap, see Fig.(4.2)(a)&(b) is an alternative technique to diminishing the problem of airgap closing forces in traditional machines by balancing airgap closing forces (although it relies on a high tolerance airgap). They add complexity to the machine.
- However, Section(4.6) will describe how, in an ironless stator, airgap forces due to the conductor current being in the airgap field are present which can either open or close the gap, depending on power factor. Therefore structural stiffness and/or double sided airgaps could still be needed to some extent.
- If one structure, stator or rotor, is inside the other one (i.e. the outer one is 'double sided') the outer one needs a rolling bearing on one side, see Fig.(4.2)(a) & (d), which is undesirable due to the extra cost. However, if the structures are side-by-side (ie 'cantilevered'), as in Fig.(4.2)(b)&(c) the whole machine becomes axially longer, which leads to a longer shaft, which is also unattractive.
- An external rotor layout has the advantage of reducing hub length.

On the basis of these, for this preliminary investigation, an ironless stator, radial flux, single sided airgap, double sided rotor, internal stator configuration is chosen, as in Fig.(4.2)(d). More details of the design are shown in Figs.(4.3)&(4.4).

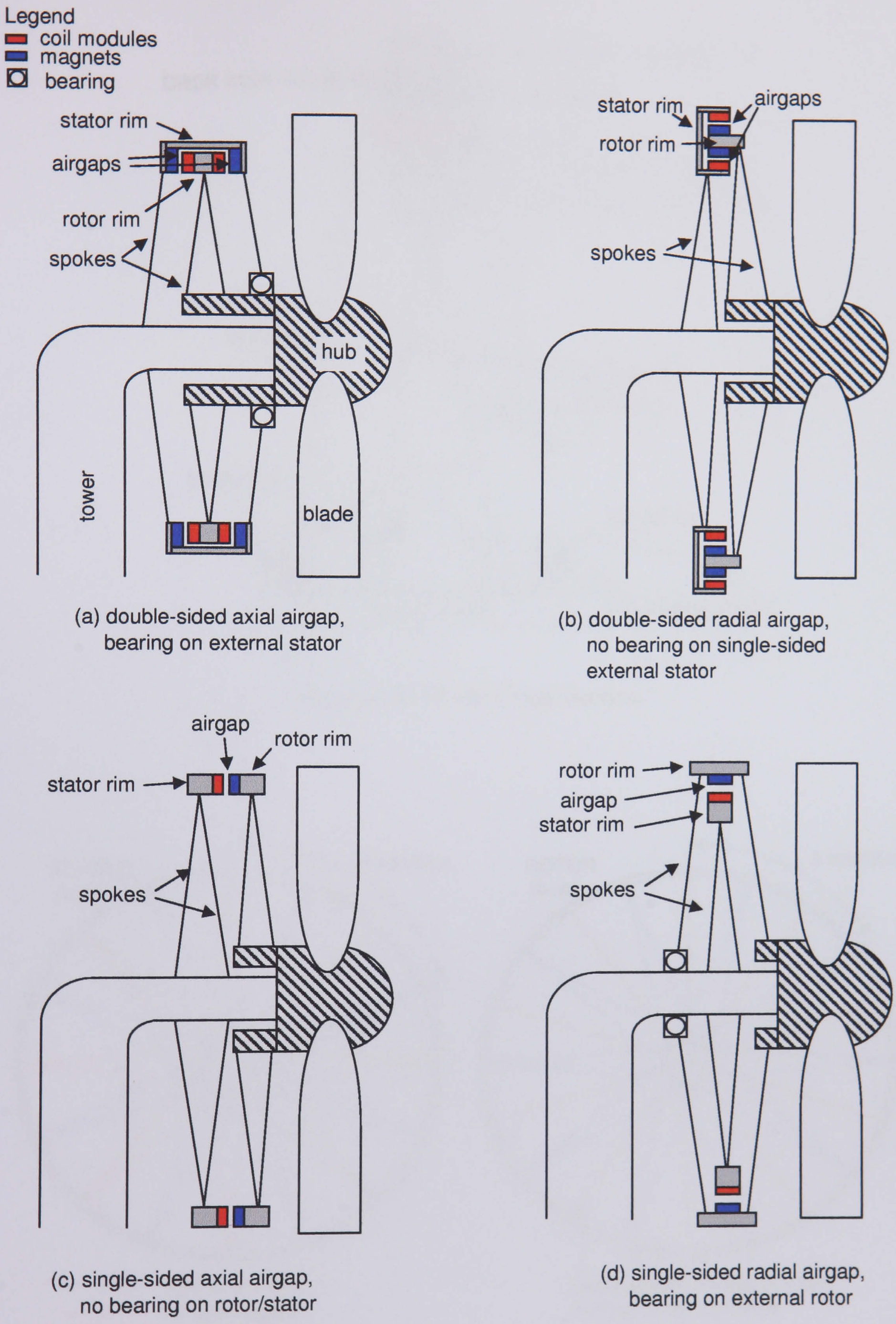

Figure 4.2: Possible Layouts for SLiM

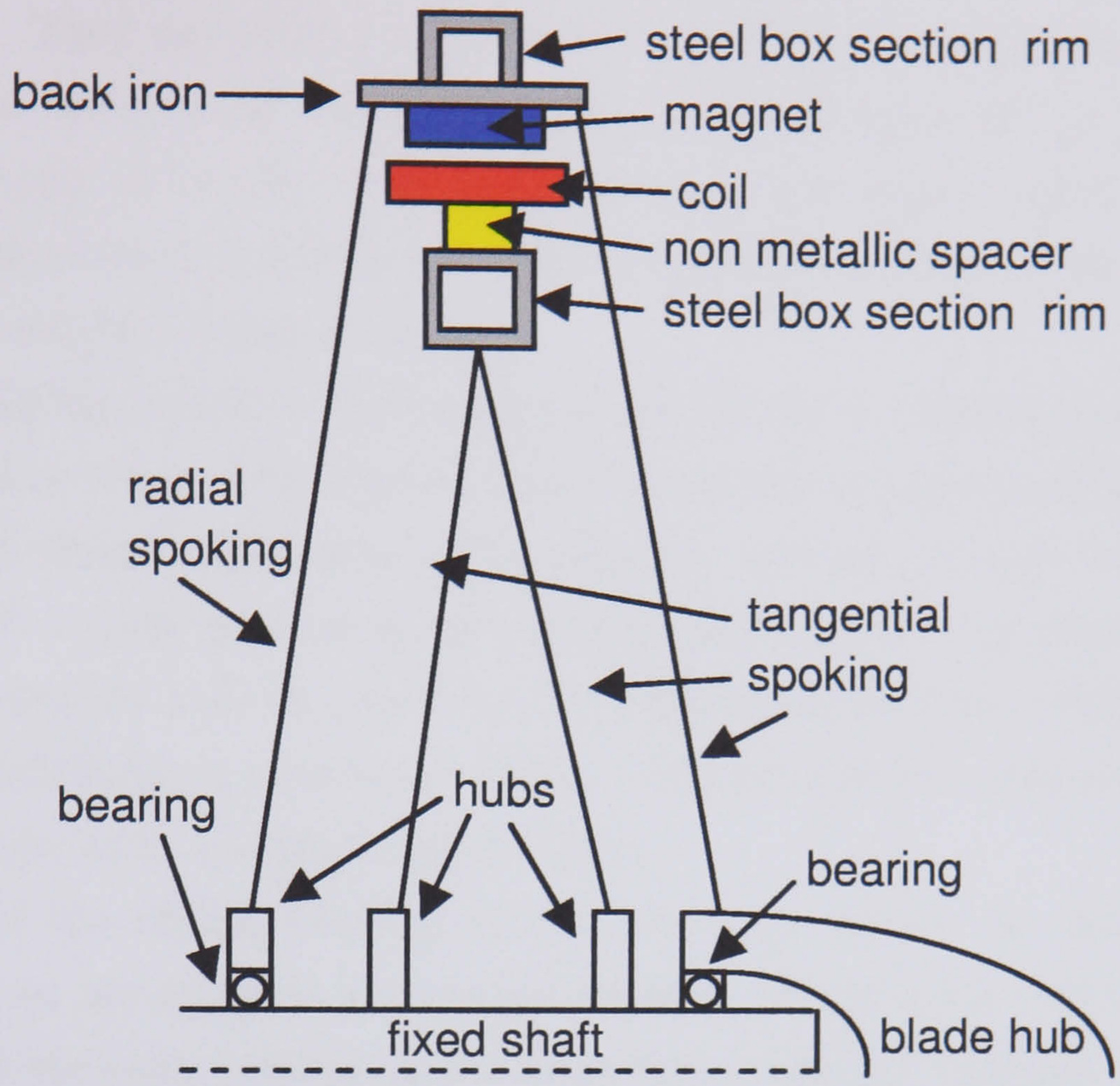

Figure 4.3: SLiM Cross Section

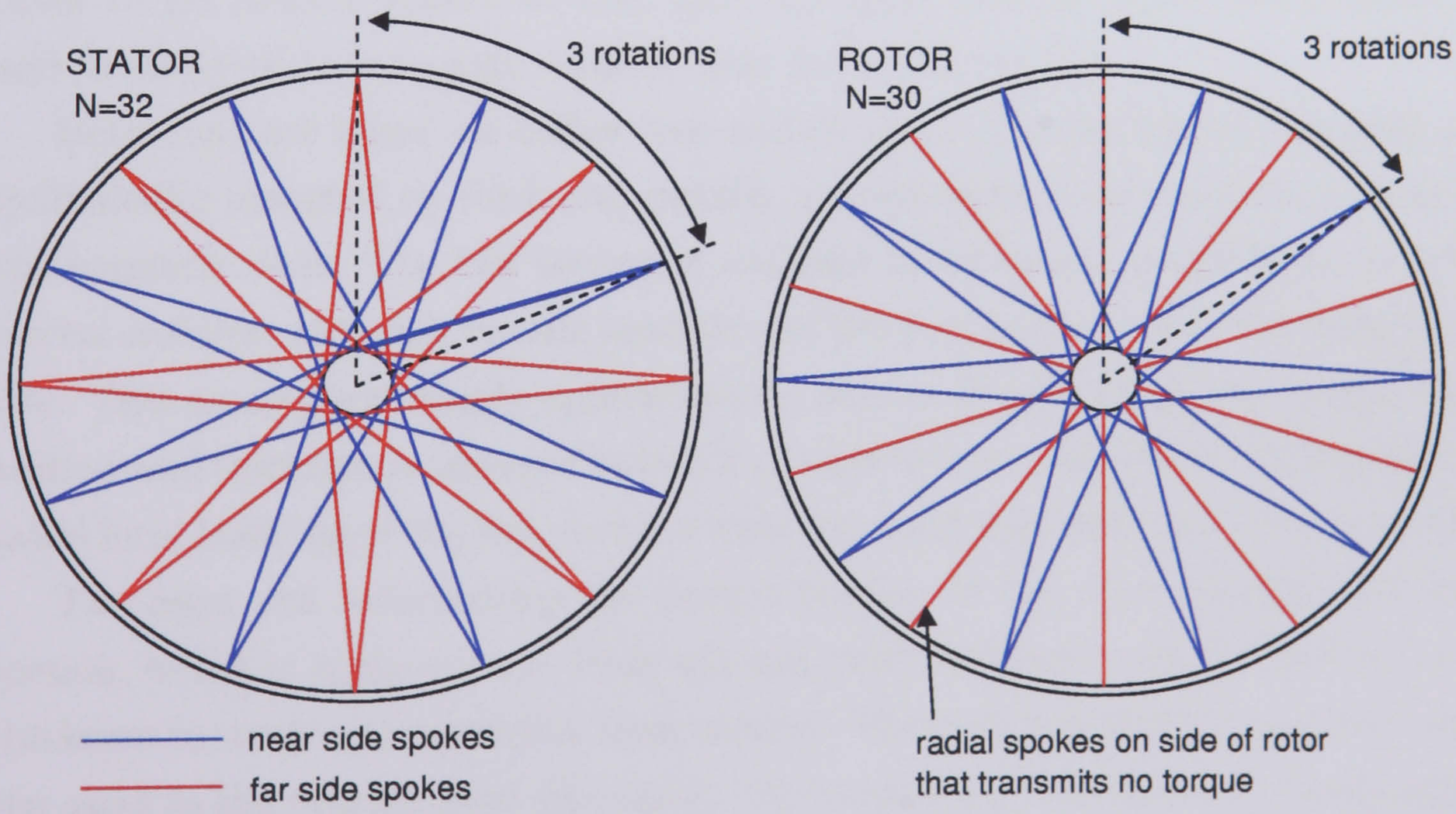

Figure 4.4: Choice of SLiM Spoke Pattern

The steel spokes are exposed to their maximum and minimum stresses during rated torque. They are sized and prestressed such that at maximum torque, the pulling spokes are stressed to the reversed stress fatigue limit, and the pushing spokes completely de-tension. Any compression in the spokes would lead to spoke buckling which in turn would create extreme bending stresses in the spokes. with local fatigue and/or yielding results.

Because during operation the pushing spokes partly de-tension, the rim becomes less supported by them. This negates that porpoise in the pattern normally found on bicycle wheels where pulling and pushing spokes alternate around the rim. Therefore, for SLiM, a spoke pattern is adopted that pairs pulling and pushing spokes at the rim and also the hub thus halving the connections on both. This pattern still leads to one hub flange's attachment points being rotated by a half pitch relative to the other flange, as in a normal bicycle wheel.

Because of the rolling bearing on the rotor, the spokes on that side do not resist torque, so are replaced with radial spoking. Keeping the radial spoking rim attachment at the same position as the tangential spoking it 'replaces' maintains the rim support in a similar fashion during operation. This leads to both hub flanges connection points being lined up on the rotor flanges. The radial spoking experiences no torque and so is prestressed up to the reversed stress fatigue limit.

The spoke patterns place constraints on the spoke number. For the stator, in order to get pairs of spokes on each side, the spoke number must have a factor 4, and similarly the rotor spoke number must have a factor of 3.

Both rims are based on hollow box section steel. For the stator, the coils are individually mounted on thick non-metallic spacers so that the steel rim is clear of the magnetic field. The box section is assumed to be square, which gives it some lateral stiffness, although the rim modelling of Section(4.4) only determines depth of rim. This assumption simply approximately mimics bicycle wheel rim design. Box section wall thickness is assumed to be 5% of outside dimension, which is sufficient to avoid local buckling of the rim, and is within standard wall thickness' used generally.

The rotor rim incorporates the central portion of the back iron into the box section, which is again square. Here the box wall thickness is set at the back iron thickness to create a symmetrical cross section. The back iron width is assumed to be the same as the magnet axial dimension. The remaining back iron not incorporated into the box section is assumed to have negligible structural use and is not factored into the rim design model.

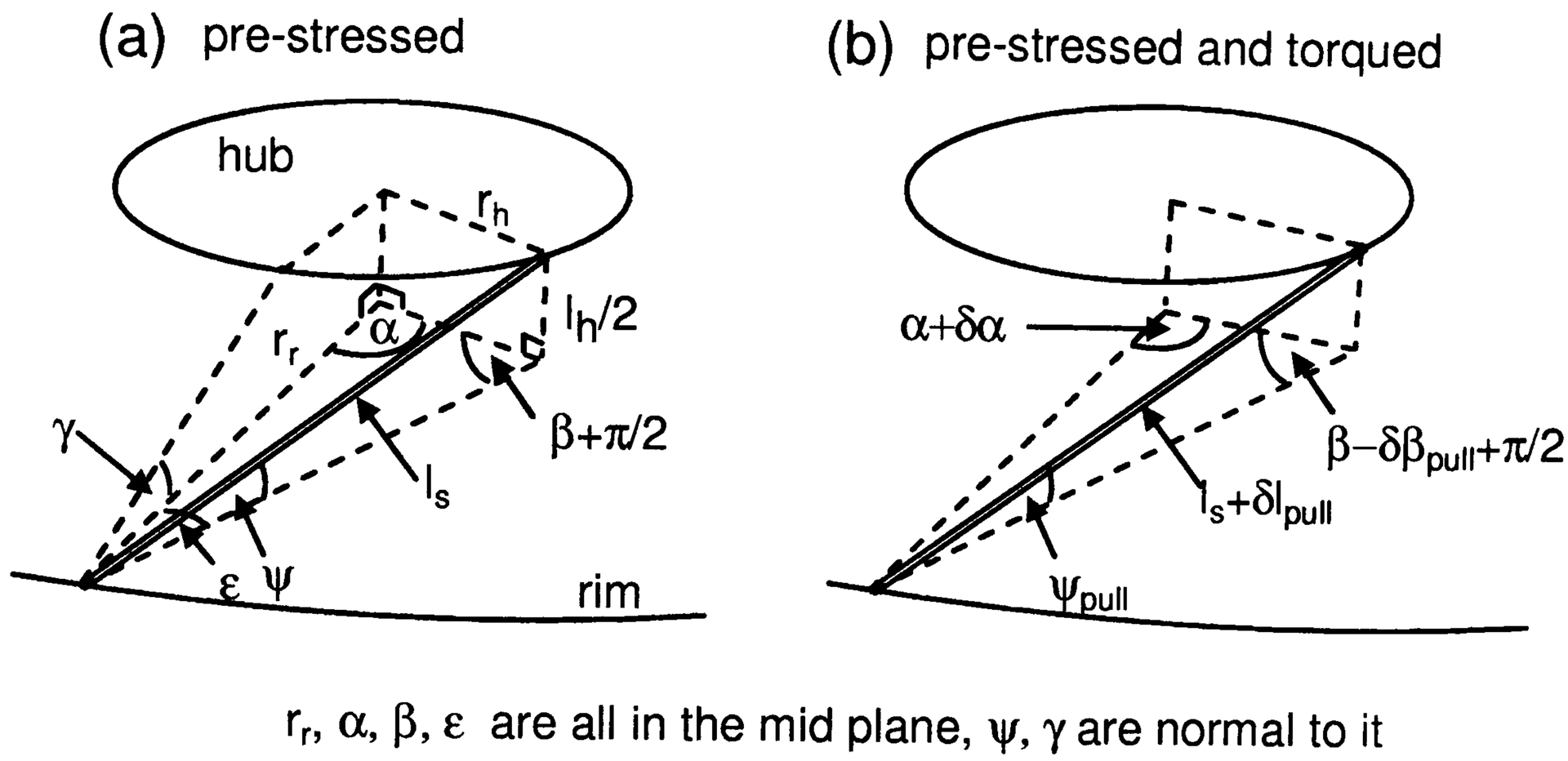

Figure 4.5: Wheel Geometries

4.3 Torque Force Models

Due to the high coil number, the torque force at the airgap is modelled as being constant around the rim. The model assumes that the rim radius r_r remains constant as torque is applied, this is discussed in Section(4.4). Three increasingly simple torque models are developed and compared for a range of possible configurations.

Third Order Model

Fig.(4.5) shows the 3D wheel geometry. The wheel is first pre-stressed and all the spokes, of cross-sectional area a_s, stretch by δ_{pre}, and the spoke stress is σ_0. As the wheel is subjected to torque, the rim rotates relative to the hub by an angle $\delta\alpha$. From a prestessed but untorqued spoke length of l_s, pulling spokes stretch by δl_{pull} and and pushing spokes shorten by δl_{push}, not by an equal amount due to the geometry involved. The spoke stress changes to σ_{pull} & σ_{push} for the pulling and pushing spokes respectively. The angle the spokes make to the tangent to the hub changes from a prestessed but untorqued value β, by $-\delta\beta_{pull}$ for the pulling spokes, and $+\delta\beta_{push}$ for the pulling spokes. The resulting torque balance at the hub is:

$$T = \frac{N r_h a_s}{2} \left[\sigma_{pull} \cos\psi_{pull} \cos\left(\beta - \delta\beta_{pull}\right) - \sigma_{push} \cos\psi_{push} \cos\left(\beta + \delta\beta_{push}\right)\right] \quad (4.1)$$

Where T is torque, N is number of spokes. There exist the following geometrical relationships for the wheel:

$$l_s = \sqrt{r_r^2 + r_h^2 - 2r_r r_h \cos\alpha + (l_h/2)^2} \tag{4.2}$$

$$\delta l_{pre} = l_s - \sqrt{{r_r}^2 + {r_h}^2 - 2r_r r_h \cos\alpha} \tag{4.3}$$

$$\delta l_{pull} = \sqrt{{r_r}^2 + {r_h}^2 - 2r_r r_h \cos(\alpha + \delta\alpha) + (l_h/2)^2} - l_s \tag{4.4}$$

$$\delta l_{push} = l_s - \sqrt{{r_r}^2 + {r_h}^2 - 2r_r r_h \cos(\alpha - \delta\alpha) + (l_h/2)^2} \tag{4.5}$$

$$\beta = \cos^{-1}\left(\frac{r_r \sin\alpha}{\sqrt{r_r^2 + r_h^2 - 2r_r r_h \cos\alpha}}\right) \tag{4.6}$$

$$\delta\beta_{pull} = \beta - \cos^{-1}\left(\frac{r_r \sin(\alpha + \delta\alpha)}{\sqrt{r_r^2 + r_h^2 - 2r_r r_h \cos(\alpha + \delta\alpha)}}\right) \tag{4.7}$$

$$\delta\beta_{push} = \cos^{-1}\left(\frac{r_r \sin(\alpha - \delta\alpha)}{\sqrt{r_r^2 + r_h^2 - 2r_r r_h \cos(\alpha - \delta\alpha)}}\right) - \beta \tag{4.8}$$

$$\cos\psi_{pull} = \frac{\sqrt{r_r^2 + r_h^2 - 2r_r r_h \cos(\alpha + \delta\alpha)}}{l_s + \delta l_{pull}} \tag{4.9}$$

$$\cos\psi_{push} = \frac{\sqrt{r_r^2 + r_h^2 - 2r_r r_h \cos(\alpha - \delta\alpha)}}{l_s - \delta l_{push}} \tag{4.10}$$

Eqns.(4.6),(4.7),(4.8) are presented in this form because they are used to inspect the values of these angles during the analysis. Eqns.(4.7)-(4.10) are combined and terms cancel to give

$$\cos(\beta - \delta\beta_{pull})\cos\psi_{pull} = \frac{r_r \sin(\alpha + \delta\alpha)}{l_s + \delta l_{pull}} \tag{4.11}$$

and

$$\cos(\beta + \delta\beta_{push})\cos\psi_{push} = \frac{r_r \sin(\alpha - \delta\alpha)}{l_s - \delta l_{push}} \tag{4.12}$$

So Eq.(4.1) can be rewritten:

$$T = \frac{N r_h a_s}{2}\left[\frac{\sigma_{pull}\sin(\alpha + \delta\alpha)}{l_s + \delta l_{pull}} - \frac{\sigma_{push}\sin(\alpha - \delta\alpha)}{l_s - \delta l_{push}}\right] \tag{4.13}$$

If the same stress criteria is applied to both pulling and pushing spokes ie the wheel can be subjected to torque in both directions ie pulling spokes become pushing

spokes and visa versa, then total stretch $\delta l_{pull} + \delta l_{push}$ is dictated by the spoke material properties. The following stress-strain relationships exist for the spokes, where E_s is the Young's Modulus of the spoke material:

$$E_s = \frac{\sigma_0 \left(l_s - \delta l_{pre}\right)}{\delta l_{pre}} \tag{4.14}$$

$$E_s = \frac{\sigma_{pull} \left(l_s - \delta l_{pre}\right)}{\delta l_{pull} + \delta l_{pre}} \tag{4.15}$$

$$E_s = \frac{\sigma_{push} \left(l_s - \delta l_{pre}\right)}{\delta l_{pre} - \delta l_{push}} \tag{4.16}$$

$$\sigma_0 = \frac{\sigma_{push}\delta l_{pull} + \sigma_{pull}\delta l_{push}}{\delta l_{push} + \delta l_{pull}} \tag{4.17}$$

Therefore, if σ_{pull} & σ_{push} are chosen using material strength limits, δl_{pull}, δl_{push} and $\delta\alpha$ need to be found in order to size spoke cross section a_s for a given torque requirement. Manipulation of Eqs.(4.14)-(4.17), (4.4)&(4.5) would be difficult, but Goal Seek can be easily set up in a Microsoft Excel spreadsheet to find the correct prestress σ_0 that will result in the required σ_{pull} & σ_{push} [1].

Second and First Order Models

If spoke length change is found from $\mathrm{d}l_s/\mathrm{d}\alpha$, a simplified second order model results, and Eqns.(4.4)&(4.5) modify to:

$$\delta l_{pull} \approx \delta l_{push} = \delta l = \frac{r_r r_h \sin\alpha}{\sqrt{r_r^2 + r_h^2 - 2r_r r_h \cos\alpha}}\delta\alpha \tag{4.18}$$

thus ignoring the small difference between δl_{pull} and δl_{push}. Now Eqns.(4.15)-(4.17) simplify to:

$$E_s = \frac{\sigma_{pull} \left(l_s - \delta l_{pre}\right)}{\delta l + \delta l_{pre}} \tag{4.19}$$

$$E_s = \frac{\sigma_{push} \left(l_s - \delta l_{pre}\right)}{\delta l_{pre} - \delta l} \tag{4.20}$$

[1]Goal Seek is part of a suite of commands sometimes called what-if analysis (what-if analysis: A process of changing the values in cells to see how those changes affect the outcome of formulas on the worksheet). When you know the desired result of a single formula but not the input value the formula needs to determine the result, you can use the Goal Seek feature available by clicking Goal Seek on the Tools menu. When goal seeking, Microsoft Excel varies the value in one specific cell until a formula that's dependent on that cell returns the result you want.

$$\sigma_0 = \frac{1}{2}\left(\sigma_{push} + \sigma_{pull}\right) \tag{4.21}$$

and now δl can be found directly from Eqns.(4.19)-(4.21)&(4.14):

$$\delta l = \frac{l_s\left(\sigma_{pull} - \sigma_{push}\right)}{2E_s + \sigma_{pull} + \sigma_{push}} \tag{4.22}$$

and Eq.(4.18) gives $\delta\alpha$.

A further simplification to create a first order model is made by ignoring the effect of wind-up on the angle the spoke tensions make at the hub. This changes Eq.(4.1) to

$$T = \frac{N r_h r_r a_s \sin\alpha}{2 l_s}\left(\sigma_{pull} - \sigma_{push}\right) \tag{4.23}$$

Results

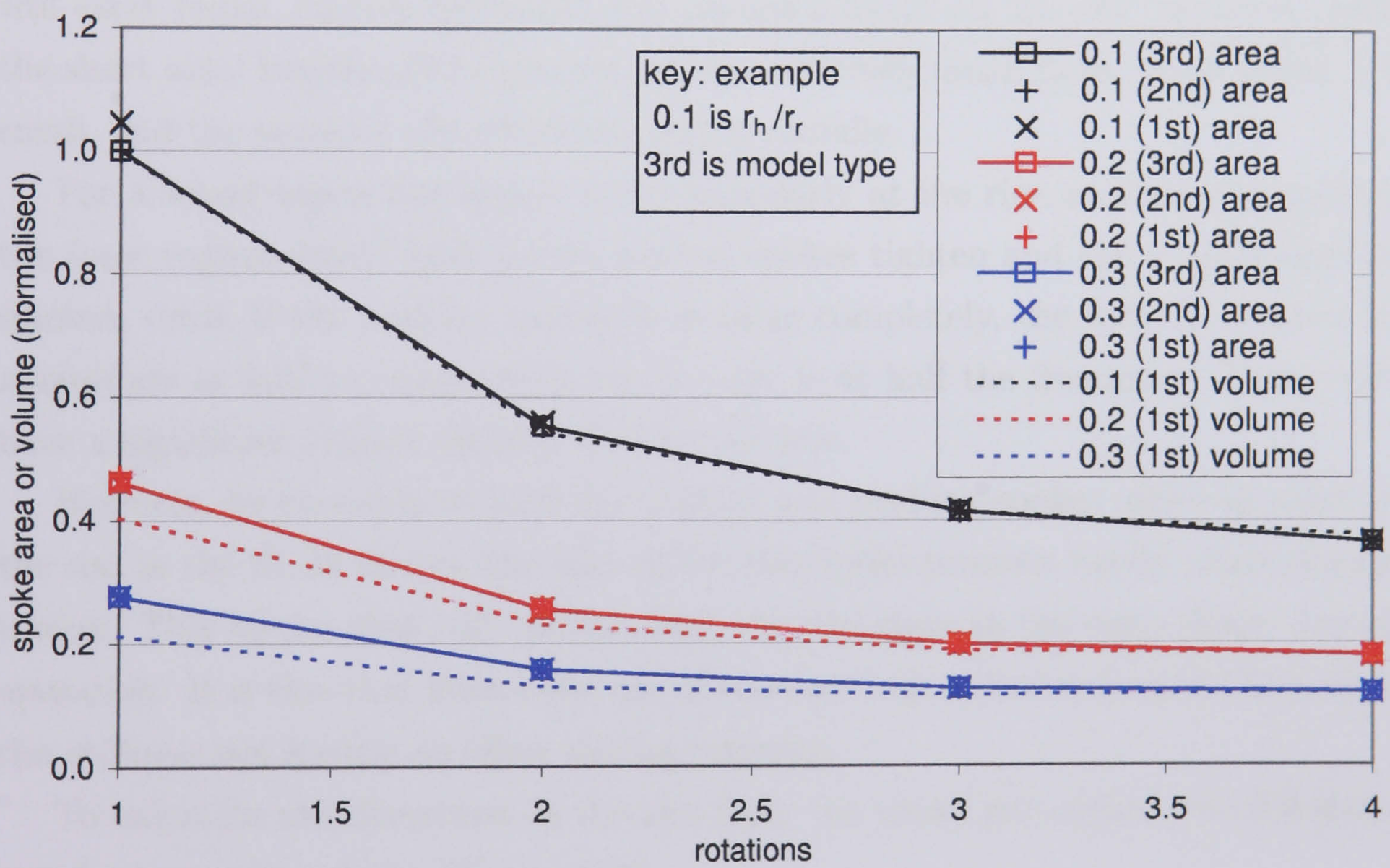

Figure 4.6: Comparison of Torque Models and Effects of Spoke Rotation and Hub Radius

Fig.(4.6) shows a comparison of these three torque models at likely maximum and minimum hub/rim ratios, and for all the rotations possible for a 40 spoke wheel. It also shows how the required spoke cross sectional area, a_s, compares

with the base case of $r_h/r_r = 0.1$, for 1 rotation. Finally it multiplies these a_s by the spoke length to give spoke volume compared with the same base case. In the comparison $\sigma_{push} = 0$, which maximises any differences between the models as it allows maximum wind up.

4.4 Rim Design

For the generator there must be some tolerance required at the airgap to avoid airgap rubbing and also for power quality and effective electromagnetic design.

The rims of the stator and rotor are subjected to point loading from the spokes, and electromagnetic torque and lateral wind forces both applied uniformly around the rims. The local effects of the latter two can be neglected at this stage. The angles the spokes have at the rim, ϵ, ψ, see Fig.(4.5)(a), depend on spoke number, spoke rotation, hub/rim radius ratio and hub length. This means that the spokes will exert radial, circum-referential and torsional forces on the rim. However, with the short axial lengths of the generators, and relatively small hubs, these angles are small, and the tensions are effectively acting radially.

For a wheel where the spokes arrive singularly at the rim, as torque is applied the force regime would alter as the pulling spokes tighten and the pushing spokes slacken, until, if the pushing spokes de-tension completely, the force is doubled in magnitude at half as many points on the rim ie at half the frequency. This could have a significant impact on how the rim behaves.

However, by choosing to have the pulling and pushing spokes arrive in pairs at the rim in the SLiM design, the sum of the two spoke tensions barely alters during torque. This means that once prestressed, the rim stays in the same shape during operation. It is this that allows the use of constant rim radius in Section(4.3), with rim stiffness not having an effect during torquing.

To calculate the distortion in the rim from the spoke pretension, the following standard equations from [18] are used:

$$\delta r_{spoke} = -\frac{F r_r^3}{EI}\left[\frac{k_1\left(\theta - \sin\theta\cos\theta\right)}{4\sin^2\theta} + \frac{k_2\cos\theta}{2\sin\theta} - \frac{k_2^2}{2\theta}\right] \tag{4.24}$$

$$\delta r_{mid} = \frac{F r_r^3}{EI}\left[\frac{k_1\left(\sin\theta - \theta\cos\theta\right)}{4\sin^2\theta} - \frac{k_2}{2\sin\theta} + \frac{k_2^2}{2\theta}\right] \tag{4.25}$$

where r_{spoke} & r_{mid} are the deflections of the rim at the spoke connections and halfway between them respectively, and are positive with increasing r_r. F is the

spoke force at that point, I is the second moment of inertia in the plane of the wheel, 2θ is angle between spoke attachments. $k_1 = 1 - \alpha + \beta$, $k_2 = 1 - \alpha$ where $\alpha = I/Ar_r^2$ the hoop stress deformation factor (for thin rings) and $\beta = FEI/GAr_r^2$ the radial shear deformation factor (for thin rings). A is the cross sectional area of the rim, F is the shape factor for the cross section, G is the shear modulus. The shape factor, F, used for both the rim and the stator is for box section. in spite of the additional back iron strips on the rotor rim. For box section:

$$F = \left[1 + \frac{3\left(D_2^2 - D_1^2\right) D_1}{2D_2^3}\left(\frac{t_2}{t_1} - 1\right)\right]\frac{4D_2^2}{10r^2} \tag{4.26}$$

where D_1 & D_2 are the distance from the neutral axis to the inner and outer surfaces of the flange, respectively, t_1 is the thickness of the webs, t_2 is the thickness of the flanges, and $r = \sqrt{I_x/A}$, the radius of gyration about the neutral axis.

Eqns.(4.24) & (4.25) allow the range of deflection to be found for each rim. Any change in the average radius from being unstressed is ignored as in a real machine knowledge of it would allow a correction at the design stage. Adding the range from both rims together gives the airgap variation.

4.4.1 Wheel Buckling

Bicycle wheels are susceptible to buckling failure, and this could also be true of the SLiM rotor and stator. The subject is a complex one, but some simple calculations were used to estimate the limits of stability in the plane of the wheel. This may not be the worst case, but no simple models of alternative buckling modes were found, and development of them was considered beyond the resources of the present work.

Two alternative calculations were looked at, both from [19]. Firstly, the stator was assumed to be just the rim alone, with no spokes, and the spoke tensions were taken as a uniform radial inward pressure. The critical compressive force in the rim at which buckling occurs can be found from:

$$F_{cr} = \frac{3EI}{R_r^2} \tag{4.27}$$

where E is modulus of the rim material, I is the second moment of area of the rim and R_r is rim radius. The compressive force in the rim ie hoop stress, is found from the spoke tensions:

$$F = \frac{a_s \sigma_0 N}{2\pi} \tag{4.28}$$

where a_s is the spoke cross sectional area, σ_0 is the spoke stress and N is the number of spokes.

Secondly, the stator was assumed to be a long straight beam on an elastic foundation, with the spokes assumed to be a continuous elastic support. The full exposition of this is left to [19], the critical compressive force is:

$$F_{cr} = \frac{\pi^2 EI}{L^2} \tag{4.29}$$

which if L were the length of the beam, l, would be the Euler formula with hinged ends. However, L is instead a reduced length which takes account of the elastic support. The choice of L/l depends on the support stiffness per unit length (ie spoke number and cross section), the beam length (ie distance between spokes), and rigidity. Values for L/l were taken from a lookup table in [19]. Actual beam length is taken as the circumference of the rim.

4.5 Aerodynamic Forces

These include windage on the rotor spokes and the rotor rim, and because the generator is not enclosed in a nacelle, lateral wind forces on both the stator and the rotor. The windage losses are not considered significant at this stage and are neglected. It is usual for this type of calculation to use the Germanischer Lloyd standard of 50 year return gust speed for a wind turbine class I site as a worst case storm wind speed, which is 70m/sec [20].

There are two criteria that the generator has to fulfill with respect to this storm wind loading. Firstly, the downwind spokes have to maintain some tension to avoid buckling and the upwind spokes have to remain below the material limit, and secondly, some limit has to be placed on the lateral movement of the rim. Whilst to some extent the stator and rotor rims will move in unison, differences in the rim and spokes, and aerodynamic coupling between the two, will mean that the rims cannot be assumed to deflect the same and so it is better to design for a deflection which can then be factored in to any clearance, such as to avoid collision. This deflection is fairly arbitrarily chosen as 30mm. The length of the hub that contributes to the cone angle of the spokes, l_h, is adjusted to fulfill these criteria.

Fig.(4.7) shows the layout and notation for the calculation. The spokes are approximated to radial. The force from the wind is calculated using:

$$F_{wind} = \frac{1}{2}\rho_{air} v^2 A \tag{4.30}$$

where ρ_{air} is air density at 20°C, v is the storm force wind speed, A is the normal cross sectional area of 2 spokes plus their fraction of the total rim circumference, which is:

$$A = 2\phi_s (r_r - r_h) + \frac{4\pi r_r d}{N} \qquad \text{(stator)} \tag{4.31}$$

$$A = \frac{1}{2}(2\phi_s + \phi_r)(r_r - r_h) + \frac{3\pi r_r d}{N} \qquad \text{(rotor)} \tag{4.32}$$

where ϕ_s is spoke diameter of the stator spokes and also the tangential spoking on the rotor, $(r_r - r_h)$ is the spoke length normal to the wind, d is radial depth of

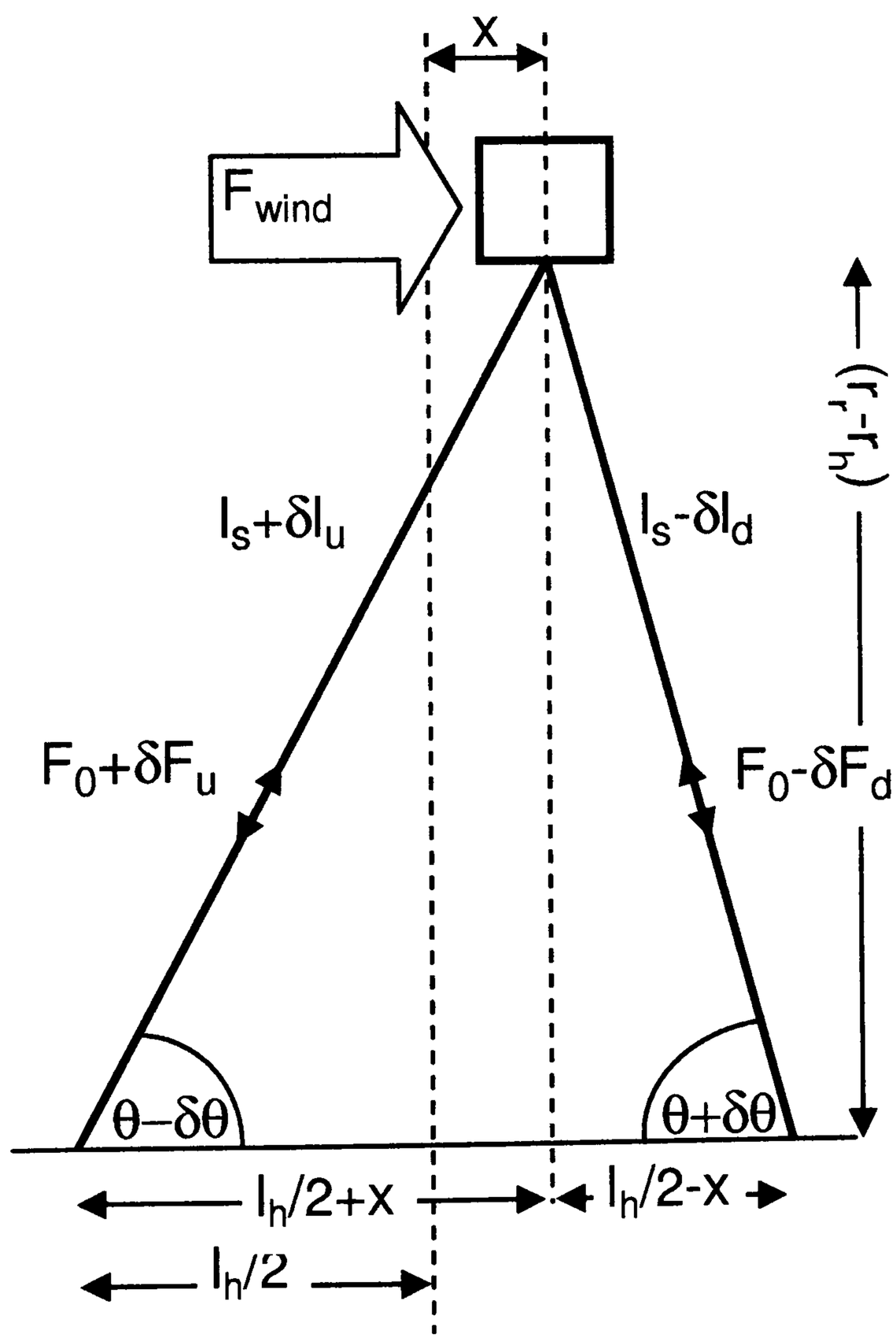

Figure 4.7: Details of lateral deflection from wind load calculation

rim, N is total spokes on the wheel.

This F_{wind}, from both spoke and rim wind loading, is assumed to be concentrated at the rim, which simplifies the model at the same time as overestimating its effect. The drag coefficient is approximated to 1, it's real value is in the range 1 to 1.3 for the two profiles, rim and spoke. The lateral force balance is:

$$F_{wind} + (F_0 - \delta F_d)\cos(\theta + \delta\theta_d) - (F_0 + \delta F_u)\cos(\theta - \delta\theta_u) = 0 \tag{4.33}$$

The following geometrical relationships apply:

$$l_s = \sqrt{(r_r - r_h)^2 + l_h^2/4} \tag{4.34}$$

$$l_s + \delta l_u = \sqrt{(r_r - r_h)^2 + (l_h/2 + x)^2} \tag{4.35}$$

$$l_s - \delta l_d = \sqrt{(r_r - r_h)^2 + (l_h/2 - x)^2} \tag{4.36}$$

$$\cos(\theta + \delta\theta_d) = \frac{l_h/2 - x}{l_s - \delta l_d} \tag{4.37}$$

$$\cos(\theta - \delta\theta_u) = \frac{l_h/2 + x}{l_s + \delta l_u} \tag{4.38}$$

as do the two elasticity equations:

$$E_s = \frac{\delta F_u l_s}{\delta l_u a_s} \tag{4.39}$$

$$E_s = \frac{\delta F_d l_s}{\delta l_d a_s} \tag{4.40}$$

Excel Goal Seek can be used with Eqns.(4.33)-(4.40) to find the spoke tension changes and the lateral deflection. The hub length can then be adjusted and the Goal Seek repeated until the deflection is acceptable.

4.6 Ironless Stator Field-Current Interaction Forces

Now that there is no stator iron to channel the flux around the windings. the conductor windings are in the full field and as such are subjected to a force due to the magnetic field at that point:

$$d\mathbf{F} = \mathbf{I}dl \wedge \mathbf{B} \tag{4.41}$$

To look at the nature of the forces on the coil, the simplified arrangement of an N-turn concentrated 2D coil in a 2D field comprised of the fundamental B field is investigated. Then the analysis is extended to include the 3D effects. If the variation of the field in the z-direction were included it would allow some assessment of UMP for axial and radial tolerance variation, but this is ignored for both 2D and 3D as it was thought the method does not merit further extension due to it's approximations.

4.6.1 2D Analysis

Fig.(4.8) shows the layout of the 2D simplified physical model including the assumed fundamental field and the concentrated coil. For a 2D machine we can say $\mathbf{I} = I_y\hat{\mathbf{y}}$, $\mathbf{B} = B_x\hat{\mathbf{x}} + B_z\hat{\mathbf{z}}$ and Eq.(4.41) becomes

$$d\mathbf{F} = F_x + F_z = I_y(B_z\hat{\mathbf{x}} - B_x\hat{\mathbf{z}}) \tag{4.42}$$

If electrical degrees, θ_e, are used to define x-position, the z and x components of the fundamental field are:

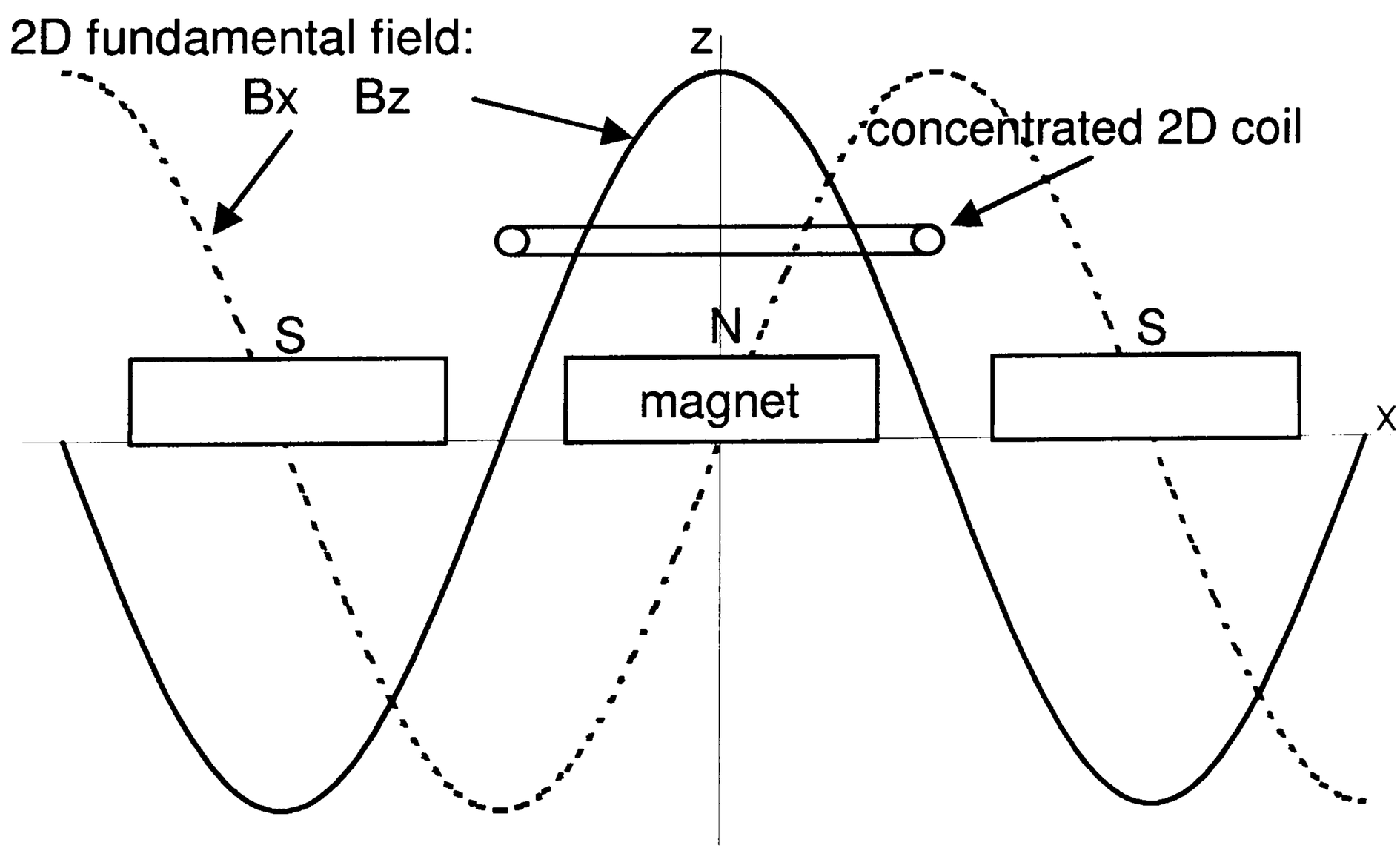

Figure 4.8: Layout of 2D machine

$$B_z = \widehat{B}\cos\theta_e \tag{4.43}$$

$$B_x = \widehat{B}\sin\theta_e \tag{4.44}$$

where $\theta_e = (\pi/\tau)x$ and $\widehat{B}$ is the peak field. Because the rotor is moving in the positive x-direction, the stator coil sees at time t:

$$B_z = \widehat{B}\cos(\theta_0 - \omega_e t) \tag{4.45}$$

$$B_x = \widehat{B}\sin(\theta_0 - \omega_e t) \tag{4.46}$$

where ω_e is rotor electrical frequency, t is time and θ_0 is the θ_e position at $t = 0$. If the coil is centred above a north pole at $t = 0$ then the x positions of the left and right conductors are $-f\pi/2$ and $f\pi/2$ where f is the fractional pitch of the coil eg $f = 1$ for a full pitch winding. The fields they see are therefore:

$$B_z(l) = \widehat{B}\cos\left(-\frac{f\pi}{2} - \omega_e t\right), \quad B_z(r) = \widehat{B}\cos\left(\frac{f\pi}{2} - \omega_e t\right) \tag{4.47}$$

$$B_x(l) = \widehat{B}\sin\left(-\frac{f\pi}{2} - \omega_e t\right), \quad B_x(r) = \widehat{B}\sin\left(\frac{f\pi}{2} - \omega_e t\right) \tag{4.48}$$

where l and r refer to the left and right hand side of the coil respectively. The induced emf is the sum of the voltages on each side of the coil:

$$E = Nl_c v\left(B_z(l) + B_z(r)\right) \tag{4.49}$$

where l_c is the length of the coil on each side, and v is the velocity of the coil. Because $v{=}\omega r{=}\omega_e rp/2$ where p is the pole number, and $r/p{=}\tau\pi$:

$$E = 2Nl_c\omega_e\tau\pi\left(B_z(l)l_c + B_z(r)l_c\right) \tag{4.50}$$

$I_y{=}E/Z$ where Z is the impedance of the coil plus load in the circuit, so:

$$I_y = \frac{2N\widehat{B}l_c\omega_e\tau\pi}{Z}\left[\cos\left(-\frac{f\pi}{2} - \omega_e t + \phi\right) + \cos\left(\frac{f\pi}{2} - \omega_e t + \phi\right)\right] \tag{4.51}$$

where ϕ accounts for inductive lag/capacitative lead. This simplifies to:

$$I_y = \frac{4N\widehat{B}l_c\omega_e\tau\pi}{Z}\sin\left(\frac{f\pi}{2}\right)\sin(\omega_e t + \phi) \tag{4.52}$$

Current in the rhs/lhs conductor is +ve/-ve respectively. F_x and F_z from Eq.(4.42) can be written:

$$F_x = I_y(l)B_z(l) + I_y(r)B_z(r) \tag{4.53}$$

$$F_z = -I_y(l)B_x(l) - I_y(r)B_x(r) \tag{4.54}$$

i.e.

$$F_x = K\sin\left(\frac{f\pi}{2}\right)\sin\left(\omega_e t + \phi\right)\left[-\cos\left(-\frac{f\pi}{2} - \omega_e t\right) + \cos\left(\frac{f\pi}{2} - \omega_e t\right)\right] \tag{4.55}$$

$$F_z = -K\sin\left(\frac{f\pi}{2}\right)\sin\left(\omega_e t + \phi\right)\left[-\sin\left(-\frac{f\pi}{2} - \omega_e t\right) + \sin\left(\frac{f\pi}{2} - \omega_e t\right)\right] \tag{4.56}$$

where $K{=}4N\widehat{B}^2 l_c \omega_e \tau\pi/Z$. These two equations can be condensed, but the separation of the left and right conductor forces is lost:

$$F_x = 2K\sin^2\left(\frac{f\pi}{2}\right)\sin\left(\omega_e t + \phi\right)\sin\left(\omega_e t\right) \tag{4.57}$$

$$F_z = -2K\sin^2\left(\frac{f\pi}{2}\right)\sin\left(\omega_e t + \phi\right)\cos\left(\omega_e t\right) \tag{4.58}$$

Figs.(4.9)-(4.11) show these various quantities for the following three cases, with K, and $\widehat{B}$ set to unity.

Case 1: Full pitch winding, current on q-axis

The field at each side of the coil is in anti-phase, and field maximums at each side coincide with the current maximum, with the current in phase with the airgap voltage. This means that the generator action and the radial forces are in phase on the left and right, and are maximums. The generator action is pulsing in a sine-squared form with maximums when the coil centre is midway between poles. The radial forces are sinusoidal in form and cancel to zero over one cycle, thus for the entire machine there is no nett radial force. Because both the generator forces and the radial forces are in phase on both sides there are no twisting torques on the coil.

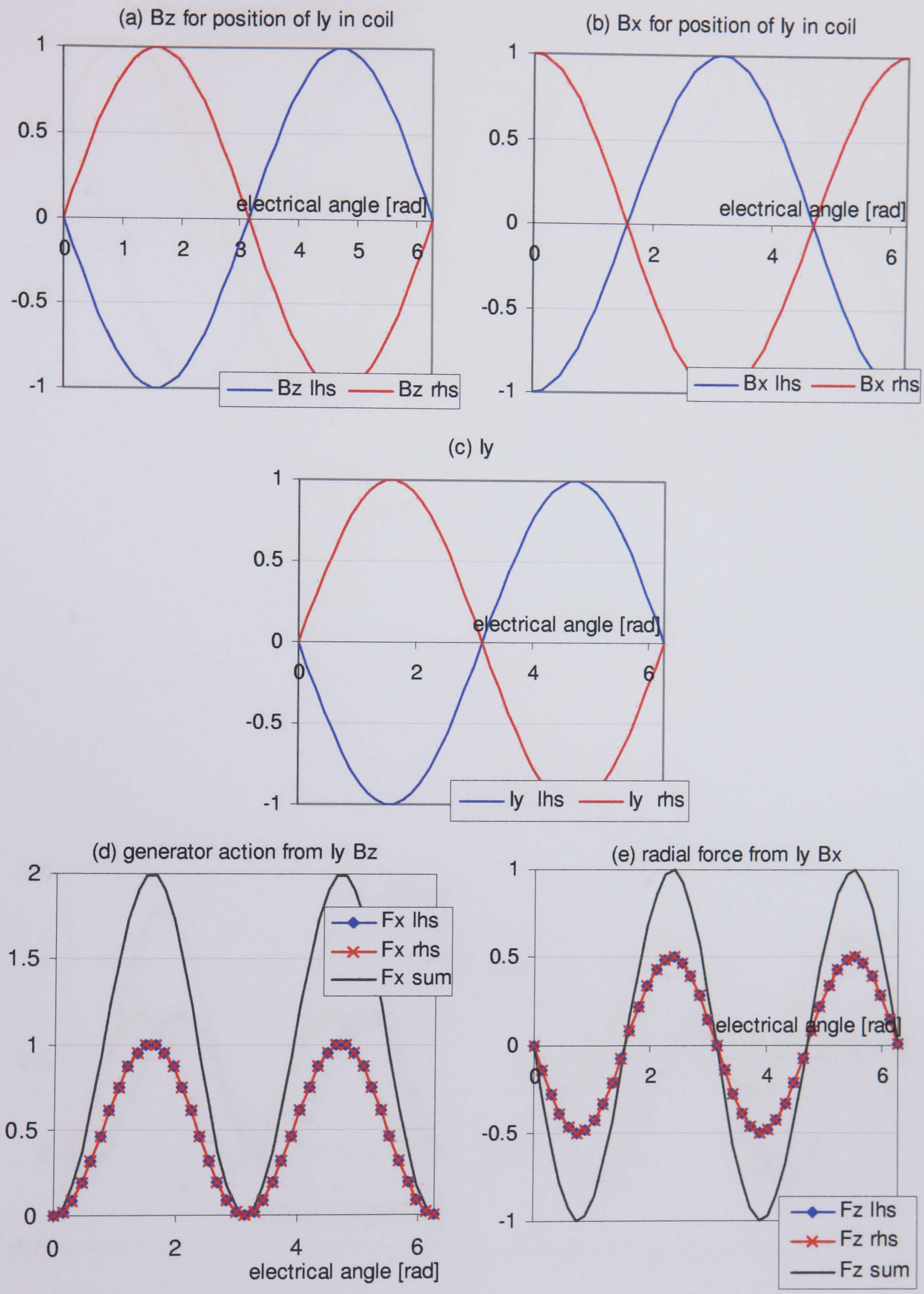

Figure 4.9: 2D Field-current forces for a full pitch coil at upf

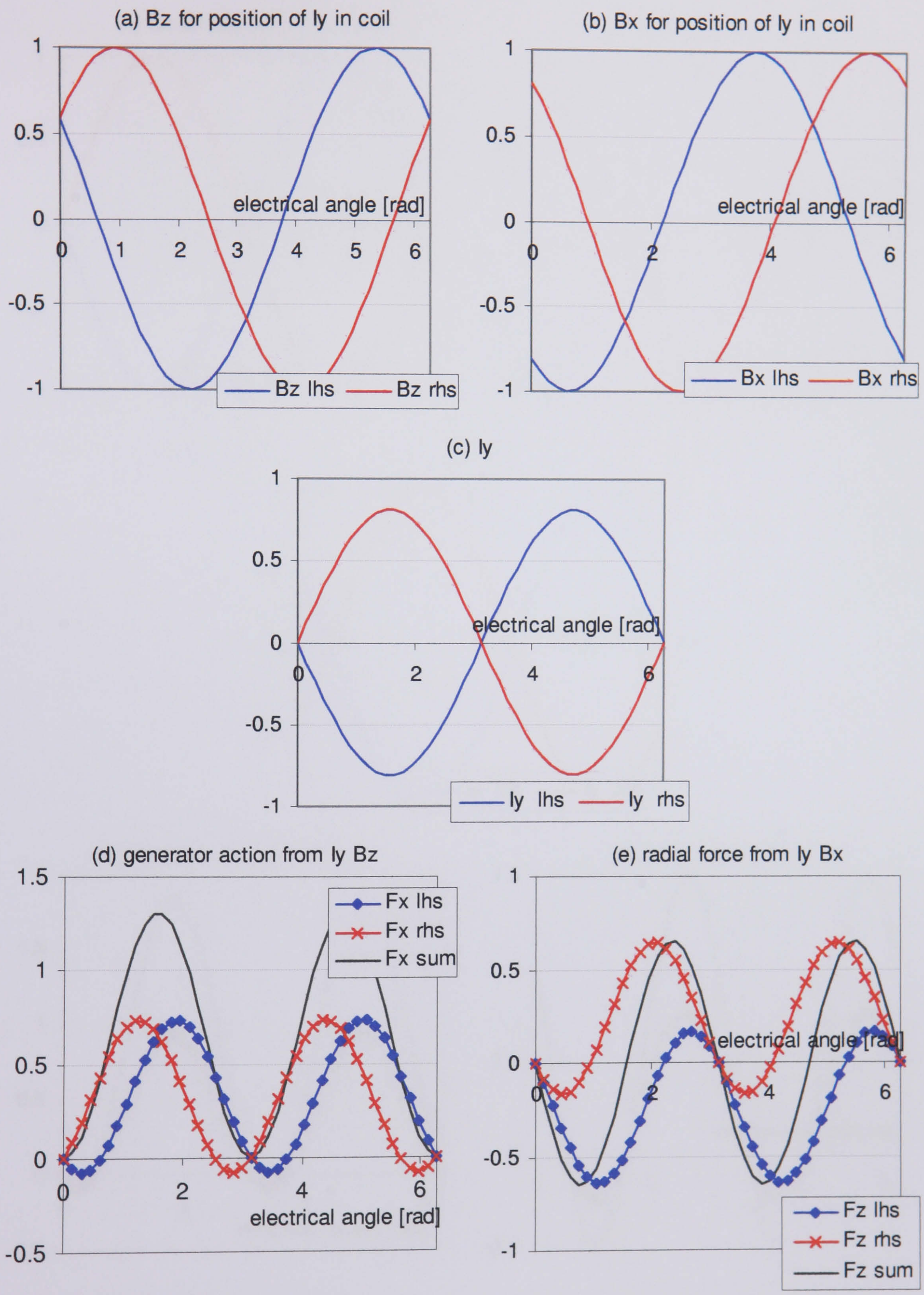

Figure 4.10: 2D Field-current forces for a fractional pitch coil at upf

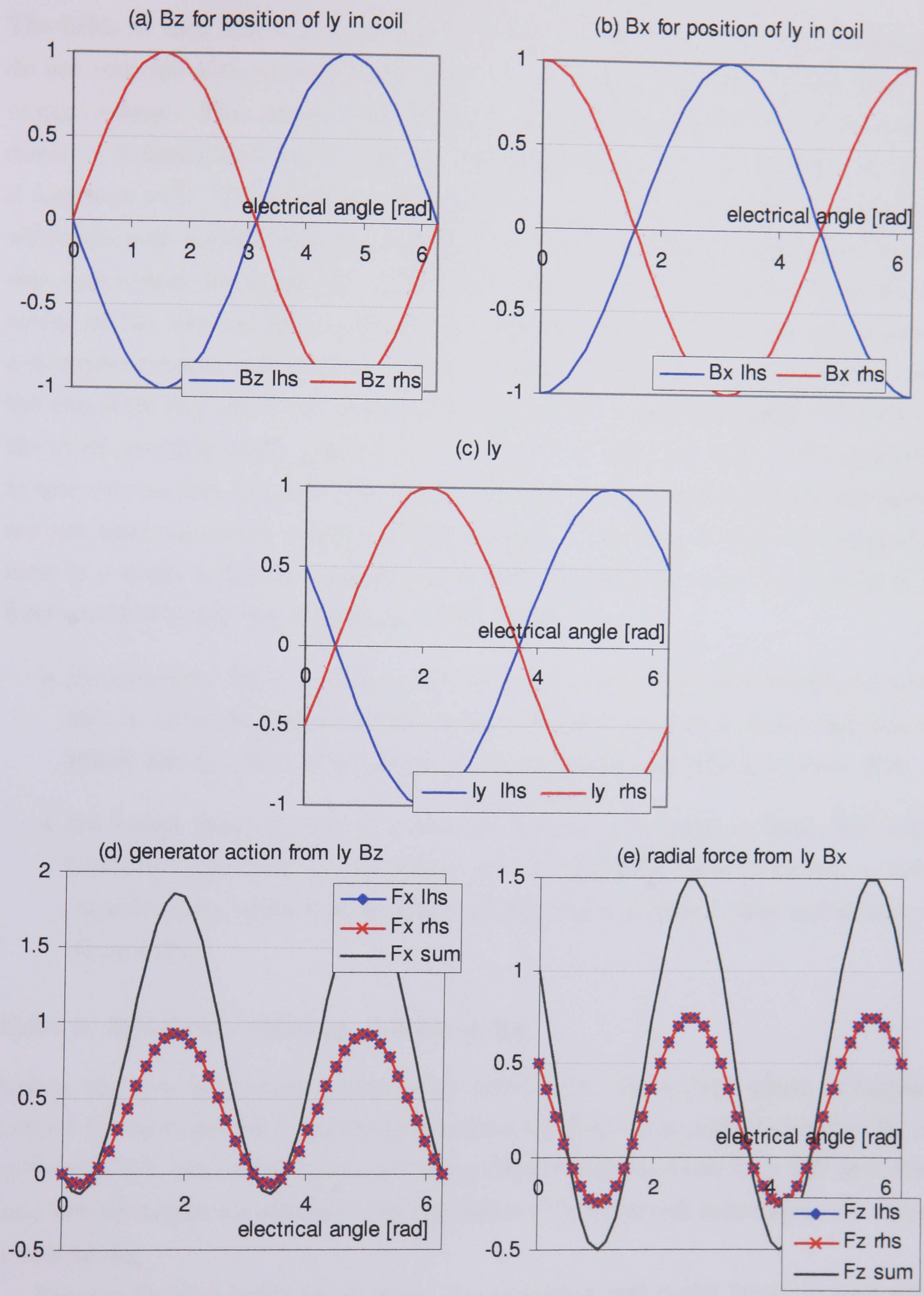

Figure 4.11: 2D Field-current forces for a fractional pitch coil with inductive lag

Case 2: Fractional pitch winding (f=0.6), current on q-axis

The fields at each side of the coil are now not π out of phase and field maximums do not coincide with current maximums, but the current is still in phase with the airgap voltage. This means that both the generator and radial forces are scaled down by a factor $\sin^2(f\pi/2)$, once for the induced current and once for the field it interacts with. The generator action on the two sides moves out of phase and. whilst the sum is still a sine-squared form and so always positive, individually each side experiences forces in the -x direction. The differences between these forces acting on the left and right sides at any moment in time will give rise to a varying x-direction tension/compression within the body of the coil. The radial forces on the two sides also move out of phase and one becomes predominantly positive and the other predominantly negative i.e. they become offset sinusoids. They still sum to zero over a cycle, but now there are cycles of y-direction torque because the forces are not instantaneously identical. The changes in the form of both the generator force in a single conductor and the radial force on each side, from a full pitch to a fractional pitch coil, can be understood as follows:

- the generator force at f=1 is sine-squared in form, but with fractional pitch this is (a) scaled and (b) a further term is added, a product of sine and cosine, which has the effect of adjusting the scale further and adding a phase shift.

- the radial force at f=1 is a product of sine and cosine in form, but with fractional pitch this is (a) scaled and (b) a further term is added, a sine-squared term, which has the effect of adjusting the scale further and adding a phase shift.

Case 3: Full pitch winding, inductive lag

Unless the generator feeds a controlled active load, the current phase is lagging behind the emf because in practical situation the load is normally inductive. If. as in Section 6.5, the coil is connected via a diode bridge rectifier to a DC link, the load acts quite like a resistance, but non-linear. Thus the coil inductance will cause a current lag.

Because the coil is full pitch again, the generator and radial forces in each side of the coil are in phase. With Case 2, the phase shift occurring from the fractional pitch was equal and opposite for the two sides of the coil, and hence they cancelled out, but here the phase shift is applied to both sides, making the mathematical

arguments that applied to each coil side in Case 2 apply to the sum of the forces here. This leads to periods in the cycle where the generator action is negative. and a net radial force over the cycle. This radial force is pushing the coil away from the rotor with a phase lag, but if it were a phase lead it would be an airgap closing force and would require structural stiffness to counter it.

4.6.2 3D Analysis

Fig.(4.12) shows the layout of the 3D simplified physical model including the assumed fundamental field and the concentrated coil. The simple coil is now rectangular and has ends, and the fundamental field is now 3D i.e. $\mathbf{I} = I_y\hat{\mathbf{y}} + I_x\hat{\mathbf{x}}$, $\mathbf{B} = B_x\hat{\mathbf{x}} + B_y\hat{\mathbf{y}} + B_z\hat{\mathbf{z}}$ and Eq.(4.41) becomes:

$$d\mathbf{F} = F_x + F_y + F_z = I_yB_z\hat{\mathbf{x}} - I_xB_z\hat{\mathbf{y}} + (I_xB_y - I_yB_x)\hat{\mathbf{z}} \tag{4.59}$$

In the 2D analysis B_z and B_x were a function of x alone, now these are a function of x and y. This means that the left and right sides of the coil are subjected to a B_z and B_x that varies along their length, when in the 2D analysis it was constant. However, this amounts to $\widehat{B}$ being replaced with an average over the coil length, $\bar{B}$, resulting in the right hand side of Eqns.(4.57)-(4.58) being multiplied by $\overline{B}^2/\widehat{B}^2$.

There is now a B_y component which interacts with the I_x in the end windings. This B_y also varies in the y and x-direction. For the positive-y end winding the fundamental B_y can be written:

$$B_y(\text{+ve y}) = \widehat{B}'_y \cos\theta_e \tag{4.60}$$

and for negative-y

$$B_y(\text{-ve y}) = -\widehat{B}'_y \cos\theta_e \tag{4.61}$$

where $\widehat{B}'_y$ is the maximum at the particular $\pm y$-position, which depends on the coil and magnet length in the y-direction. However, what is required is the -I_xB_z & I_xB_y over the end winding length ie from $\theta_e{=}{-}f\pi/2 - \omega_e t$ to $\theta_e{=}f\pi/2 - \omega_e t$, or use the average of these fields over the length:

$$\overline{B}'_y(\text{+ve y}) = \frac{\widehat{B}'_y}{f\pi}\int_{\theta_e=-\frac{f\pi}{2}-\omega_e t}^{\theta_e=\frac{f\pi}{2}-\omega_e t} \cos\theta_e d\theta_e \tag{4.62}$$

i.e.

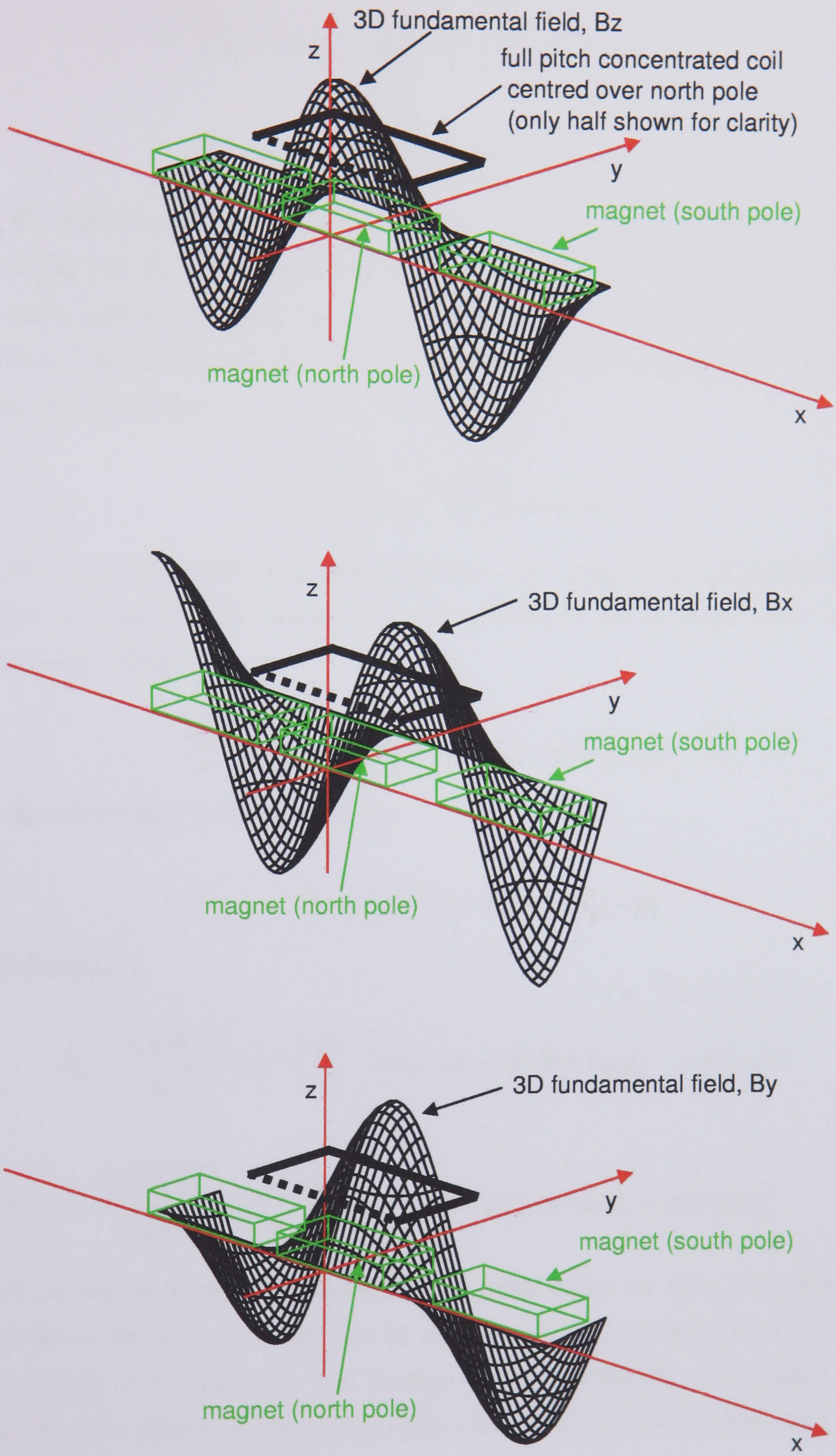

Figure 4.12: Layout of 3D machine

$$\overline{B}'_y(\text{+ve y}) = \frac{2\widehat{B}'_y}{f\pi}\sin\left(\frac{f\pi}{2}\right)\cos(\omega_e t) \tag{4.63}$$

$$\overline{B}'_y(\text{-ve y}) = -\frac{2\widehat{B}'_y}{f\pi}\sin\left(\frac{f\pi}{2}\right)\cos(\omega_e t) \tag{4.64}$$

The B_z component also interacts with the I_x in the end windings. At the coil ends, just like the B_y component had a maximum of $\widehat{B}'_y$, B_z has, $\widehat{B}'_z$. $\widehat{B}'_y$ & $\widehat{B}'_z$ are not the same generally as B_y has a sine form in the y-direction, whilst B_z has a cosine form. The average of the B_z field along the end winding is, for both positive and negative y position:

$$\overline{B}'_z = \frac{2\widehat{B}'_z}{f\pi}\sin\left(\frac{f\pi}{2}\right)\cos(\omega_e t) \tag{4.65}$$

Current I_x in the positive-y end winding is the same sense as in the left hand side of the coil and for the negative-y end winding it is the same sense as in the right hand side. Therefore:

$$F_y = -I_x(\text{+y})\widehat{B}'_z(\text{+y}) - I_x(\text{−y})\widehat{B}'_z(\text{−y}) \tag{4.66}$$

and the additional z-direction force:

$$F_{z2} = I_x(\text{+y})\widehat{B}'_y(\text{+y}) + I_x(\text{−y})\widehat{B}'_y(\text{−y}) \tag{4.67}$$

Substituting in:

$$F_y = \frac{2K\overline{B}\,\overline{B}'_z}{f\pi\widehat{B}^2}\sin^2\left(\frac{f\pi}{2}\right)\sin(\omega_e t + \phi)\left[\cos(\omega_e t) - \cos(\omega_e t)\right] \tag{4.68}$$

$$F_{z2} = -\frac{2K\overline{B}\,\overline{B}'_y}{f\pi\widehat{B}^2}\sin^2\left(\frac{f\pi}{2}\right)\sin(\omega_e t + \phi)\left[\cos(\omega_e t) + \cos(\omega_e t)\right] \tag{4.69}$$

Fig.(4.13) shows these two forces for the same cases as were presented in 2D. The axial force for each coil end are in anti-phase, sum to zero at all times, and result in a cycle of compression and tension in the coil axially. The radial force for each coil end is in phase, so the coil is subjected to a cycle of positive and negative force, which sums to zero over a cycle.

Inductive phase lag makes the axial forces more compressive and less tensile, and the radial forces to be more positive and less negative. With capacitative phase lead the opposite is true, giving more tensile and less compressive axial forces, and

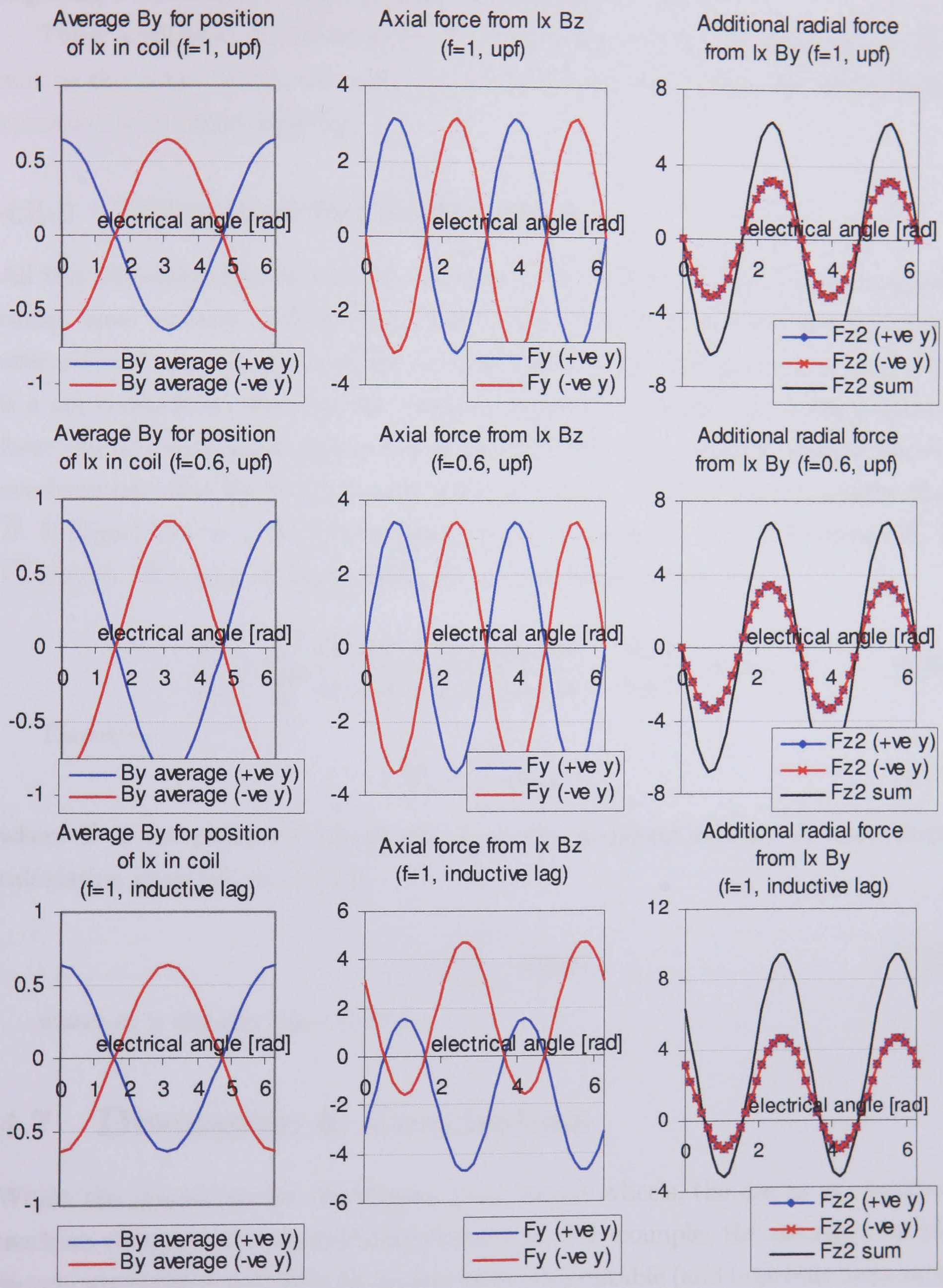

Figure 4.13: 3D Field-current forces

less positive and more negative radial forces, thus, just like the 2D radial forces, requiring a structural stiffness to resist this airgap closing force.

These additional radial forces act in phase with the original ones, and so they add to the range of the force during the cycle and also to any net force during operation with phase lead/lag.

4.6.3 Estimate of Net Radial Force

All this discussion has focussed on the nature of the forces. To assess their significance, some estimate of their magnitudes is required. It is assumed that variations over a electrical cycle can be ignored at this stage, but during phase lag or lead there is a net radial force. Because the torque is known for a design, the total generator force can be found, knowing the radius. 3D field effects are ignored because the coil overhang positions the coil end away from the field ie $\overline{B}'_z$, $\overline{B}'_y$ are much smaller than $\overline{B}$. If Eqns.(4.57) & (4.58) are integrated over an electrical cycle the average $\overline{F}_x$ & $\overline{F}_z$ results. The ratio of these allows $\overline{F}_z$ to be estimated from $\overline{F}_x$:

$$\frac{\overline{F}_z}{\overline{F}_x} = \frac{\int_0^{2\pi} \sin(\omega_e t + \phi)\cos(\omega_e t)dt}{\int_0^{2\pi} \sin(\omega_e t + \phi)\sin(\omega_e t)dt} = \frac{\sin\phi}{\cos\phi} = \tan\phi \tag{4.70}$$

Therefore

$$\overline{F}_z = \frac{T}{r_r}\tan\phi \tag{4.71}$$

where T is the generator torque and r_r is the generator radius. A hoop stress calculation gives the rim stress:

$$\sigma_r = \frac{T}{r_r \pi a_r}\tan\phi \tag{4.72}$$

where a_r is the rim cross section.

4.7 Discussion & Conclusions

Whilst the inspiration for SLiM came from bicycle wheels, the use as an electrical machine structure is a considerable departure. For example, the tolerance on the bicycle wheel rim is probably far greater than is acceptable (and hopefully achievable at reasonable cost) in an electrical machine. Also, the force regime in a bicycle wheel is completely different, and perhaps more demanding, with the need for the wheel to withstand large point forces on the rim.

The SLiM configuration chosen from a large set of possibilities is not necessarily most suitable, but at this stage is a best guess starting point, and much of the development is relevant to other designs. If the spoking was not paired at the rim ie pulling and pushing spokes arrived individually, the force acting on the rim, and hence it's deflections, would change depending on the torque. This would demand a model that combined rim stiffness and spoke stiffness to give rim deflections and required spoke cross section. The choice of paired spoking brings design advantages but also separates the spoke sizing and the rim deflection calculations.

After comparison of the three torque models i.e. the spoke sizing models, it can be seen that the simplest one is adequate for steel spokes, or any spoke with similar modulus of elasticity. Because the rim remains under the same spoke forces during operation, a standard calculation can be used to find rim deflection, without incorporating spoke stiffness.

Buckling of the stator and rotor structure is a complex issue but the two calculations developed will show whether the hoop stress in the rims of the case study designs brings the structures close to this example of buckling mode.

A simple model of the effect of storm winds on the structures is presented and allows the estimation of a suitable hub length for the generator. Aerodynamic losses are not considered any further at present.

The nature of the forces between the various field components and the coil current is investigated in some detail, including the effects of phase change in the coil current. The nature of alot of the forces is cyclical with no net force over an electrical cycle, and would therefore only impact coil module design to ensure adequate strength and structural stiffness at a local level. However, during phase lag or lead, net radial forces do exist whose magnitude is estimated simply from the torque in the generator.

Chapter 5

Ironless Stator Electromagnetics

The radial airgap PM rotor proposed for use with SLiM has a magnetic field unconstrained by stator iron, and its magnitude and direction vary drastically in the region to be swept by any stator coils.

The 2D separation of variables solution to Laplace's equation with boundary conditions of infinite, infinitely permeable rotor back and stator iron is often used to calculate the rotor field in the gap of long electrical machines. This can be adapted for use with ironless stator machines by removing the stator iron boundary. This is done initially, but the likely short axial length of SLiM leads to concerns that end fringing effects could significantly affect B_z, the normal component of the magnetic field. Therefore a novel extension to the technique is developed to allow the calculation of the 3D field of rectangular magnets on an infinite infinitely permeable rotor.

Detailed experimental work mapped the normal component of the field over a line of permanent magnets mounted on steel plate, in order to validate the 3D analytical work and investigate the effect of a finite width steel backing, which cannot be modelled with this technique.

5.1 2D Analytical Model of the Magnetic Field

This models the magnetic field due to a line of alternating polarity, rectangular, permanent magnets assuming that the magnets are of sufficient axial length that end effects can be ignored. Because the machines being considered are invariably of a high pole number, curvature can be ignored, so a right handed cartesian coordinate system is used where x refers to the circumferential direction, y the axial direction, and z the radial direction. The magnet, which typically has a relative

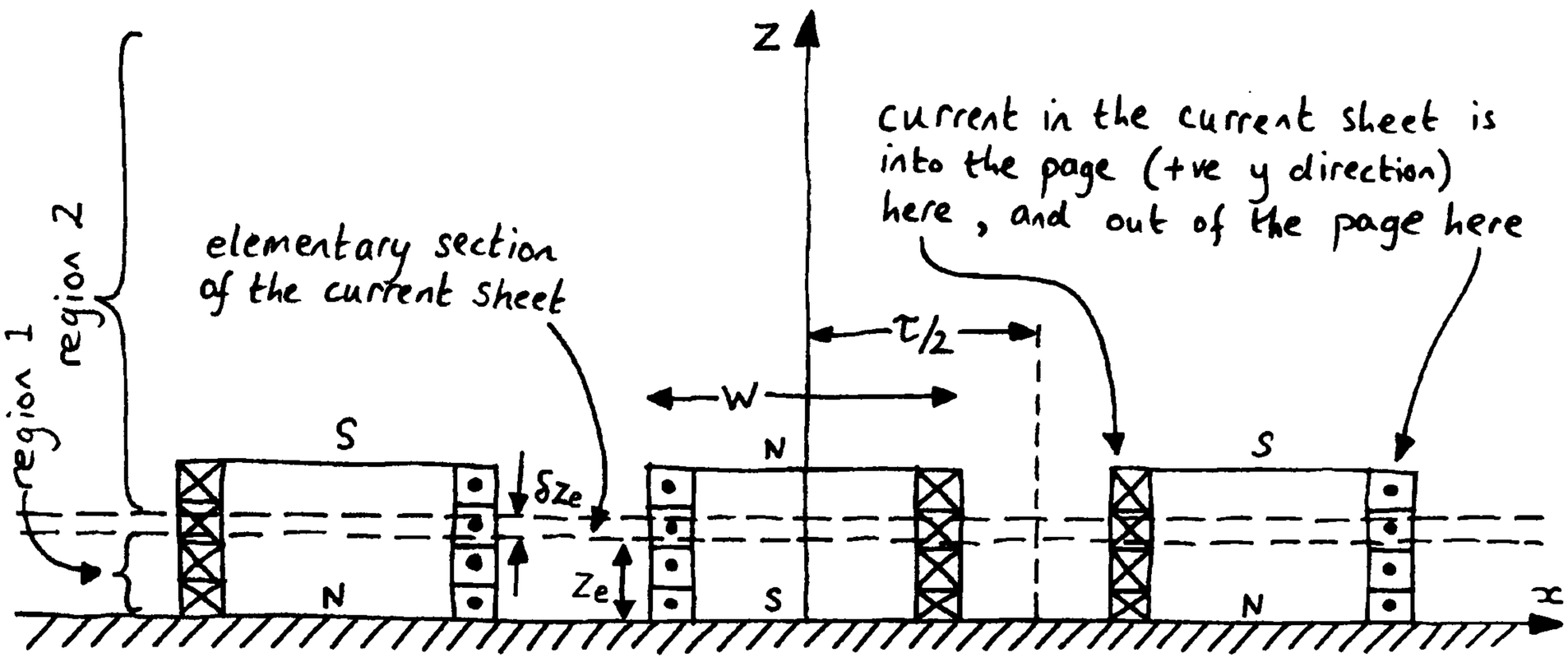

Figure 5.1: Details of 2D Rotor Representation

permeability of 1.05, is approximated by a region with a relative permeability of 1 and it's magnetization is represented by a current sheet, Fig.(5.1). At the edges of the magnets the current sheet has a positive or negative value, elsewhere the current in the current sheet is zero. The y-direction linear current density with respect to the z-axis is:

$$K_m = B_{rem}/\mu_0 \tag{5.1}$$

Fig.(5.2) shows an elementary section of this current sheet of thickness δz_e. These current elements at the edges of the magnets are periodic impulses with respect to the x-direction, Fig.(5.2), that can be represented by a Fourier series.

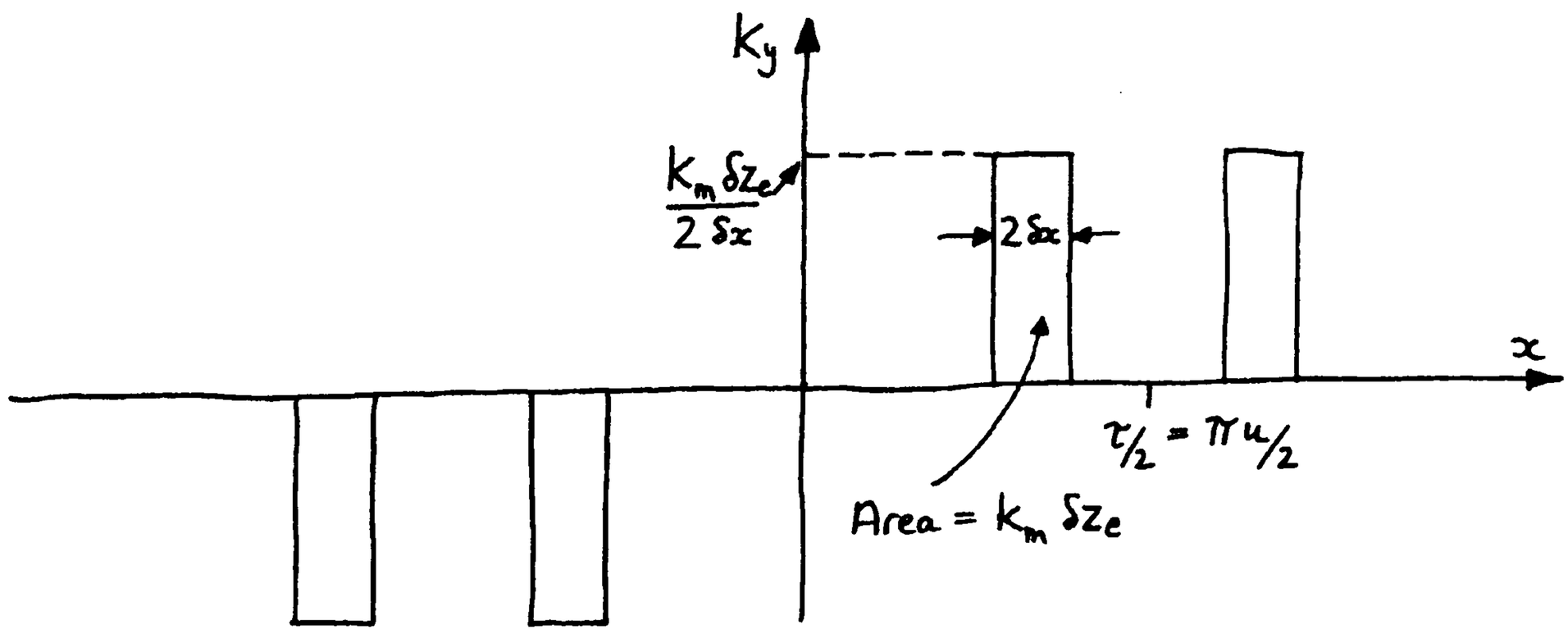

Figure 5.2: Magnets as Current Impulses

The area of each impulse is $K_m \delta z_e$. If $2\delta x$ is chosen as the width, the height is $K_m \delta z_e / 2\delta x$. Decomposing the set of impulses into a Fourier series:

$$K_y = \sum_n K_n \delta z_e \sin(nx/u) \tag{5.2}$$

where

$$u = \frac{\tau}{\pi} \tag{5.3}$$

and

$$K_n = \frac{4K_m}{\pi u} \sin(nw/2u) \qquad \text{odd n only} \tag{5.4}$$

The flux density created by each of these Fourier components of the elementary current sheet can be found analytically for any point above the rotor back iron. The expressions can then be integrated over the thickness of the magnet to find the flux density generated by each Fourier component. The field can then be summed for a sufficient number of Fourier terms to find the total field at any point. The z-component of this field can be used to find the flux linkage of the stator coils.

The first step is to find the magnetic field generated by a Fourier component of an elementary current sheet. Since the regions below (Region 1) and above (Region 2) the elementary current sheet are free space, $\underline{\nabla} \times \underline{H} = 0$, and also $\underline{B} = \underline{\nabla} \times \underline{A}$, which leads to Laplace's equation,

$$\underline{\nabla}^2 \cdot \underline{A} = 0 \tag{5.5}$$

and

$$B_x = \frac{\partial A_z}{\partial y} - \frac{\partial A_y}{\partial z} \tag{5.6}$$

$$B_y = \frac{\partial A_x}{\partial z} - \frac{\partial A_z}{\partial x} \tag{5.7}$$

$$B_z = \frac{\partial A_y}{\partial x} - \frac{\partial A_x}{\partial y} \tag{5.8}$$

With current in only the y-direction, the B field must be in the xy plane, so $B_y = 0$, and from eq.(5.7) $A_x = A_z =$ constant and therefore both can be set to zero, and eqs.(5.5),(5.6) and (5.8) simplify to:

$$\nabla^2 \cdot A_y = 0 \tag{5.9}$$

$$B_x = -\frac{\partial A_y}{\partial z} \tag{5.10}$$

$$B_z = \frac{\partial A_y}{\partial x} \tag{5.11}$$

Also A_y is not a function of y so eq. (5.9) has a separation of variables solution of the form:

$$A_y = X(x)\,Z(z) \tag{5.12}$$

and knowing it is periodic in the x direction:

$$A_y = (C\sin kx + D\cos kx)\left(Ee^{kz} + Fe^{-kz}\right) \tag{5.13}$$

where $C, D, E.F$ are constants to be found from the boundary conditions. The magnetic flux density can now be found from eqs.(5.10) and (5.11):

$$B_x = -k\,(C\sin kx + D\cos kx)\left(Ee^{kz} - Fe^{-kz}\right) \tag{5.14}$$

$$B_z = k\,(C\cos kx - D\sin kx)\left(Ee^{kz} + Fe^{-kz}\right) \tag{5.15}$$

Applying boundary conditions, with subscripts 1 and 2 showing the region referred to:

(i). Region 2 extends to infinity in the z-direction, where $B_x = 0$, therefore $E_2 = 0$

(ii). In Region 1 at the steel backing surface ($z = 0$), $B_x = 0$ due to the high permeability of the steel, therefore $E_1 = F_1$

(iii). At the boundary between Region 1 and Region 2, ie either side of the elementary current sheet, $\underline{\nabla} \times \underline{H} = \underline{J}$

$$H_{x_2} - H_{x_1} = K_n \delta z_e \sin nx/u \tag{5.16}$$

Substituting from eqns.(5.14) & (5.15) into the left hand side of eq.(5.16) and applying $E_2 = 0$ & $E_1 = F_1$ from (i) & (ii) above:

$$\frac{k}{\mu_0}(C_2\sin kx + D_2\cos kx)\,F_2 e^{-kz_e} + \frac{k}{\mu_0}(C_1\sin kx + D_1\cos kx)\,F_1\left(e^{kz_e} - e^{-kz_e}\right) = K_n\delta z_e \sin(nx/u) \tag{5.17}$$

The right hand side only has sine terms in x, therefore $D_1 = D_2 = 0$, and this also defines $k = n/u$. Therefore eq. (5.17) simplifies to:

$$C_2 F_2 e^{-nz_e/u} = \frac{\mu_0 K_n \delta z_e}{n/u} - C_1 F_1 \left(e^{nz_e/u} - e^{-nz_e/u}\right) \tag{5.18}$$

(iv). Also at the boundary between Region 1 and Region 2, H_z is continuous, which leads to:

$$C_2 F_2 e^{-nz_e/u} = C_1 F_1 \left(e^{nz_e/u} + e^{-nz_e/u}\right) \tag{5.19}$$

which can be used with eq.(5.18) to give:

$$C_1 F_1 = \frac{\mu_0 K_n \delta z_e}{2n/u}\, e^{-nz_e/u} \tag{5.20}$$

$$C_2 F_2 = \frac{\mu_0 K_n \delta z_e}{n/u} \cosh kz_e \tag{5.21}$$

All the constants are now defined by these conditions. With $B_1 = B_2 = C_2 = 0$, $C_1 = D_1$ and $k = n/u$, eqs.(5.14), (5.15) can be rewritten:

$$B_{x_1} = -2C_1 F_1 \left(n/u\right) \sin\left(nx/u\right) \sinh\left(nz/u\right) \tag{5.22}$$

$$B_{x_2} = C_2 F_2 \left(n/u\right) \sin\left(nx/u\right) e^{-nz/u} \tag{5.23}$$

$$B_{z_1} = 2C_1 F_1 \left(n/u\right) \cos\left(nx/u\right) \cosh\left(nz/u\right) \tag{5.24}$$

$$B_{z_2} = C_2 F_2 \left(n/u\right) \cos\left(nx/u\right) e^{-nz/u} \tag{5.25}$$

Substituting eqs.(5.20),(5.21) into eqs.(5.22) to (5.25) gives the flux density at any point in Region 1 or Region 2 due to the elementary current sheets:

$$B_{x_1} = -\mu_0 K_n \sin\left(nx/u\right)\, \sinh\left(nz/u\right)\, e^{-nz_e/u}\, \delta z_e \tag{5.26}$$

$$B_{x_2} = \mu_0 K_n \sin\left(nx/u\right)\, e^{-nz/u} \cosh\left(nz_e/u\right)\, \delta z_e \tag{5.27}$$

$$B_{z_1} = \mu_0 K_n \cos(nx/u)\ \cosh(nz/u)\ e^{-kz_e}\ \delta z_e \tag{5.28}$$

$$B_{z_2} = \mu_0 K_n \cos(nx/u)\ e^{-nz/u} \cosh(nz_e/u)\ \delta z_e \tag{5.29}$$

The expressions for Region 2 can now be integrated over all the elementary current sheets at positions $0 \leq z_e \leq t_m$ to give the flux density from that Fourier component from the entire magnet thickness. Region 1 disappears because the integration is all the way to the rotor back iron. The total magnetic flux density at any point above the magnet surface is the sum of these equations over a sufficient number of Fourier terms. After the integration, substitution for K_n from eq.(5.4), and use of eq.(5.1) gives:

$$B_{x_2 total} = \sum_{n\ odd} \frac{4B_{rem}}{n\pi} \sin(nw/2u) \sinh(nt_m/u) \sin(nx/u) e^{-nz/u} \tag{5.30}$$

$$B_{z_2 total} = \sum_{n\ odd} \frac{4B_{rem}}{n\pi} \sin(nw/2u) \sinh(nt_m/u) \cos(nx/u) e^{-nz/u} \tag{5.31}$$

5.2 3D Analytical Model of the Magnetic Field

In the 2D analysis the infinitely long magnets are represented by current sheets which are unmodulated in the y-direction. The 3D analysis models rectangular magnets set out in a rectangular grid on an infinite steel backing, see Fig.(5.3) by making two changes to the 2D representation of the magnetization.

Firstly, the 2D y-directed current sheet is now modulated in the y-direction by multiplying the Fourier series that describes them with respect to the x-direction, similar to eq.(5.2) and Fig.(5.2), by a Fourier series in the y-direction comprising a series of well spaced rectangles, see Fig.(5.4), that sets the current sheet to zero between magnets. The two central rectangles represent the sides of the rotor magnet, but the further repetitions imply an infinite line of magnets in the y-direction which is clearly not what is required. By setting τ_y sufficiently large compared with w_y then these 'ghost' magnets will not influence the magnetic field at the rotor. The complete expression to describe the spatial distribution of y-direction current density is:

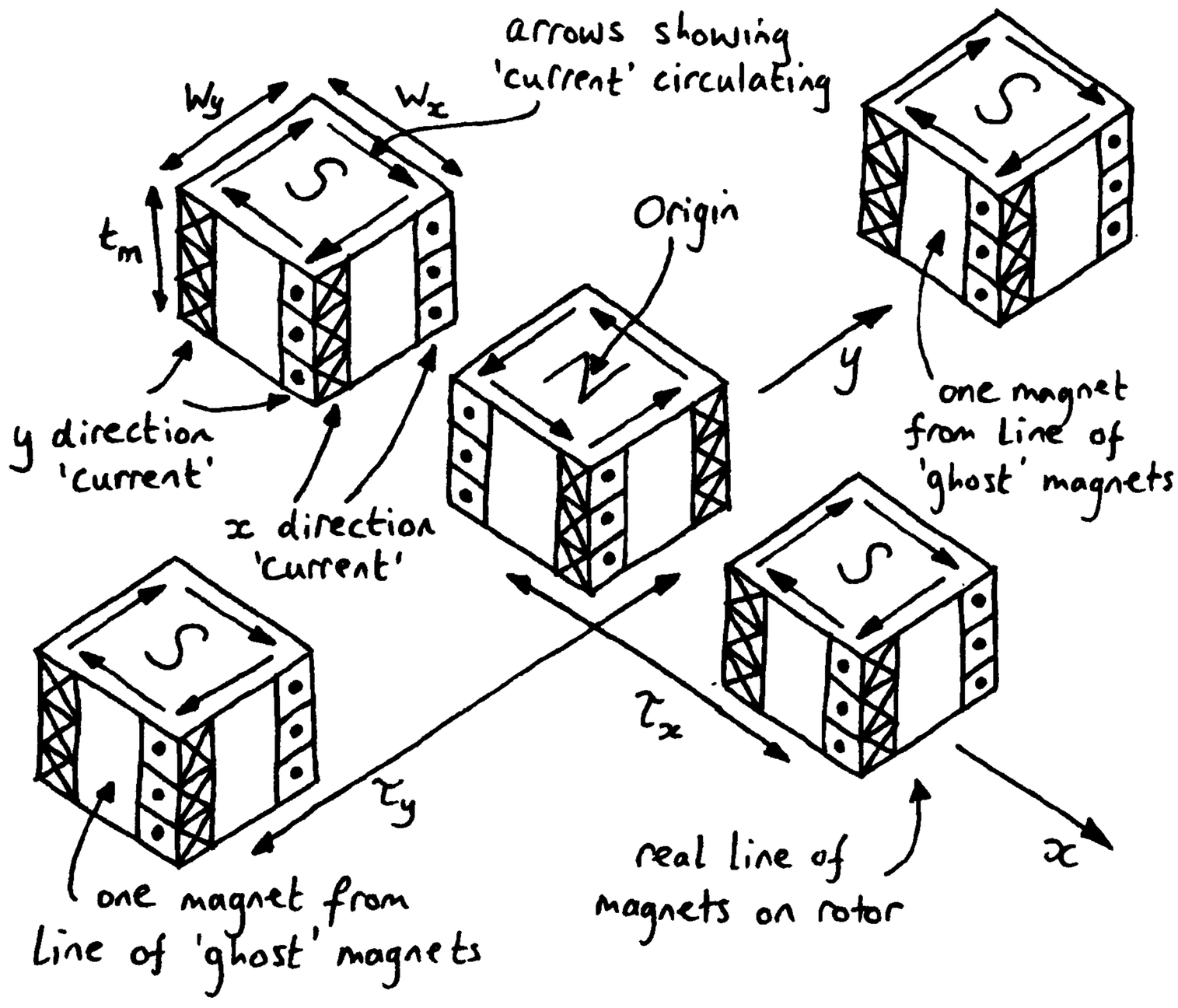

Figure 5.3: Details of 3D Rotor Representation

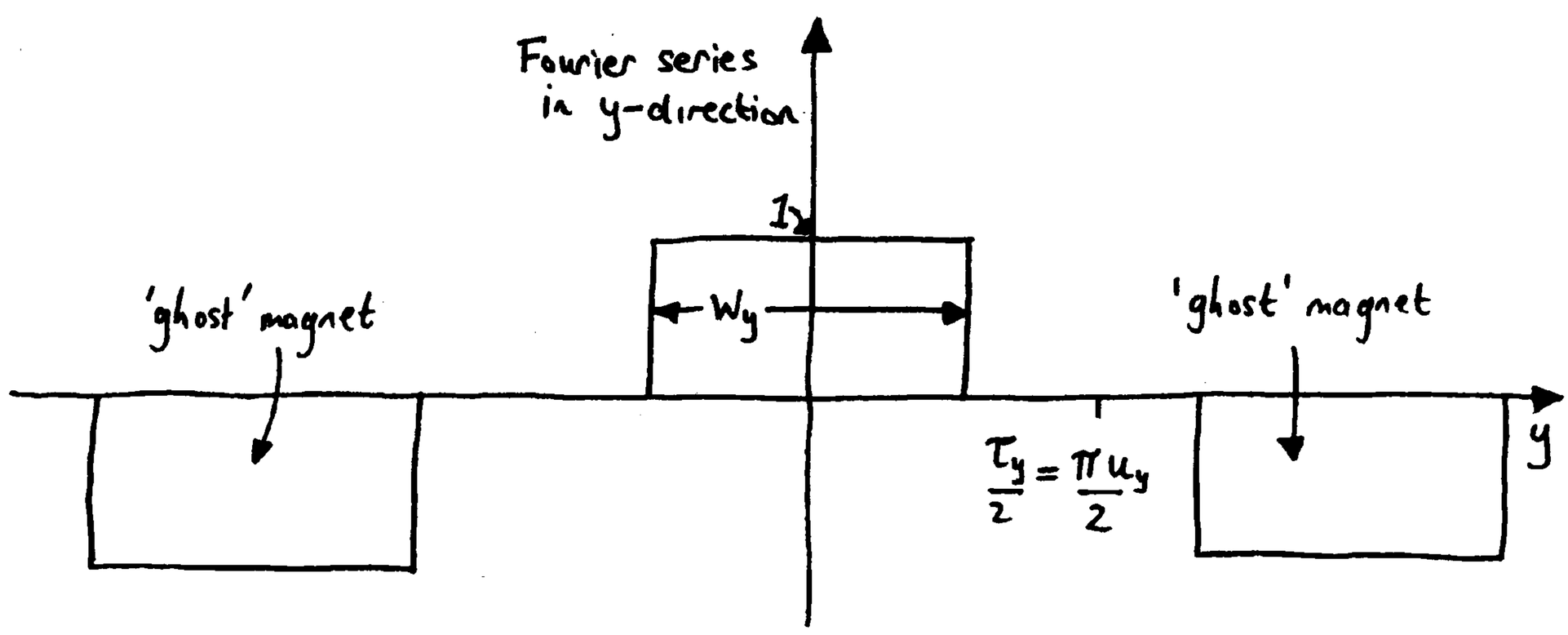

Figure 5.4: y-direction Modulation of K_y

$$K_y = \sum_{n,\ m \text{ odd}} \underbrace{\frac{4K_m}{\pi u_x} \sin\left(nw_x/2u_x\right)\delta z_e \sin\left(nx/u_x\right)}_{\text{Fourier series in x direction}} \underbrace{\frac{4}{m\pi} \sin\left(mw_y/2u_y\right) \cos\left(my/u_y\right)}_{\text{Fourier series in y direction}} \tag{5.32}$$

where

$$u_x = \tau_x/\pi, \qquad u_y = \tau_y/\pi \tag{5.33}$$

Secondly, in addition to the y-direction current down the sides of the magnets, a z-directed current sheet is needed for the ends of the magnets. This has essentially the same spatial distribution as the y-direction current sheet but rotated by 90 degrees:

$$K_x = -\sum_{n,\ m \text{ odd}} \underbrace{\frac{4K_m}{\pi u_y} \sin\left(mw_y/2u_y\right)\delta z_e \sin\left(my/u_y\right)}_{\text{Fourier series in y direction}} \underbrace{\frac{4}{n\pi} \sin\left(nw_x/2u_x\right) \cos\left(nx/u_x\right)}_{\text{Fourier series in x direction}} \tag{5.34}$$

The negative sign is from the orientation of this current sheet with respect to the x-axis, see Fig.(5.3). Extracting some terms common to both K_y and K_x:

$$K_{n,m} = \frac{16K_m}{\pi^2} \sin\left(nw_x/2u_x\right) \sin\left(mw_y/2u_y\right) \qquad \text{odd n,m} \tag{5.35}$$

allows eqns.(5.32),(5.34) to be rewritten:

$$K_y = \sum_{n,\ m \text{ odd}} \frac{K_{n,m}}{mu_x} \delta z_e \sin\left(nx/u_x\right) \cos\left(my/u_y\right) \tag{5.36}$$

$$-K_x = \sum_{n,\ m \text{ odd}} \frac{K_{n,m}}{nu_y} \delta z_e \cos\left(nx/u_x\right) \sin\left(my/u_y\right) \tag{5.37}$$

K_y and K_x create magnetic potentials A_y and A_x respectively, which can be found independently. To find the flux density created by each of the Fourier components of these two elementary current sheets, eqs.(5.5) to (5.8) from the 2D analysis are again simplified, but now only $A_z = 0$, leading to:

$$\nabla^2 \cdot A_x = 0 \qquad \text{for } x \text{ direction current sheet} \tag{5.38}$$

$$\nabla^2 \cdot A_y = 0 \qquad \text{for } y \text{ direction current sheet} \tag{5.39}$$

$$B_x = -\frac{\partial A_y}{\partial z} \tag{5.40}$$

$$B_y = \frac{\partial A_x}{\partial z} \tag{5.41}$$

$$B_z = \frac{\partial A_y}{\partial x} - \frac{\partial A_x}{\partial y} \tag{5.42}$$

For K_y, the potential A_y created by it must be a function of $x.y$ and z, so eq.(5.39) has a separation of variables solution of the form:

$$A_y = X(x)\,Y(y)\,Z(z) = 0 \tag{5.43}$$

Knowing it is periodic in the x and y directions:

$$A_y = (C\sin k_x x + D\cos k_x x)\,(E\sin k_y y + F\cos k_y y)\,\left(Me^{k_z z} + Ne^{-k_z z}\right) = 0 \tag{5.44}$$

and

$$k_x^2 + k_y^2 + k_z^2 = 0 \tag{5.45}$$

where C, D, E, F, M, N are constants to be found from the boundary conditions. The magnetic flux density created by A_y can now be found from eqs.(5.40),(5.42):

$$B_x = -k_z\,(C\sin k_x x + D\cos k_x x)\,(E\sin k_y y + F\cos k_y y)\,\left(Me^{k_z z} - Ne^{-k_z z}\right) \tag{5.46}$$

$$B_z = k_x\,(C\cos k_x x - D\sin k_x x)\,(E\sin k_y y + F\cos k_y y)\,\left(Me^{k_z z} + Ne^{-k_z z}\right) \tag{5.47}$$

Applying boundary conditions, with subscripts 1 and 2 showing the region referred to:

(i). Region 2 extends to infinity in the z-direction, where $B_x = 0$, therefore $M_2 = 0$

(ii). In Region 1 at the steel backing surface ($z = 0$), $B_x = 0$ due to the high permeability of the steel, therefore $M_1 = N_1$

(iii). At the boundary between Region 1 and Region 2, ie either side of the elementary current sheet,

$$H_{x_2} - H_{x_1} = \frac{(B_{x_2} - B_{x_1})}{\mu_0} = \frac{K_{n,m}\delta z_e}{mu_x} \sin(nx/u_x)\cos(ny/u_y) \tag{5.48}$$

K_y only has sine terms in x, and only cosine terms in y, therefore $D_1 = D_2 = E_1 = E_2 = 0$. This also defines $k_x = n/u_x$ and $k_y = m/u_y$ but using k notation throughout gives

$$C_2F_2N_2e^{-k_z z_e} = \frac{\mu_0 K_{n,\,m}\delta z_e}{k_z m u_x} - C_1F_1N_1\left(e^{k_z z_e} - e^{-k_z z_e}\right) \tag{5.49}$$

(iv). Also at the boundary between Region 1 and Region 2, H_z is continuous, which leads to:

$$C_2F_2N_2e^{-k_z z_e} = C_1F_1N_1\left(e^{k_z z_e} + e^{-k_z z_e}\right) \tag{5.50}$$

which can be used with eq.(5.49) to give

$$C_1F_1N_1 = \frac{\mu_0 K_{n,m}\delta z_e}{2k_z m u_x}\, e^{-k_z z_e} \tag{5.51}$$

$$C_2F_2N_2 = \frac{\mu_0 K_{n,m}\delta z_e}{k_z m u_x}\, \cosh k_z z_e \tag{5.52}$$

All the constants are now defined by these conditions. With $D_1 = D_2 = E_1 = E_2 = M_2 = 0$ and $M_1 = N_1$, eqs.(5.46), (5.47) can now be rewritten:

$$B_{x_1} = -2C_1F_1N_1k_z \sin k_x x \cos k_y y \sinh k_z z \tag{5.53}$$

$$B_{z_1} = 2C_1F_1N_1k_x \cos k_x x \cos k_y y \cosh k_z z \tag{5.54}$$

$$B_{x_2} = C_2F_2N_2k_z \sin k_x x \cos k_y y\, e^{-k_z z} \tag{5.55}$$

$$B_{z_2} = C_2F_2N_2k_x \cos k_x x \cos k_y y\, e^{-k_z z} \tag{5.56}$$

These give the flux density at any point in Region 1 or Region 2 due to the elementary y-direction current sheets. A similar procedure can be used for the flux

density due to the x-direction current sheets, but instead finding a solution for A_x (not A_y), getting expressions for B_y and B_z (not B_x and B_z).

The combined results for the two current sheets are:

$$B_{x_1} = -\frac{\mu_0 K_{n,m}}{m u_x} \sin k_x x \ \cos k_y y \ \sinh k_z z \ e^{-k_z z_e} \delta z_e \tag{5.57}$$

$$B_{y_1} = -\frac{\mu_0 K_{n,m}}{n u_y} \cos k_x x \ \sin k_y y \ \sinh k_z z \ e^{-k_z z_e} \delta z_e \tag{5.58}$$

$$B_{z_1} = \left(\frac{k_x}{m u_x} + \frac{k_y}{n u_y}\right) \frac{\mu_0 K_{n,m}}{k_z} \cos k_x x \ \cos k_y y \ \cosh k_z z \ e^{-k_z z_e} \delta z_e \tag{5.59}$$

$$B_{x_2} = \frac{\mu_0 K_{n,m}}{m u_x} \sin k_x x \ \cos k_y y \ e^{-k_z z} \cosh k_z z_e \ \delta z_e \tag{5.60}$$

$$B_{y_2} = \frac{\mu_0 K_{n,m}}{n u_y} \cos k_x x \ \sin k_y y \ e^{-k_z z} \cosh k_z z_e \ \delta z_e \tag{5.61}$$

$$B_{z_2} = \left(\frac{k_x}{m u_x} + \frac{k_y}{n u_y}\right) \frac{\mu_0 K_{n,m}}{k_z} \cos k_x x \ \cos k_y y \ e^{-k_z z} \cosh k_z z_e \ \delta z_e \tag{5.62}$$

where eqns. (5.58), (5.61) are from the x-direction current sheet, eqns. (5.58), (5.61) include the contributions from both current sheets, and eqns. (5.51), (5.52) have been used to substitute for $C_1 F_1 N_1$ and $C_2 F_2 N_2$.

The expressions for Region 2 can now be integrated over all the elementary current sheets at positions $0 \leq z_e \leq t_m$ to give the flux density from that Fourier component from the entire magnet thickness. Region 1 disappears because the integration is all the way to the rotor back iron.

The total magnetic flux density at any point above the magnet surface is the sum of these equations over a sufficient number of Fourier terms. After the integration, substitution for $K_{n,m}$ from eq.(5.35), and using $k_x = n/u_x$, $k_y = m/u_y$ gives:

$$B_{x_2 total} = \sum_{n,m \ odd} \frac{16 B_{rem}}{k_z u_x m \pi^2} \sin\left(\frac{n w_x}{2 u_x}\right) \sin\left(\frac{m w_y}{2 u_y}\right) \sinh k_z t_m \sin\left(\frac{n x}{u_x}\right) \cos\left(\frac{m y}{u_y}\right) e^{-k_z z} \tag{5.63}$$

$$B_{y_2 total} = \sum_{n,m \ odd} \frac{16 B_{rem}}{k_z u_y n \pi^2} \sin\left(\frac{n w_x}{2 u_x}\right) \sin\left(\frac{m w_y}{2 u_y}\right) \sinh k_z t_m \cos\left(\frac{n x}{u_x}\right) \sin\left(\frac{m y}{u_y}\right) e^{-k_z z} \tag{5.64}$$

$$B_{z2total} = \sum_{n,m\ odd} \frac{16B_{rem}}{nm\pi^2} \sin\left(\frac{nw_x}{2u_x}\right) \sin\left(\frac{mw_y}{2u_y}\right) \sinh k_z t_m \cos\left(\frac{nx}{u_x}\right) \cos\left(\frac{my}{u_y}\right) e^{-k_z z} \tag{5.65}$$

where

$$k_z = \sqrt{\frac{n^2}{u_x^2} + \frac{m^2}{u_y^2}} \tag{5.66}$$

5.3 Convergence of Models

In order to use these models, some understanding of how the solution converges is required. The convergence could be effected by position above the magnet surface, magnet shape, magnet pitch, and 'ghost' magnet pitch. Machine design depends on this field calculation, and too many terms will give unnecessarily long calculation times, whilst too few terms will introduce errors.

The issue is trivial for the 2D field compared to the 3D. Fig.(5.5) shows the effects of airgap, magnet pitch and magnet thickness. Convergence is assured by using 30 terms.

For 3D, Figs.(5.6)(a),(b) & (5.7)(a),(b),(c),(d) show how the field calculation converges as the number of fourier terms is increased, for different 'ghost' pitches, heights g, magnet thickness' t_m and magnet pitch τ_x. Magnets are fixed at 50mm (x) and 48mm (y). For each chart, there are 9 x,y locations chosen in a plane above the magnet top surface. The choice of these x and y positions for these example calculations includes areas that are closest to the magnet edges as, from trial and error, these regions seem to have the slowest convergence rates. It can be seen that, generally, the convergence rates and type of convergence varies. Same colour indicates points with the same y-position. This helps to show that x position does not seem to effect the details of convergence, but that within each chart points with the same y position have similar patterns and rates of convergence. Comparisons between charts indicate that the patterns of convergence are not altered by 'ghost' magnet pitch, magnet thickness t_m, magnet pitch τ_x, but are by height g. The reasons for these similar patterns is investigated no further here. However, the fact that there are many different ways in which the solution converges makes it difficult to include a test for convergence at each point during calculation. This would have minimised the calculation time. Instead, by looking at how the rate of convergence is

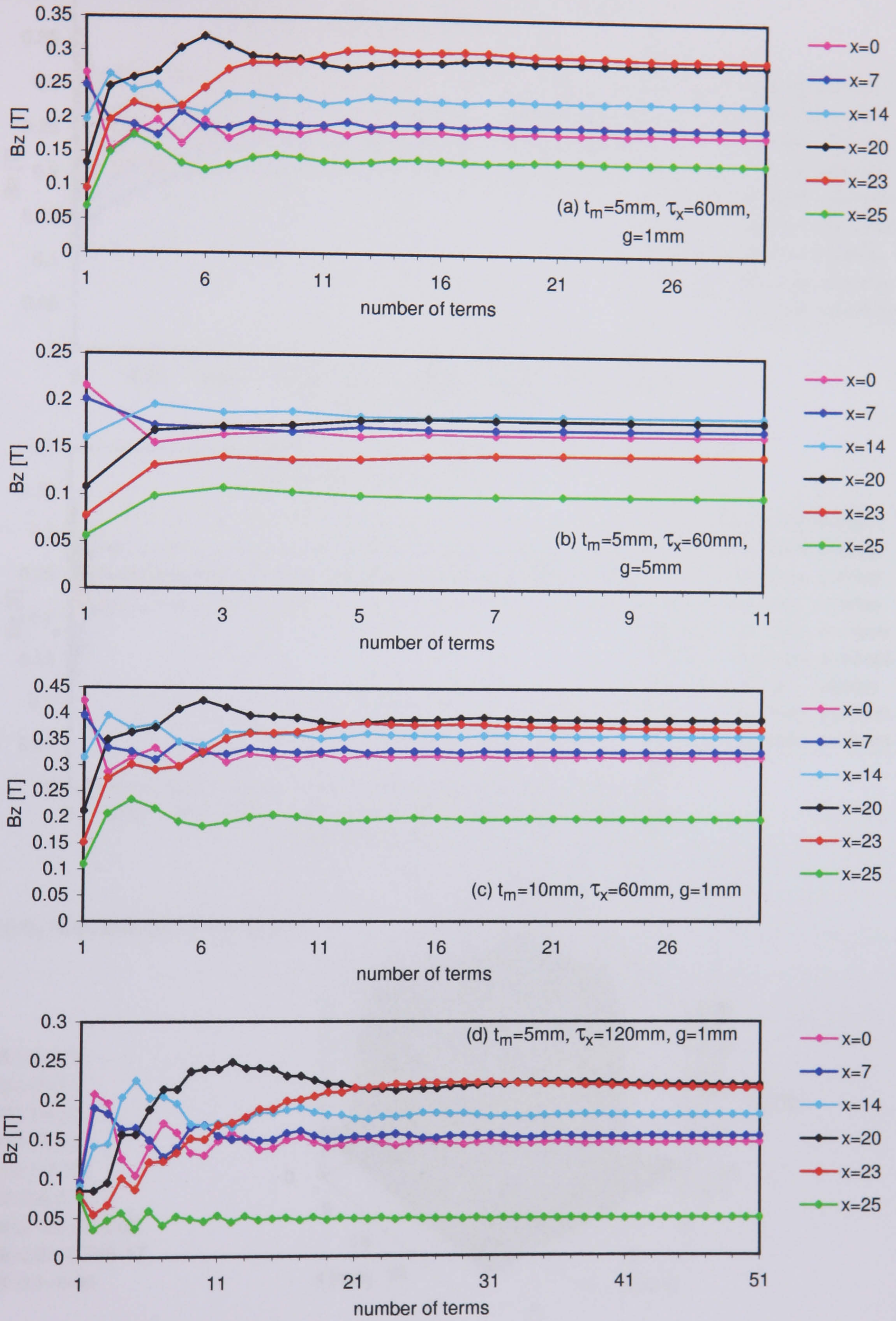

Figure 5.5: Factors affecting 2D model convergence

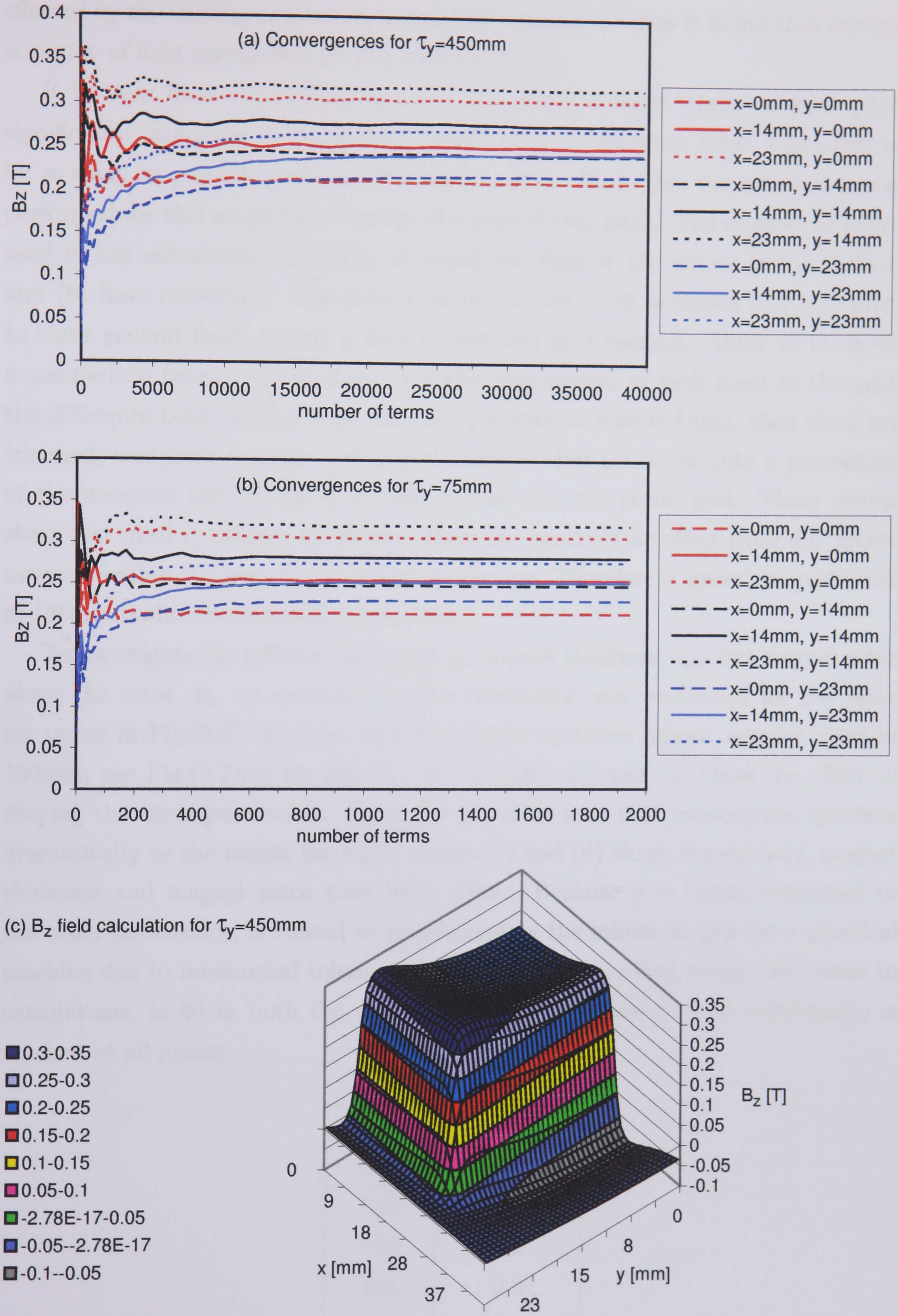

Figure 5.6: Influence of 'ghost' magnets pitch on convergence

effected by the various paramters, a standard number of terms is found that ensures accuracy of field calculation for any particular case.

It is clear from Fig.(5.6)(a) and (b) that using a large 'ghost' magnet pitch significantly slows the convergence. Therefore, it is useful to select this pitch to be as small as possible without affecting the field. To do this the calculation was performed for this setup for a variety of values of this pitch. The number of terms used in the calculation is 40,000, at which the field at the points in Fig.(5.6)(a) and (b) have converged. The field with the largest pitch is shown in Fig.(5.6)(c) to show general form, x and y ranges used and grid spacing. Table (5.1) shows a comparison between these cases. For the comparison, at each point in the grid, the difference between that case and the $\tau_y = 450$mm case is found, then these are summed, unsigned, over the entire grid. This is then converted into a percentage of the unsigned sum of the $\tau_y = 450$mm calc over the entire grid. These results show that until τ_y reduces to 100mm, there is essentially no effect from the 'ghost' magnets within the area that a coil might occupy. Therefore a 'ghost' magnet pitch of 150mm is chosen for use in calculations.

To investigate the influence of height, g, magnet thickness, t_m, and magnet pitch along the rotor, τ_x, on convergence, the calculation was performed for the same set up as in Fig.(5.6) but now with the chosen optimum 'ghost' magnet pitch of 150mm, see Fig.(5.7)(a) for results. Fig.(5.7)(b), (c) and (d) show the effect of varying the three parameters. From (b) it can be seen that convergence quickens dramatically as the height increases, whilst (c) and (d) show, respectively, magnet thickness and magnet pitch have little effect. Because $g = 1$mm, compared to the other dimensions, is viewed as approximately the minimum gap for a practical machine due to mechanical tolerances, Fig.(5.7)(a) shows that using 2500 terms in calculations, ie 50 in both the x and y series, would ensure that convergence is reached at all points.

pitch p_y mm	comparison %
300	0.3
150	0.3
100	0.8
75	6.1

Table 5.1: Influence of 'ghost' magnet pitch, p_y, on field B_z calculation

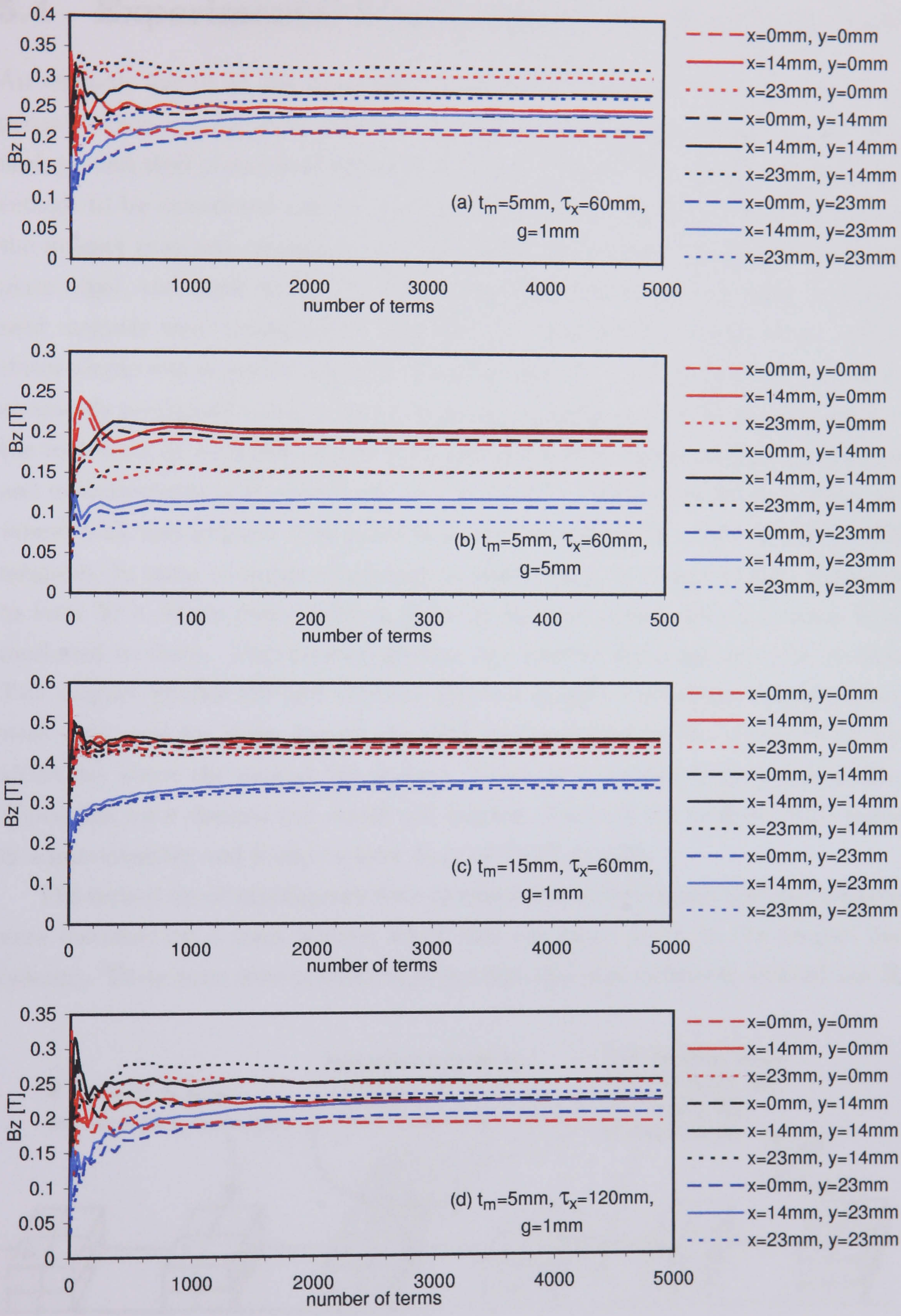

Figure 5.7: Effects of height, g, magnet thickness, t_m, and magnet pitch, τ_x on 3D Model Convergence

5.4 Experimental Measurement of Magnetic Field

An example layout of the apparatus is shown in Fig.(5.8). The first set of experiments was conducted to validate the 3D analytical model. Two 12.5mm thick flash ground steel plates were clamped together to form a 25mm thick surface, large enough to be considered infinite (henceforth referred to as $B_{z(\infty)}$) with respect to the magnet pole size (minimum of 50mm clearance between the magnets and the plate edge), and thick enough to avoid saturation. Six alternating poles of permanent magnets were arranged in a line on this. This physical model of an ironless stator airgap was mounted on a travelling carriage of a machine tool which could be accurately positioned using a digital readout. A gaussmeter probe was mounted on the tool head, at a certain height above one of the two middle magnets of the line, and measurements of B_z were taken in a grid pattern as the travelling carriage was wound back and forward. The poles were assembled from 25 x 24 x 2.5mm NdFeB magnets. In order to improve accuracy in positioning, the magnets were combined to form 50 x 48mm poles, held in place by slabs of plastic with pole-sized holes machined in them. This avoided glueing and allowed the magnets to be re-used. Two magnet pitches (60 and 120mm) and two magnet thicknesses (5 and 10mm) were used, and for these 4 cases the field was measured in two planes (5.29 and 15.29mm) above the magnet top surface. These were deemed to be representative of possible rotor designs and stator coil heights. Three of the magnets were tested in a permeameter and found to have B_{rem} of 1.12T $\approx \pm 2\%$.

The second set of experiments were identical to the first except that the magnets were mounted on a steel backing which was the same width as the magnet line (48mm). These tests were conducted to see how this edge condition affected the B_z

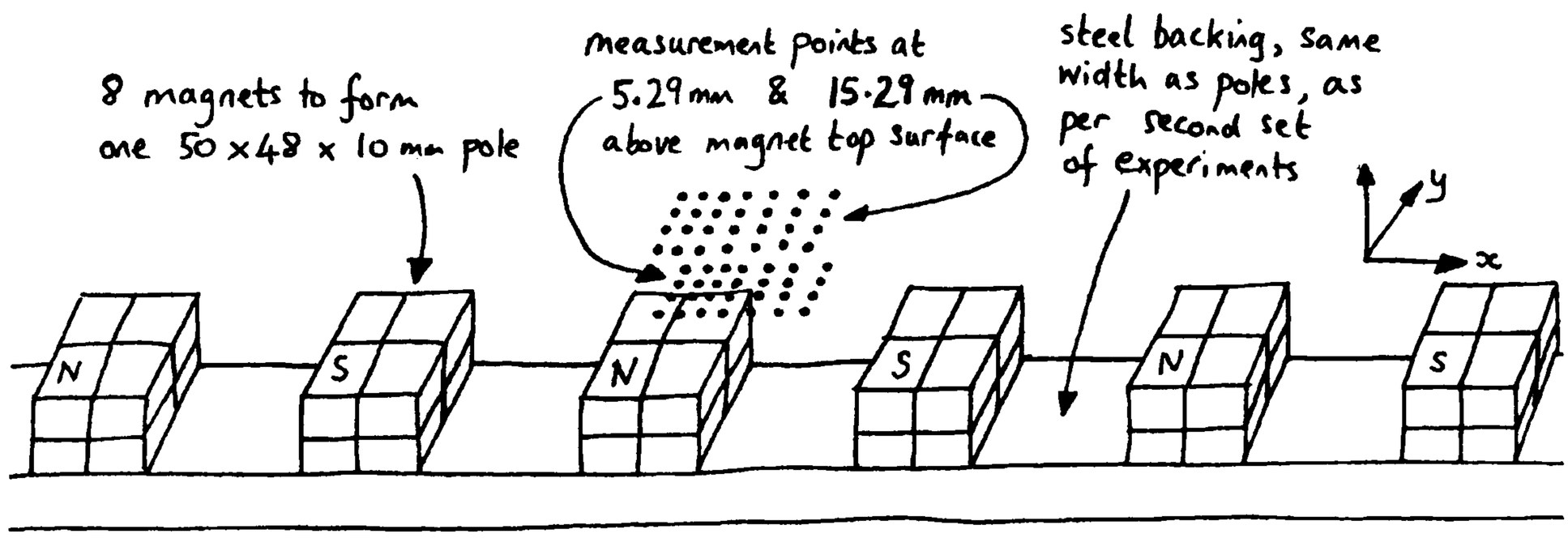

Figure 5.8: Example Experimental Setup

field, as the analytical models cannot take account of it, but it is a likely feature of any rotor. These are henceforth referred to as $B_{z(edged)}$

5.4.1 Sensor Position Within Probe

The guassmeter was used with a 1mm thick probe containing a 0.2 x 0.2mm Hall sensor, effectively giving point measurement of the field wrt the scale of the apparatus. However, the height of the sensor within the 1mm thickness was not known so some tests were conducted to estimate this, similar to the main experimentation, for a variety of x, y positions above the magnet surface:

(i). B_z was measured at the surface of the magnet, with the probe inverted, physically pressing the probe down onto the magnet surface to ensure the same height every time.

(ii). This was then repeated but with the probe the 'right' way up.

(iii). Finally it was repeated at a 1mm height above the magnet surface, with the probe the right way up.

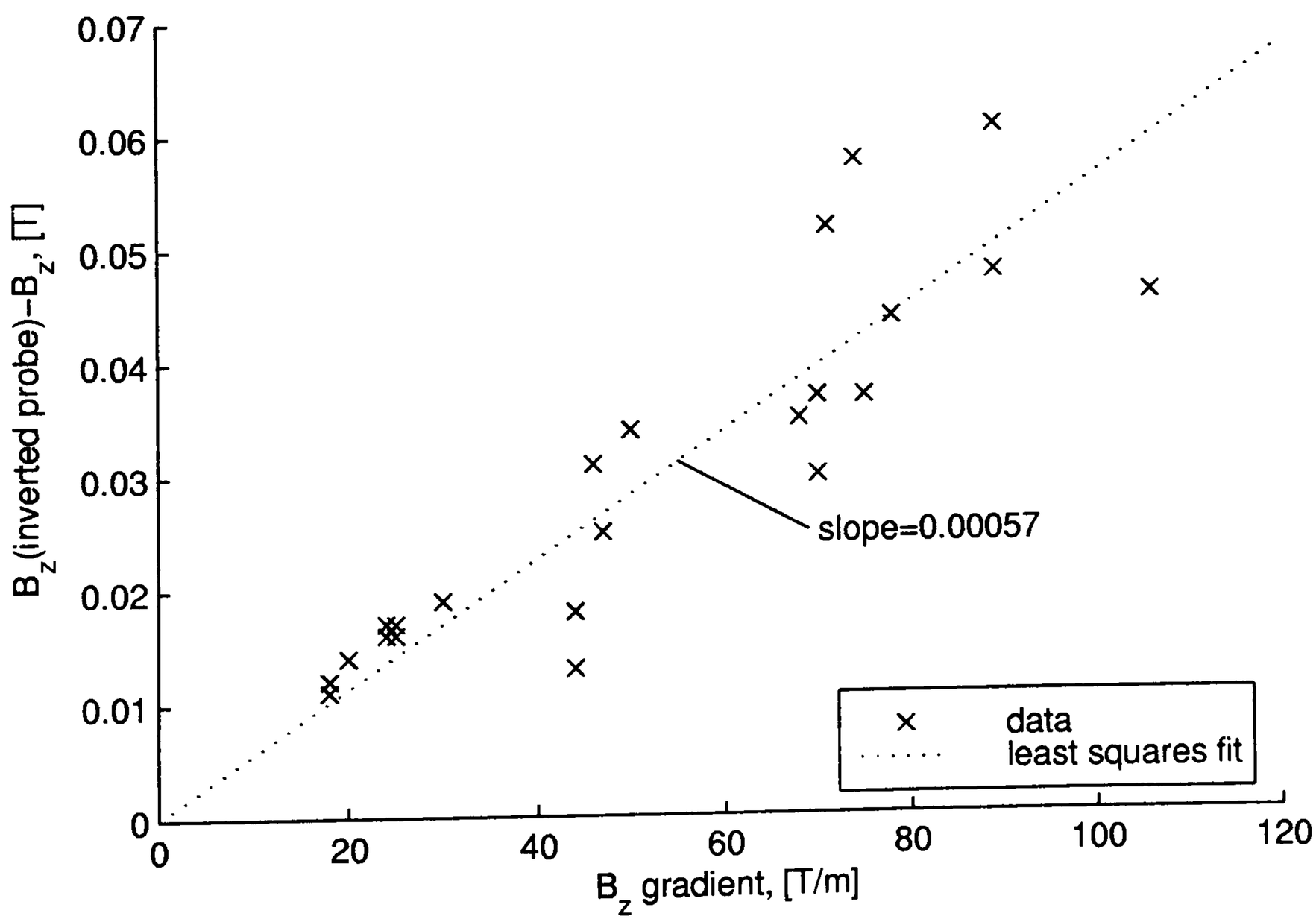

Figure 5.9: Estimation of Sensor Offset within Probe Thickness

(ii)-(iii) gives the field drop-off over a 1mm distance, so the gradient of the field can be estimated in T/m at each point. (i)-(ii) gives the field difference for the unknown height difference due to the sensor offset within the probe. Fig. (5.9) shows the field gradients vs. (i)-(ii) for each point. The slope of this graph is the difference in height of (i) and (ii), so halving it gives the offset of the sensor from the centreline of the probe. (i) gives higher readings than (ii) , so they must be closer to the magnet surface, meaning that when the probe is the 'right' way up, it has the sensor 0.29mm higher than the midpoint. Therefore, a better estimation of the z position of the sensor is obtained by adding 0.29mm to to the height measurement to the midpoint of the probe.

5.5 Discussion & Conclusions

Figs(5.10) & (5.11) show the experimental measurements and the 3D model calculations. Some characteristics of note are:

- Comparing the infinite rotor plate data with the model calculations shows a very good fit.
- Comparing the two experimental data sets shows that the edged condition increases B_z near the plate edge, and this is more significant in the cases with the thinner magnets, and the cases closer to the magnet surface.
- There is a rapid drop-off of B_z with height above the magnet, and also the change in the form of B_z.
- For the two cases with magnet thickness, t_m, =5mm, at height above magnet top surface, g, =5.29mm, B_z is greater at the edges than it is closer to the centre.
- For the two cases of τ_x=120mm, at g=5.29mm (and to a lesser extent the τ_x=120mm, t_m=5mm, g=15.29mm case), there are three reversals of the flux direction between poles, compared with one reversal for the τ_x=60mm case.

It is worth considering what happens to the B_z component of the fields of the individual magnets (of alternating polarity) on the rotor as the distance between them, τ_x is decreased. For an individual 'north' magnet there is a (+ve) central region, then a (-ve) fringe region around the magnet edges which then tails off to zero a little distance from the magnet. As a south pole approaches it, the (-ve)

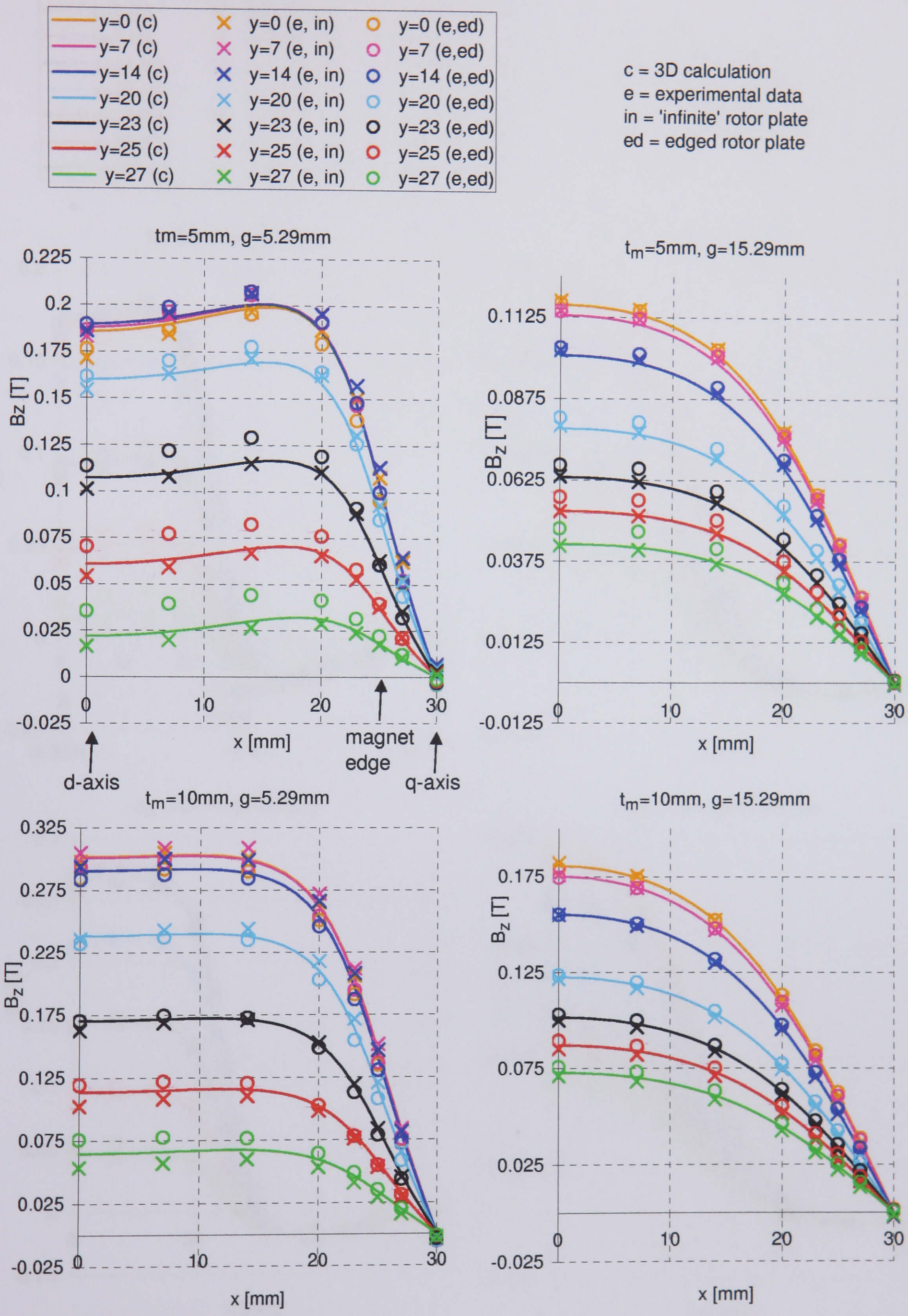

Figure 5.10: B_z experimental and 3D model results for magnet pitch=60mm

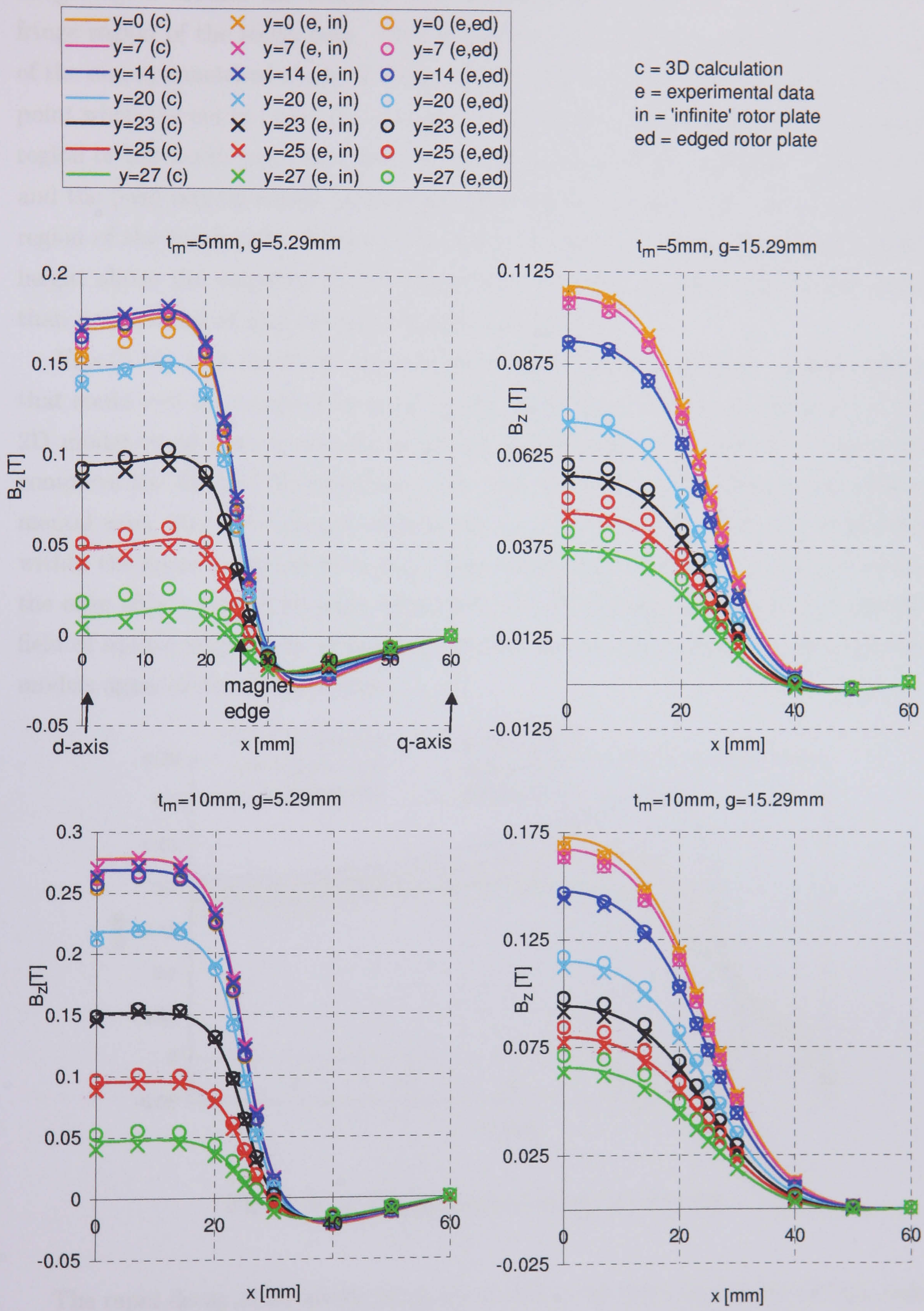

Figure 5.11: B_z experimental and 3D model results for magnet pitch=120mm

fringe region around the magnet edge is partially cancelled by the similar (+ve) fringe region of the south pole. This will never be a complete cancellation because of the non-symmetrical shape of these regions. Moved closer together there comes a point when the entire (+ve) fringe region of the south pole adds to the (+ve) central region of the north pole, and there is no cancellation of B_z anywhere. Closer still and the (-ve) central region of the south pole starts to cancel out the (+ve) central region of the north pole. However, the pitch at which all this occurs will vary with height above the magnets. It is unlikely that a practical design will include more than one reversal of flux between adjacent magnets.

Figs.(5.10) & (5.11) show large variations of B_z in the y-direction, within regions that could well be occupied by an optimum coil design. This means that use of the 2D model could lead to significant errors in flux linkage calculations. Fig.(5.12) compares the 2D and 3D solutions above the centreline of the rotor of the experimental work with t_m=5mm, τ_x=60mm, at $y = 0$, at 3 heights which might well fall within the space occupied by a coil. This shows that, along the centreline, where the edge effects should be least influential, the 2D solution underestimates the 3D field of square magnets by of the order of 10% at low values of x, but then the two models agree at the magnet edge.

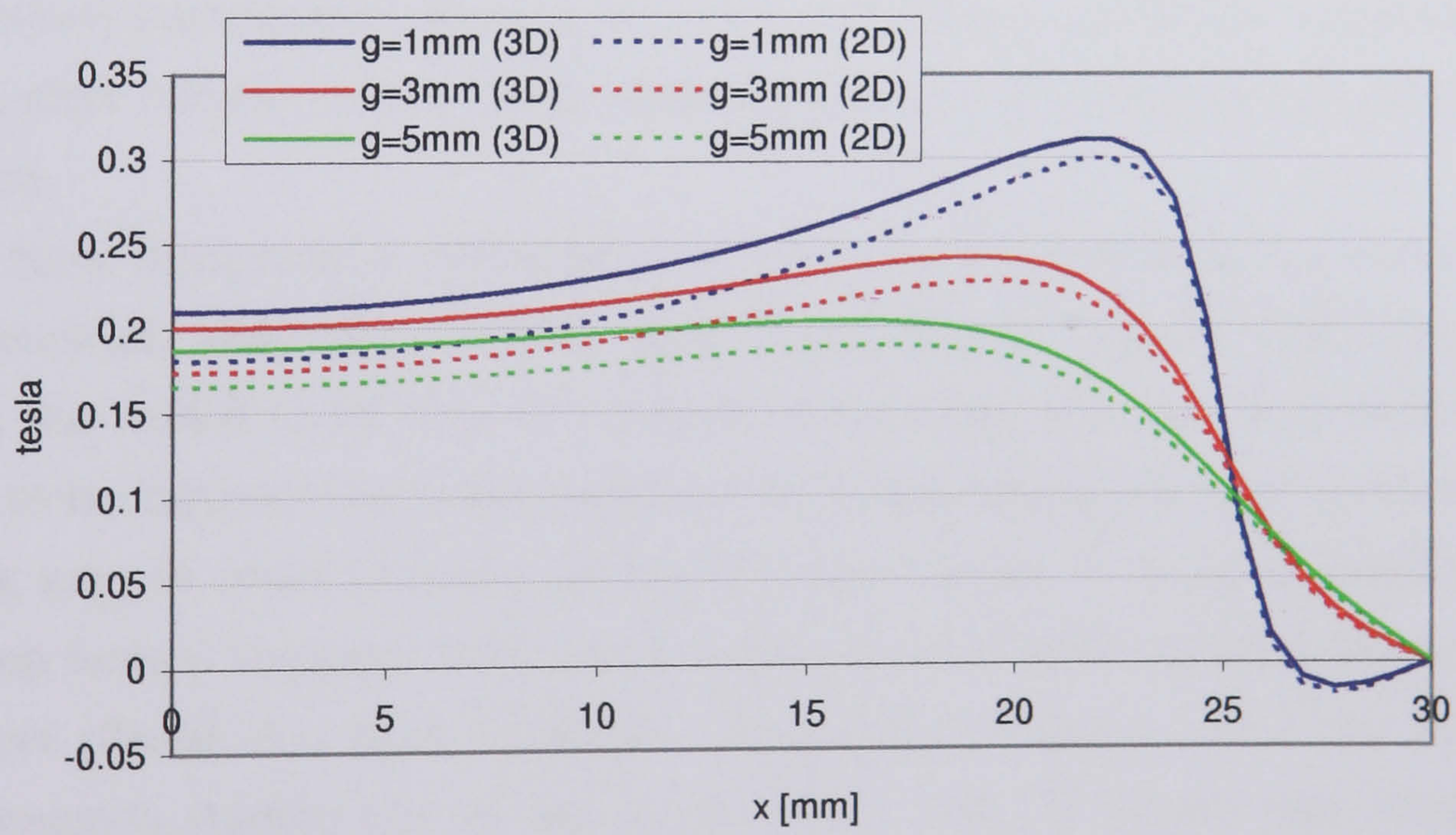

Figure 5.12: Comparison of 2D & 3D Models

The rapid decay of B_z above the magnet surface necessitates the use of thin coils in order to stay within high flux regions. These coils will therefore have to be of a distributed nature to allow sufficient turns. That, coupled with the complicated field topology make optimum coil-shape non-trivial.

Chapter 6

SLiM1 Prototype

A small prototype SLiM was constructed in order to gain practical experience of building one, and to obtain experimental measurements of open circuit voltage, self and mutual inductances, and power produced to compare with modelling work.

6.1 Design

The generator, referred to as SLiM1, see Fig.(6.1), was mainly constructed from bicycle wheel components. Basing the rotor and stator on different diameter wheels allowed, after addition of the electromagnetic components, the rotor to still fit inside the stator.

The rotor comprised a mountain bike wheel ie hub, bearings, XX cross spoking and aluminium alloy rim. A thin steel hoop, 37.5mm axially and 4.5mm thick radially, was rolled to fit over the outside of the rim, and lugs were welded on to allow it to be tightened on using hoop stress. Magno-paste was used to fill the small resulting gap, in order to maintain the flux path there as much as possible. This steel hoop formed the rotor back iron onto which 34 alternating neodymium magnet poles were placed at a pitch of 50mm. Each pole was made up of two 2.5 x 24 x 25mm magnets stacked one on top of the other, with the 25mm edge being in the axial direction. To stop the magnets sliding on the rotor without gluing them down, small rectangular pieces of aluminium sheet were fitted between the poles and held in place with duct tape.

The stator comprised a racing bike wheel ie hub, bearings, YY cross spoking and aluminium alloy rim. A second identical rim was cantilevered off this wheel using 6 aluminium beams. This cantilevered arrangement was chosen as it avoided dismantling the wheel to fit the rotor wheel inside, and also avoided adaption of

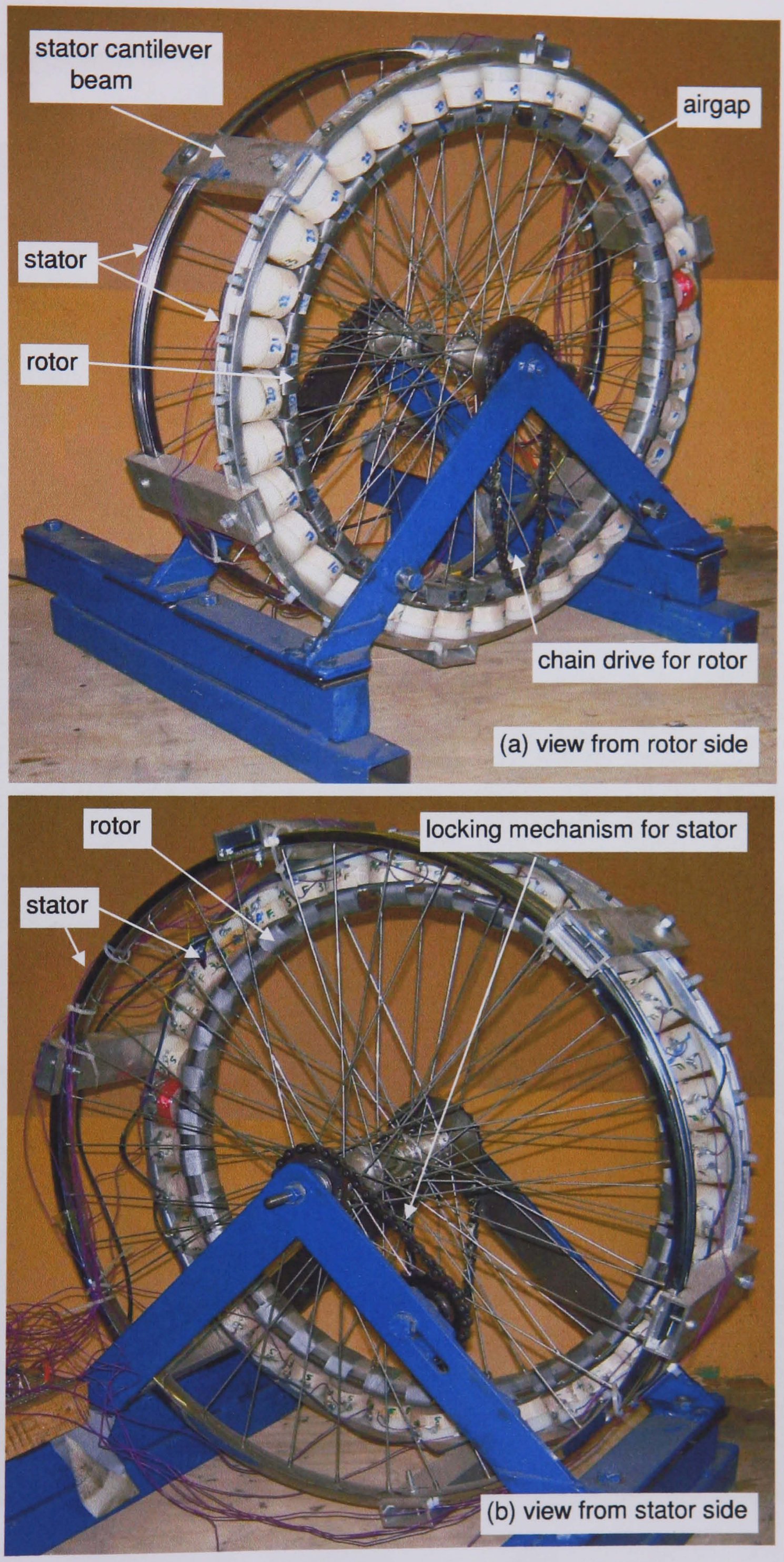

Figure 6.1: SLiM1 laboratory demonstrator

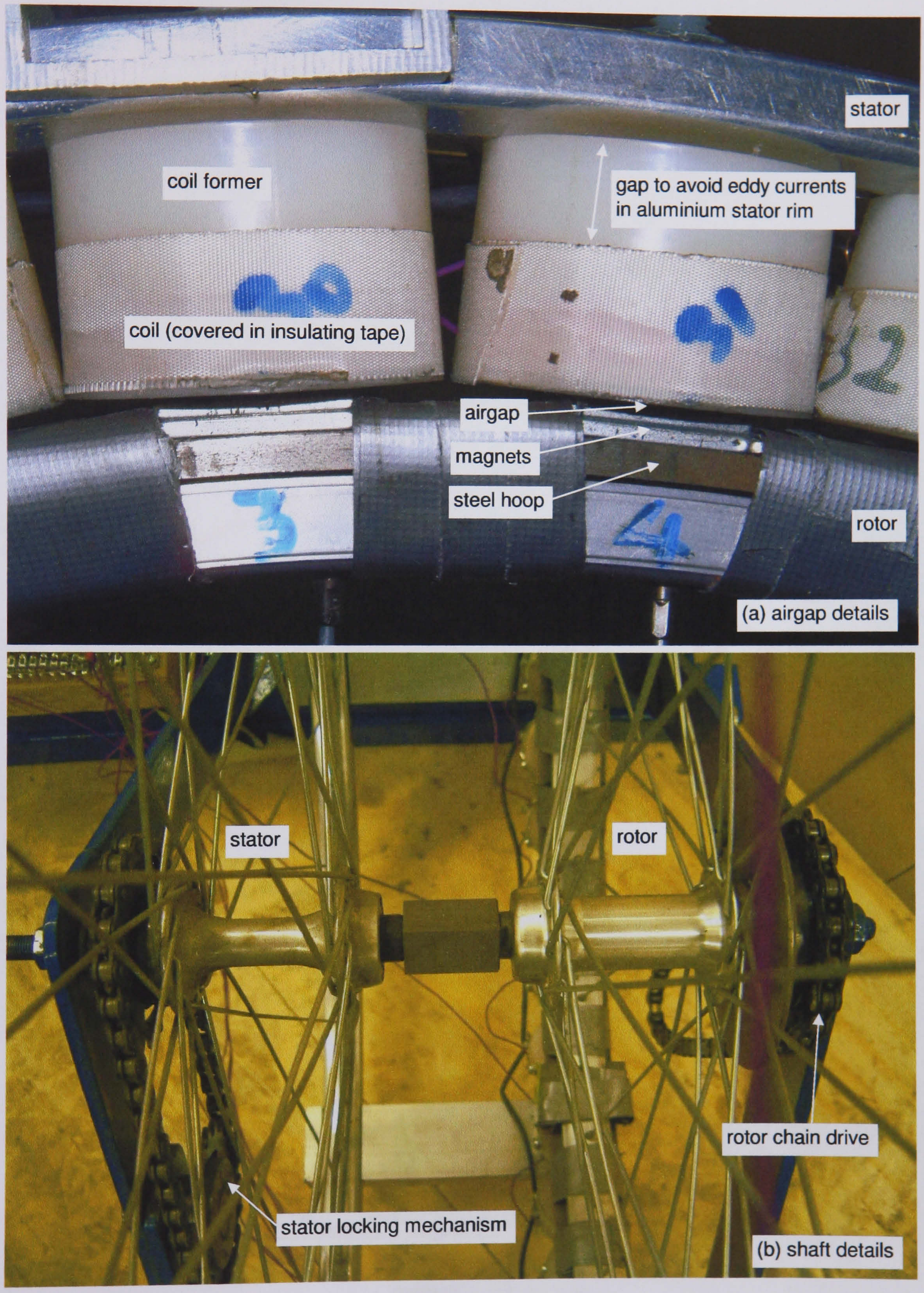

Figure 6.2: SLiM1 laboratory demonstrator

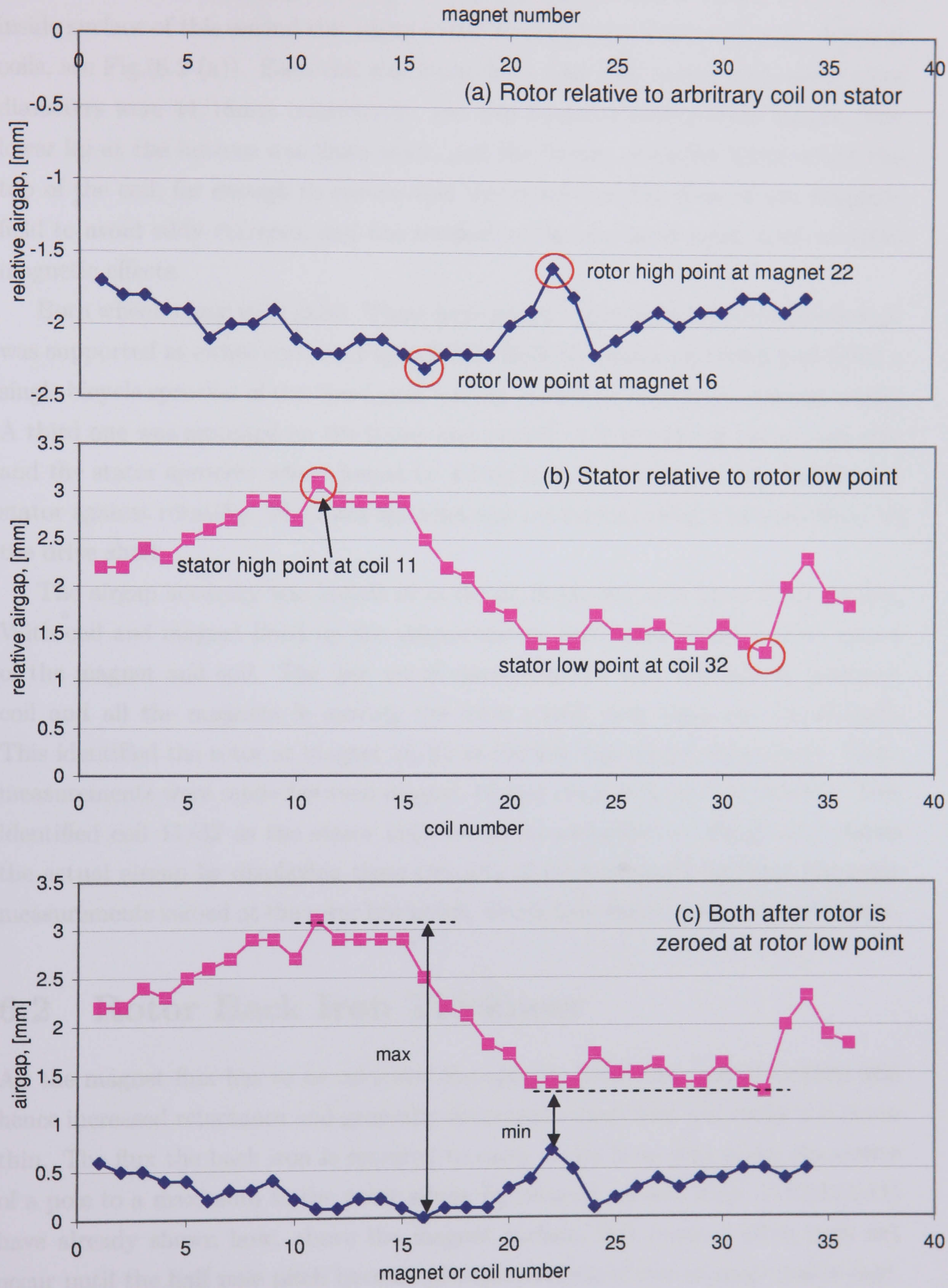

Figure 6.3: SLiM1 airgap measurements

the hub to allow a rolling bearing on one side of the stator wheel. On to the inside surface of this second rim where fitted 36 cylindrical, fractional pole, modular coils, see Fig.(6.2 (a)). Each coil was 9mm deep, had 1300 turns, with outer/inner diameters were 44/16mm respectively, and was wrapped onto a nylon former. The lower lip at the bottom was 2mm thick, and the former extended 22mm above the top of the coil, far enough to ensure that the stator rim was clear of the magnetic field to avoid eddy currents, and was secured to the rim using nylon bolts to avoid magnetic effects.

Both wheels came with axles. These were joined together and the combined shaft was supported at either end, see Fig.(6.2(b)). Both the stator and rotor had fitted a single bicycle sprocket of the 'fixed gear' variety ie with no freewheel/bearings inside. A third one was mounted on the frame and pinned so it would not rotate, and this and the stator sprocket where joined by a length of bicycle chain, thus locking the stator against rotating. The rotor sprocket was connected, using a bicycle chain, to the drive shaft.

The airgap accuracy was looked at in detail, measured with brass feeler gauges. With coil and magnet lined up the measurements were made in the central region of the magnet and coil. The first set of measurements were between an arbitrary coil and all the magnets ie moving the rotor round each time, see Fig.(6.3(a)). This identified the rotor at magnet 16/22 as the low/high point respectively. Next, measurements were made between magnet 16 and every coil, see Fig.(6.3(b)). This identified coil 11/32 as the stator high/low point respectively. Fig.(6.3(c)) shows the actual airgap by displaying these two sets of measurements but with the rotor measurements zeroed at the rotor low point. The airgap range was 0.5mm to 3.1mm.

6.2 Rotor Back Iron Thickness

All the magnet flux has to be returned through the back iron, and saturation and hence increased reluctance and generally decreased airgap field will result if it is too thin. The flux the back iron is required to carry varies from zero under the centre of a pole to a maximum at the point where B_z reversal occurs. Figs. (5.10)&(5.11) have already shown how, above the magnet surface, this reversal often does not occur until the half pole pitch because of superposition of the adjacent pole's field. However, at the back iron surface, the reversal always occurs at the magnet edge.

For a 2D rotor, all the flux returns in the x-direction, and is equal to the integral, over $x = 0$ (at the magnet centre) to x, of B_z at the back iron surface, see

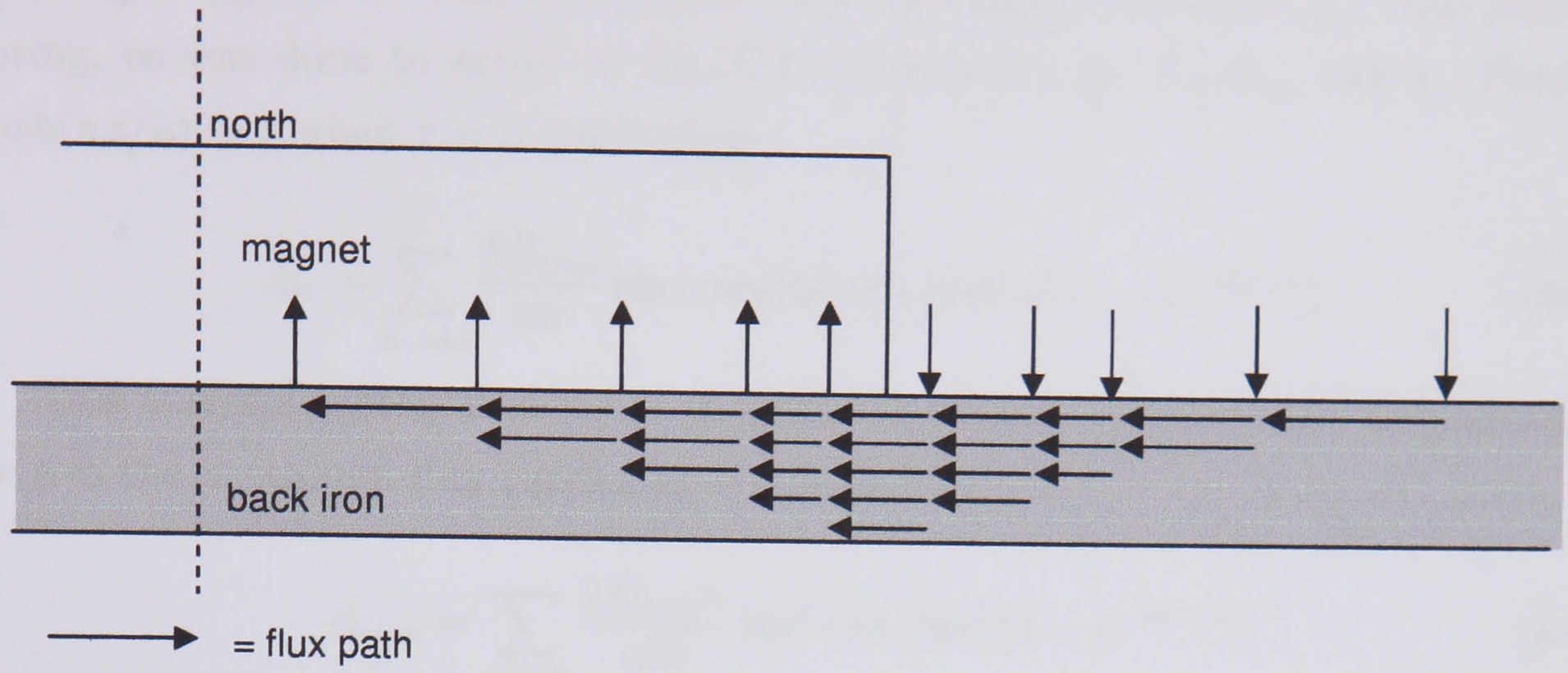

Figure 6.4: Flux Return Path for a 2D Rotor

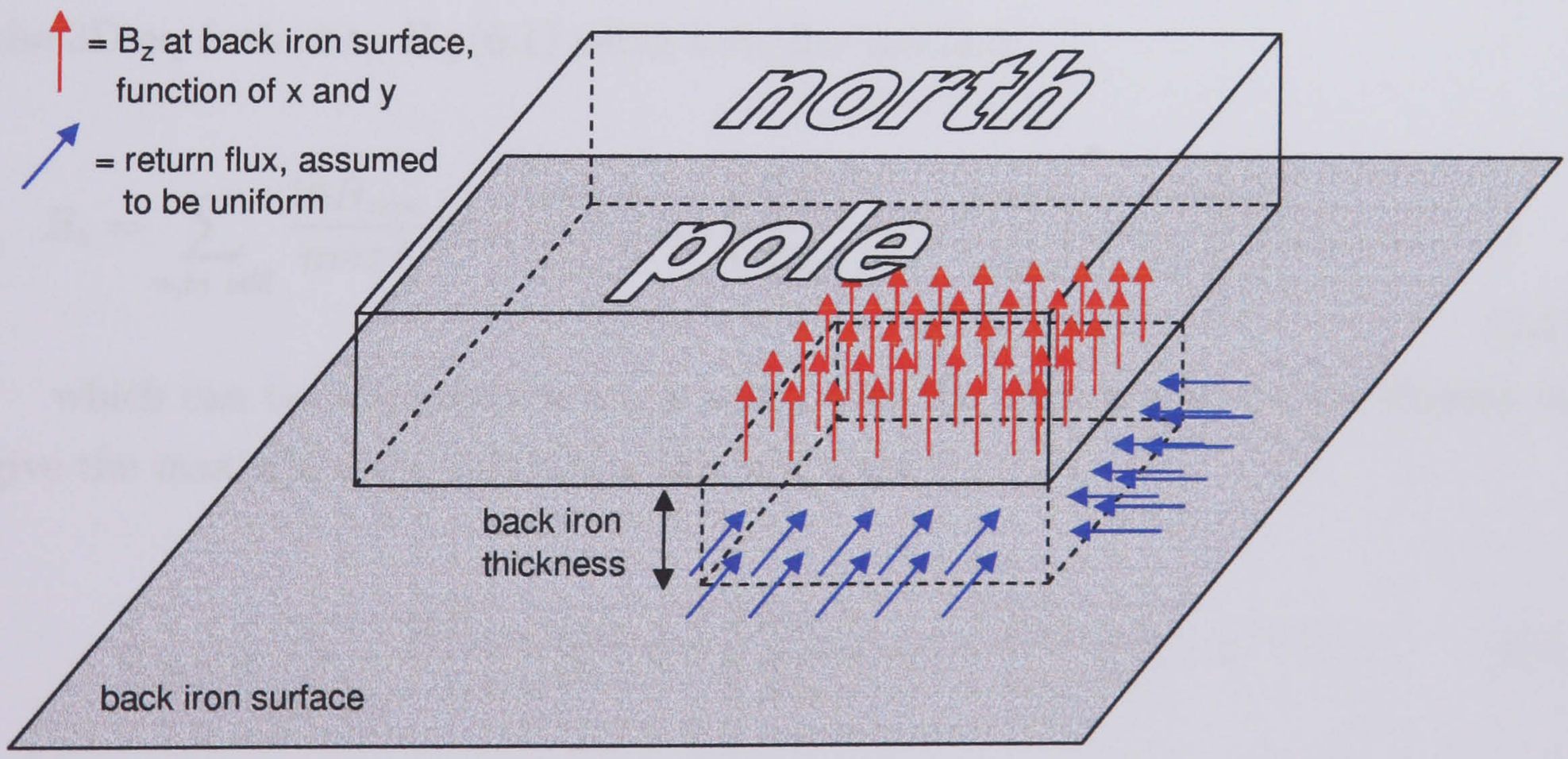

Figure 6.5: Approximated Flux Return Path for a 3D Rotor

Fig.(6.4). In Chapter 5, Eq.(5.31) was developed for the field *above* the magnet surface. However, here the field *below* it is required. This can be found from Eq.(5.28) by integrating the $e^{-kz_e}\delta z_e$ component over the magnet thickness t_m. then substituting, as was done to arrive at Eq.(5.31) previously, for K_n, K_m and k. Finally $cosh(nz/u) = 1$ when $z = 0$, producing:

$$B_z = \sum_{n\ odd} \frac{4B_{rem}}{n\pi} \sin(nw/2u) \cos(nx/u) \left(1 - e^{-nt_m/u}\right) \tag{6.1}$$

This is simply integrated w.r.t. x, from the magnet centre to the magnet edge to give the maximum flux carried by the back iron:

$$\phi_{max} = \sum_{n\ odd} \frac{4B_{rem}u}{n^2\pi} \sin^2(nw/2u) \left(1 - e^{-nt_m/u}\right) \tag{6.2}$$

and the minimum back iron thickness to avoid saturation is ϕ_{max}/B_{sat} where B_{sat} is the saturation limit for the steel, which is taken to be a typical 1.5 Tesla.

For a 3D rotor, the exact situation is more complex, with the return path of the flux being in both the x and y directions. However, as the B_z field reverses at the magnet edge, the maximum return flux can be found by summing over the back iron surface covered by the magnet. An accurate approximation of the required minimum back iron thickness is obtained by assuming all the flux returns in a uniform fashion across the steel cross section, see Fig.(6.5). Chapter 5, Eq.(5.59) can be used to give the 3D equivalent to Eq.(6.1) using a similar method:

$$B_z = \sum_{n,m\ odd} \frac{16B_{rem}}{nm\pi^2} \sin\left(\frac{nw_x}{2u_x}\right) \sin\left(\frac{mw_y}{2u_y}\right) \cos\left(\frac{nx}{u_x}\right) \cos\left(\frac{my}{u_y}\right) \left(1 - e^{-k_z t_m}\right) \tag{6.3}$$

which can be integrated w.r.t. x and y over the area covered by the magnet to give the maximum flux carried by the back iron:

$$\phi_{max} = \sum_{n,m\ odd} \frac{16B_{rem}u_x u_y}{(nm\pi)^2} \sin^2\left(\frac{nw_x}{2u_x}\right) \sin^2\left(\frac{mw_y}{2u_y}\right) \left(1 - e^{-k_z t_m}\right) \tag{6.4}$$

50 terms are used in both the x and y directions for the calculation as this seems to give good convergence, and is the same as used in magnetic field calculations. Minimum back iron thickness to avoid saturation is $2\phi_{max}/(B_{sat}(w_x + w_y))$. For SLiM1 this is 2.3mm.

6.3 Open Circuit Voltage, V_{oc}

6.3.1 Open Circuit Voltage Measurements

To allow checks on the effects of the variations in the airgap. two V_{oc} tests were conducted on SLiM1, one at the stator high point, coil 11, and one at the stator low point, coil 32. All other coils were ensured to be open circuit also during the tests. An optical r.p.m. counter was used on the rotor hub to measure speed, and the oscillosope allowed the capture the voltage waveform for just over 2 revolutions. Fig.(6.6(a)&(b)) show the results, but in both the waveform has been split and laid over the same timescale to check if the waveform is the same for both rotations. If the waveforms were to be related to the position of the magnets, and hence the measured airgap variations, some reference was required on the waveform. Therefore magnet 1 was removed from the rotor and the effect can be clearly seen in Fig.(6.6(a)&(b)). The waveforms at minimum/maximum airgap, Fig.(6.6(c)/(d)) respectively, were extracted from Fig.(6.6 (a)/(b)) respectively. Each has two data sets, one from each mechanical rotation.

6.3.2 Open Circuit Voltage Modelling

Adaption of B_{z_2total}

The first requirement in this particular scheme for calculating V_{oc} is calculation of the magnetic field throughout the region occupied by the coil. The 3D Fourier series solution for B_{z_2total} of Chapter 5 requires calculations not only to be done at a specific x, y position above the magnets, but also at a specific height z, so for a coil the calculation would have to be made on a series of z planes within the coil thickness. However, inspection of Eq.(5.65) shows that only one part of it is a function of z, which can be analytically integrated through the coil thickness. If that part of Eq.(5.65) is called $f(z)$ then:

$$f(z) = e^{-k_z z} \tag{6.5}$$

The average of $f(z)$ over coil depth t_c is

$$\frac{1}{t_c}\int_{t_m+g}^{t_m+g+t_c} f(z)dz = \left[\frac{-e^{-k_z z}}{k_z}\right]_{t_m+g}^{t_m+g+t_c} \tag{6.6}$$

$$\frac{1}{t_c}\int_{t_m+g}^{t_m+g+t_c} f(z)dz = -\frac{1}{k_z}e^{-k_z(t_m+g)}\left(1-e^{-k_z t_c}\right) \tag{6.7}$$

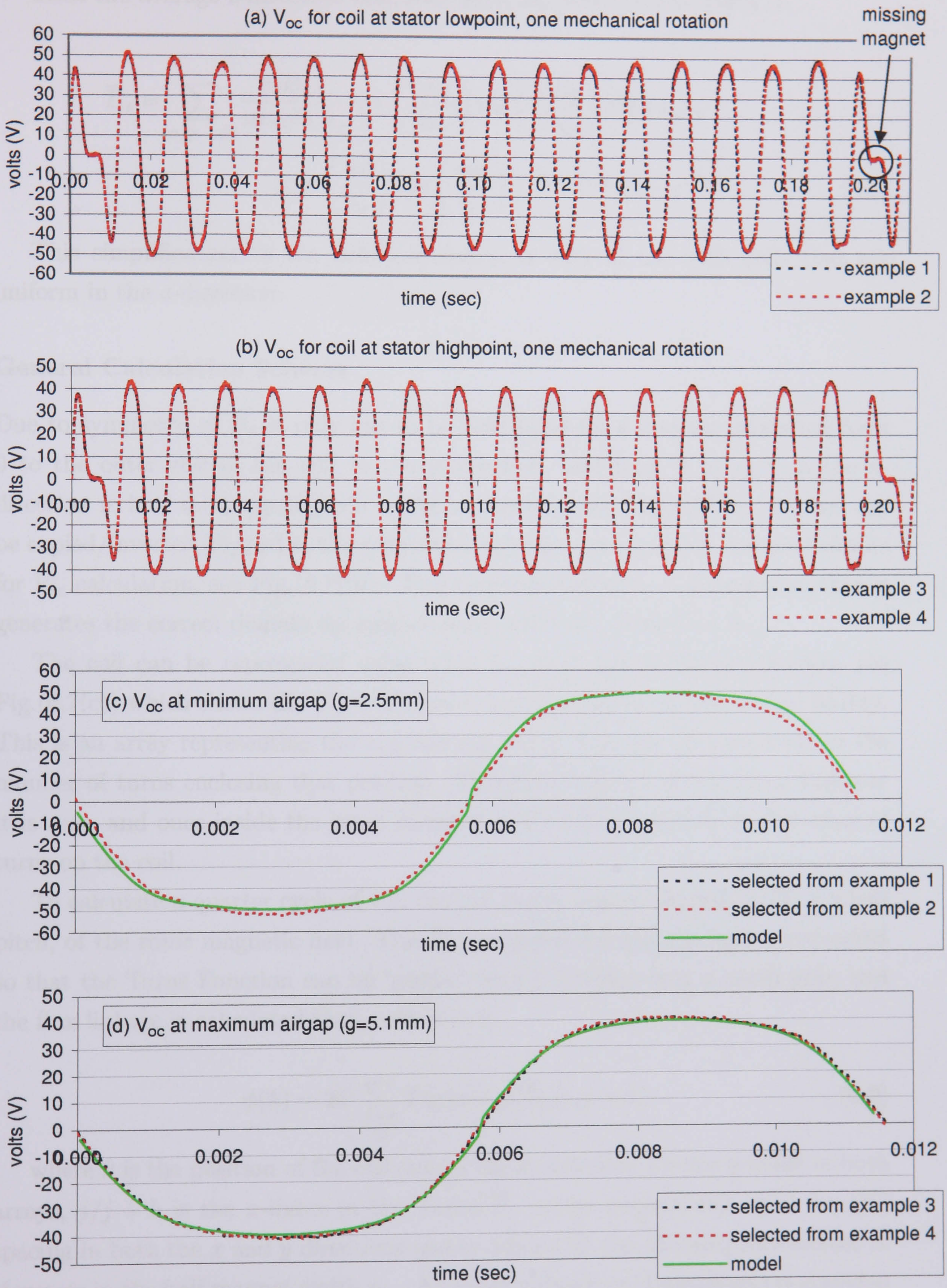

Figure 6.6: Open Circuit Voltage Experimental and Model Results

Then the average z-direction magnetic field, $\overline{B}_z$ over the coil depth is

$$\overline{B}_z = \sum_{n,m\ odd} \frac{16B_{rem}}{nm\pi^2 t_c k_z} \sin\left(\frac{nw_x}{2u_x}\right) \sin\left(\frac{mw_y}{2u_y}\right) \sinh k_z t_m \cdots$$
$$\cos\left(\frac{nx}{u_x}\right) \cos\left(\frac{my}{u_y}\right) e^{-k_z(t_m+g)} \left(1 - e^{-k_z t_c}\right) \tag{6.8}$$

This simplification to the field calculation is only of use with coils that are uniform in the z-direction.

General Calculation Scheme

Due to symmetry of $\overline{B}_z$ it only has to be calculated for a domain extending from 0 to the outer end of the coil in the y-direction, and from 0 to $\tau_x/2$ in the x-direction ie half the magnet pitch in the x-direction, see Fig.(6.7(a)). It then can be copied/inverted/flipped in the x-direction to create an expanded domain suitable for V_{oc} calculation, see Fig.(6.7(b)). This copying procedure is arranged so that it generates the correct domain for coils of outer width w_{co} from 0 to $2\tau_x$.

The coil can be represented using what is called here a Turns Function, see Fig.(6.7(c)) which shows the Turns Function for the cylindrical coil used in SLiM1. This is an array representing the x, y coil region, showing for all x, y positions the number of turns enclosing that position. Therefore, outside of the outer diameter it is zero, and once inside the inner diameter it is constant at the total number of turns on the coil.

To calculate a quarter cycle of V_{oc}, the coil has to 'move' through $\tau_x/2$, ie a half pitch, of the rotor magnetic field. The $\overline{B}_z$ expanded domain has been constructed so that the Turns Function can be 'placed' with it's centre over a north pole, and the flux linkage is calculated thus, with $k = 0$:

$$\phi(k) = 2\delta^2 \sum_{i,j} Turns(i,j)\overline{B}_z(i, j+k) \tag{6.9}$$

where k is the position of the coil axis in the x-direction, i is the y-index in both arrays, $j/j+k$ is the x-index in the Turns/$\overline{B}_z$ arrays respectively. δ is the grid spacing in both the x and y directions and is defined by the choosing the number of elements in the half magnet width w_x. All other x direction dimensions are rounded to integer δ. The factor of 2 is included because the arrays only represent the domain on one side of the x-axis.

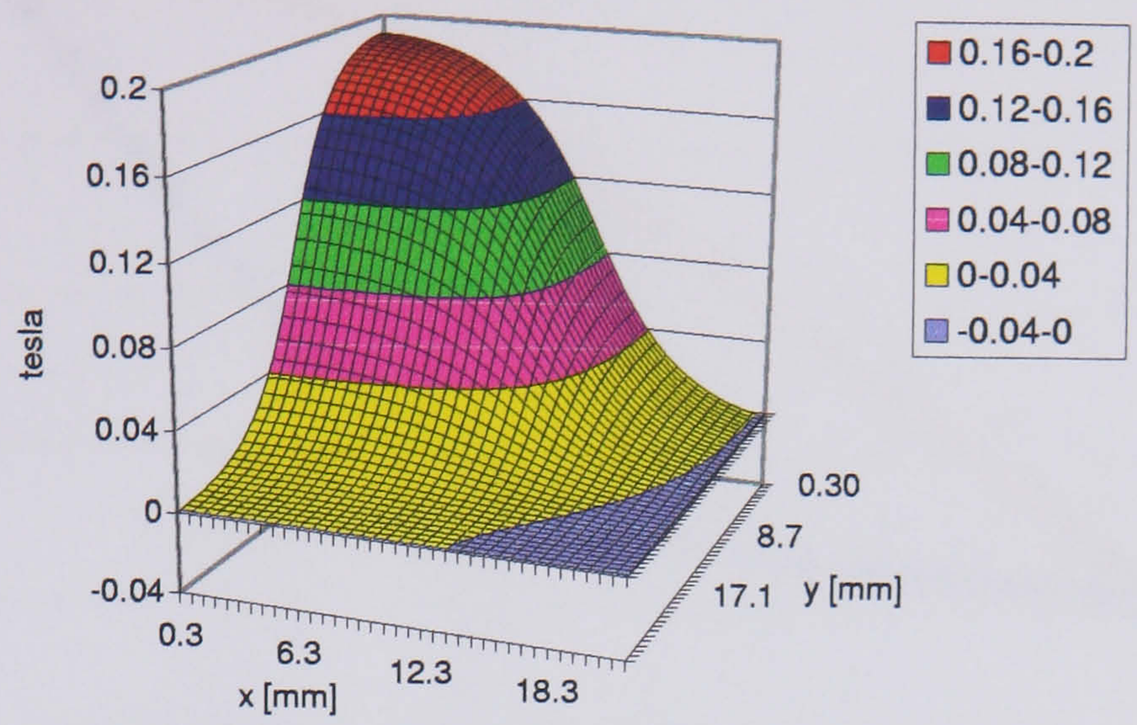

(a) Calculated z direction average magnetic field

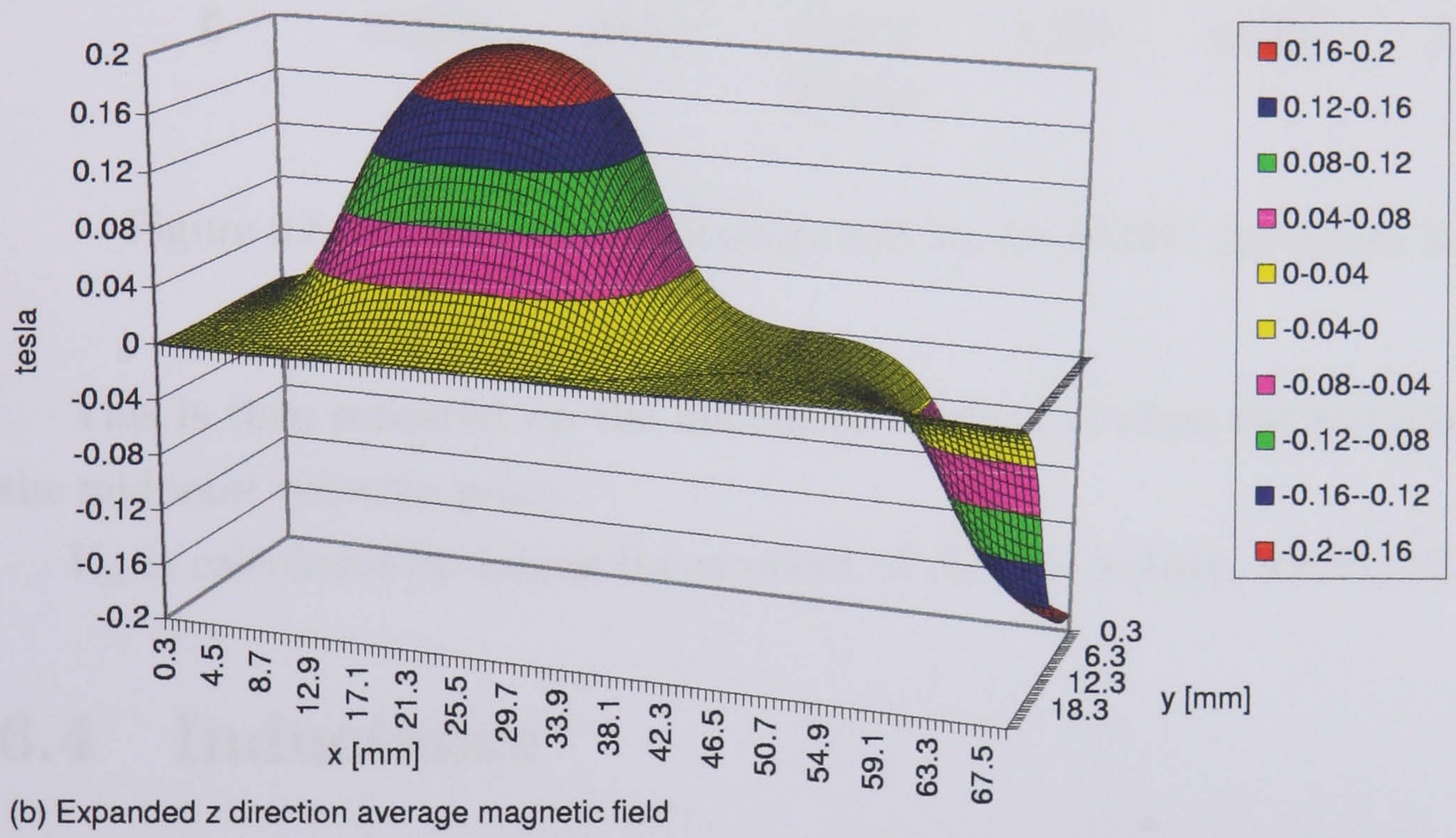

(b) Expanded z direction average magnetic field

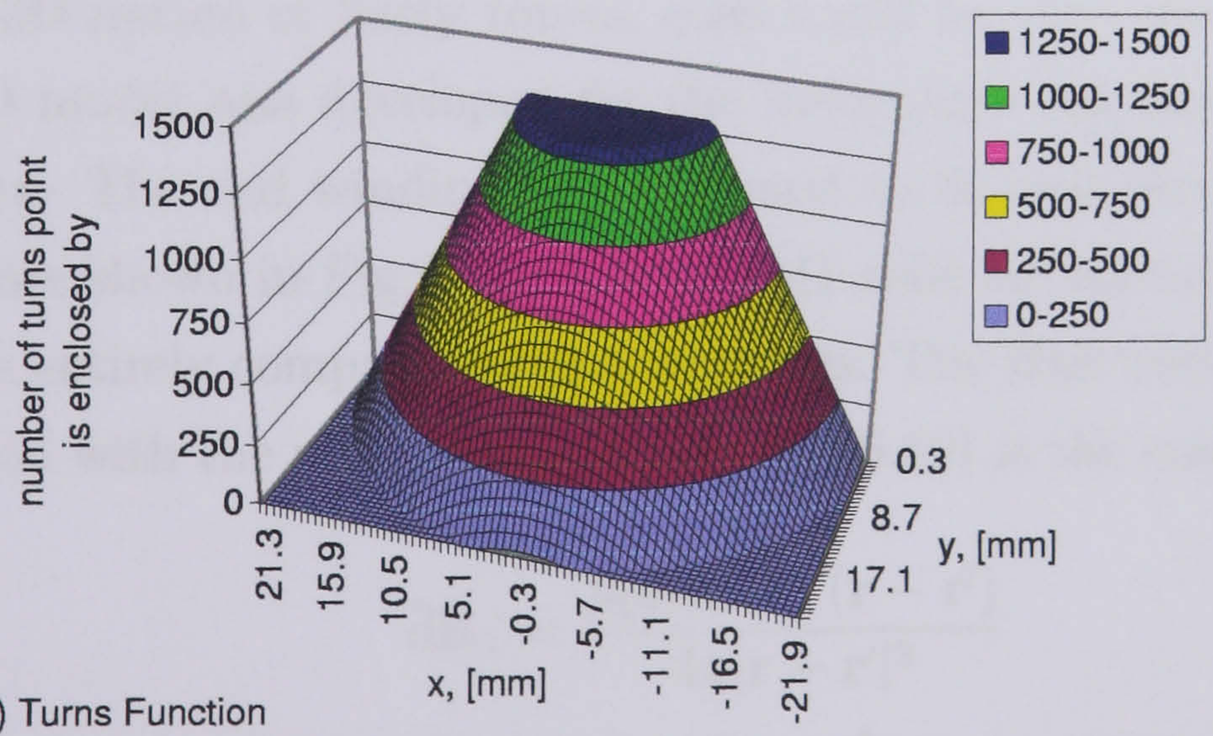

(c) Turns Function

Figure 6.7: Stages in modelling V_{oc} for SLiM1 minimum airgap

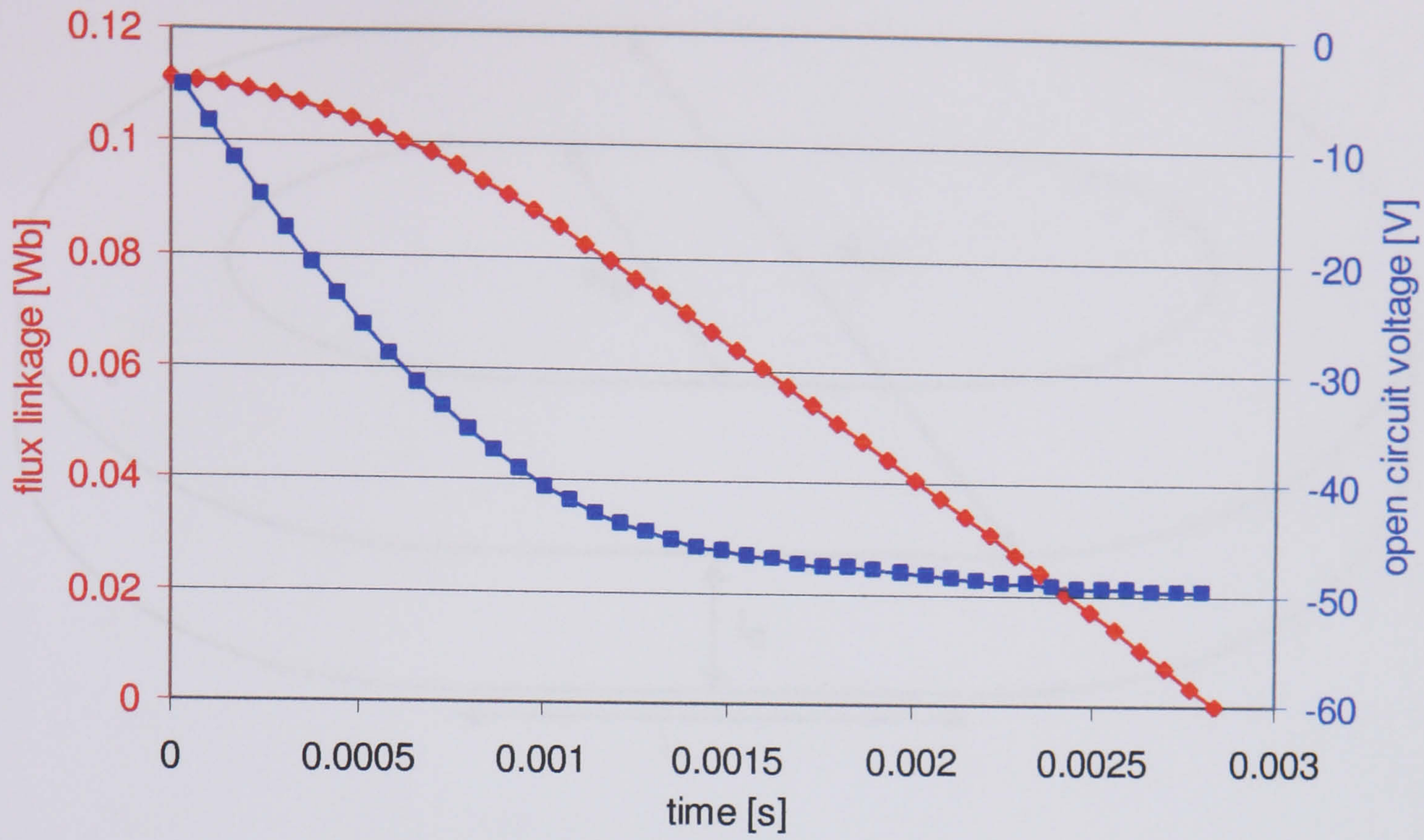

Figure 6.8: Calculated flux linkage and V_{oc} for SLiM1 minimum airgap

This is then repeated up the maximum k which is when the coil centre is over the midpoint between poles.

V_{oc} is calculated by taking the gradient of the flux linkage, see Fig.(6.8).

6.4 Inductance

Due to the 3D nature of likely rotors, coils could be very short in the x-direction and so a 3D model was developed for the inductance calculation to take account of end effects. The end windings are assumed to be semicircular, and layout and parameters are shown in Fig.(6.9). The SLiM1 coils are an extreme example being cylindrical ie entirely composed of end windings. The Biot Savart method was used in conjunction with the method of images. Eq.(6.10) is the starting point:

$$d\mathbf{B_1} = \frac{\mu_0 I_1 \mathbf{dl_1} \wedge (\mathbf{r} - \mathbf{r}')}{4\pi|\mathbf{r} - \mathbf{r}'|^3} \tag{6.10}$$

Where $\mathbf{B_1}$ is the resultant field at position $\mathbf{r}$ from a current I_1 at position $\mathbf{r}'$, and $\mathbf{dl_1}$ is the unit vector in the direction of I_1.

The B_z component of the field from the current throughout the entire coil is calculated for a quadrant of the area contained by the coil ie the quadrant extends from $x = 0$ to $w_{co}/2$, $y = 0$ to $(w_{co} + l_c)/2$ and over the coil z depth. Because only

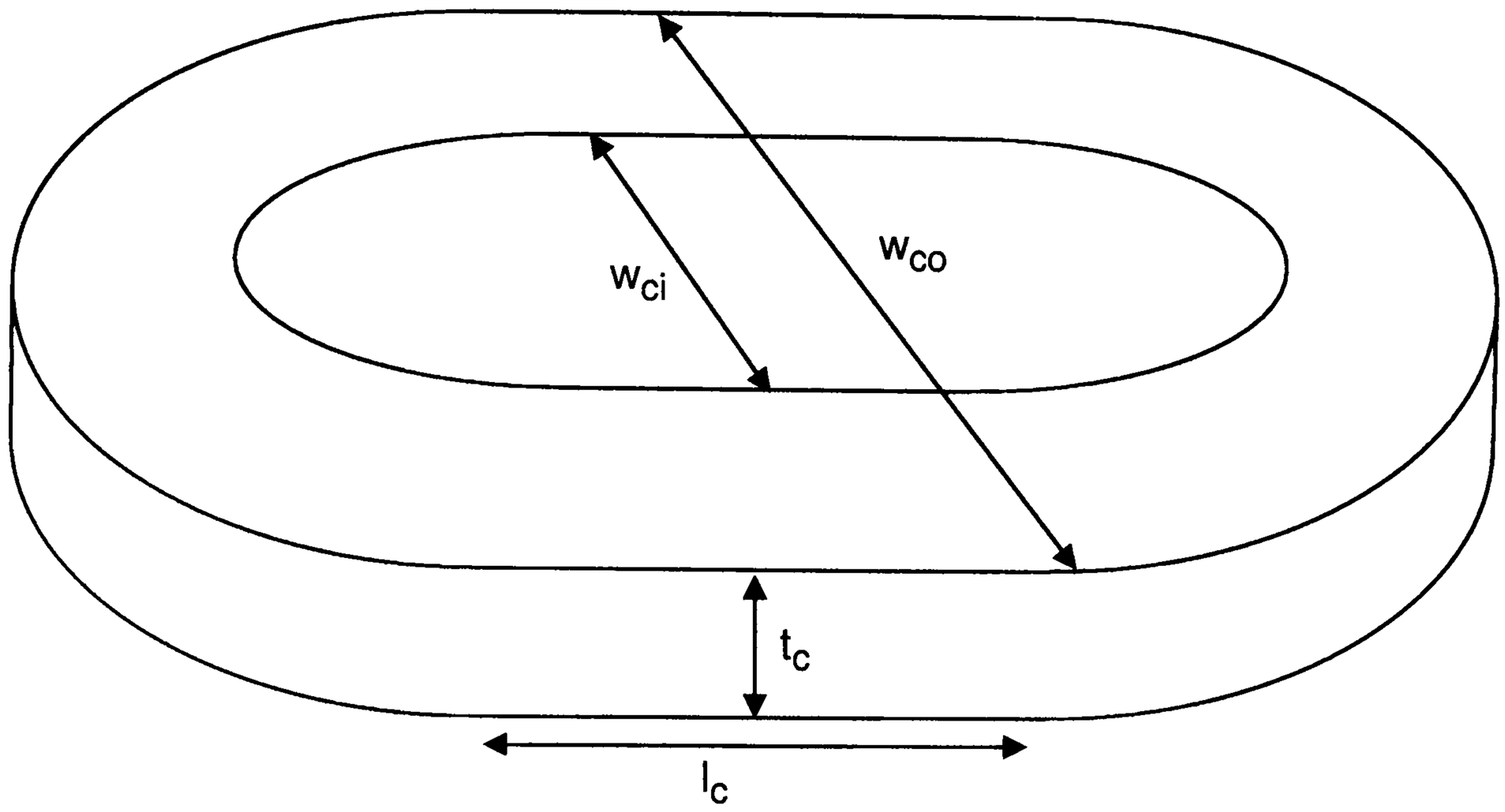

Figure 6.9: coil description

coils linear in z are being contemplated, the average over z is taken to get a single array in the xy-plane, which is then multiplied by element xy area and quadrupled as only one quadrant of the flux map was calculated for the coil. This was then multiplied by a Turns Function to get flux linkage.

For these calculations, a regular square grid was set up in the xy plane. Number of elements was chosen across half the coil inner width ie $w_{ci}/2$, from which element x and y size, δ, was defined. The coil outer width and length l_c were rounded to integer δ. Element z size, δ_z, was chosen separately.

Because the calculation is not performed for each individual turn on the coil, but is performed for many elements, I_1 of Eq.(6.10) has to be converted to a current density. If i is the current in the coil, and T_t is total turns, current density is:

$$J = \frac{T_t}{(w_{co}/2 - w_{ci}/2)\, t_c}\, i \qquad A/m^2 \tag{6.11}$$

Inductance is flux linkage per unit current, so if $i = 1$ in Eq.(6.11) then the elemental current flow which corresponds to coil current of 1A is:

$$I_1 = \frac{T_t\, \delta\, \delta_z}{(w_{co}/2 - w_{ci}/2)\, t_c} \tag{6.12}$$

Fig.(6.10)(a) shows the results for the SLiM1 coils, in isolation i.e. remote from any steel surface, with an increasing number of elements. The calculation gives an inductance of approximately 39mH. For comparison, the inductance of one of the

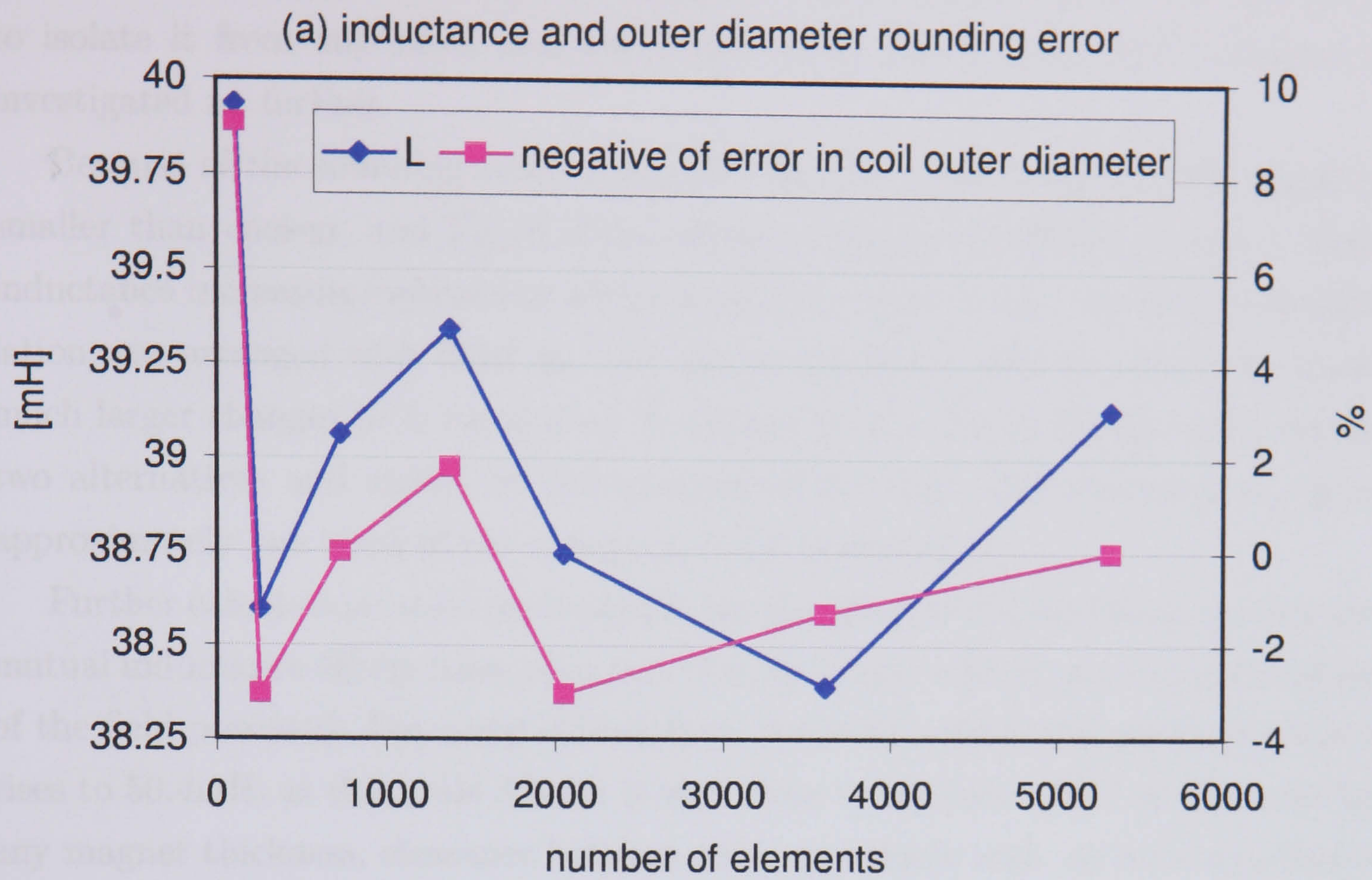

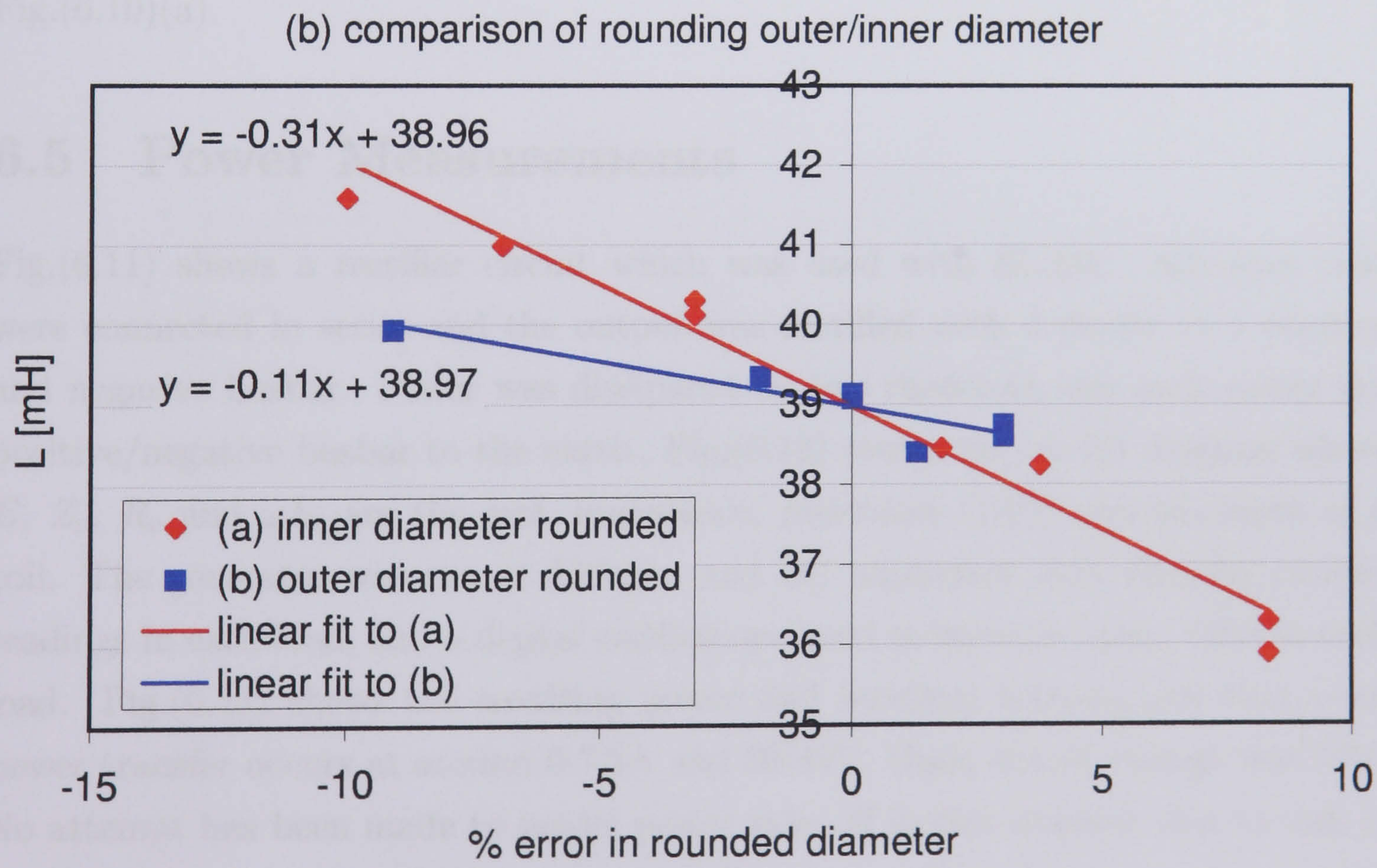

Figure 6.10: SLiM1 coil (isolated) inductance calculation details

SLiM1 coils was measured experimentally after removing the coil from the stator to isolate it from any steel, and was found to be 50mH. This 20% difference is investigated no further.

Because of the rounding error in w_{co} the coil is nearly always slightly bigger or smaller than chosen, and Fig.(6.10)(a) shows a strong correlation between them, inductance increasing/decreasing with increase/decrease in w_{co}. Initially, the calculation was arranged with fixed w_{co} and w_{ci} rounded, but this was found to create much larger changes in L for a given % change in w_{ci}. Fig.(6.10)(b) compares the two alternatives and shows by the gradient of the lines that rounding w_{co} gives approximately one third of the change in L c.f. rounding w_{ci}.

Further calculations were performed to see the effect of the steel rotor surface and mutual inductance effects from adjacent coils (by simply adding w_{co} to the x position of the field position). For a coil 3.5mm from the steel surface the model predicts L rises to 50.4mH, at this scale 3.5mm is very close to the rotor steel as this included any magnet thickness, clearance between rotor and stator and any former/adhesive to hold the coil together. For a coil remote from the rotor the mutual inductance from one neighbour is 0.8mH, and rises to 1.2mH when set 3.5mm from a steel surface. All these values are for 5324 elements ie the same as the last data point in Fig.(6.10)(a).

6.5 Power Measurements

Fig.(6.11) shows a rectifier circuit which was used with SLiM1. Adjacent coils were connected in series and the output was rectified with 2 diodes to a positive and negative busbar. Power was dissipated by two rheostats, one each across the positive/negative busbar to the earth. Fig.(6.12) shows the circuit diagram where E, Z_c, R_c and ωL_c are the emf, impedance, resistance (70Ω) and reactance of a coil. The generator was run at 319rpm, and DC ammeters were used for current readings in each load, and a digital oscilloscope used to measure mean volts in each load. Fig.(6.13) shows the resulting power and terminal voltage, and that peak power transfer occurs at around 6-7.5A and 30-40V. Open circuit voltage was 57V. No attempt has been made to model power take off in this manner, due to lack of time, and also as it is a fairly arbitrary choice of a variety of schemes. Due to the rectifier, the current is fed to the DC bus in pulses, conduction starting when $2E$ is greater than the DC bus voltage. For comparison, if the pairs of generator coils fed directly into a matched resistive load, and if coil resistance is neglected, the peak

power transfer occurs at $2E/\sqrt{2}$ (ie 40V). During loading at the higher currents the structure seemed to vibrate quite badly.

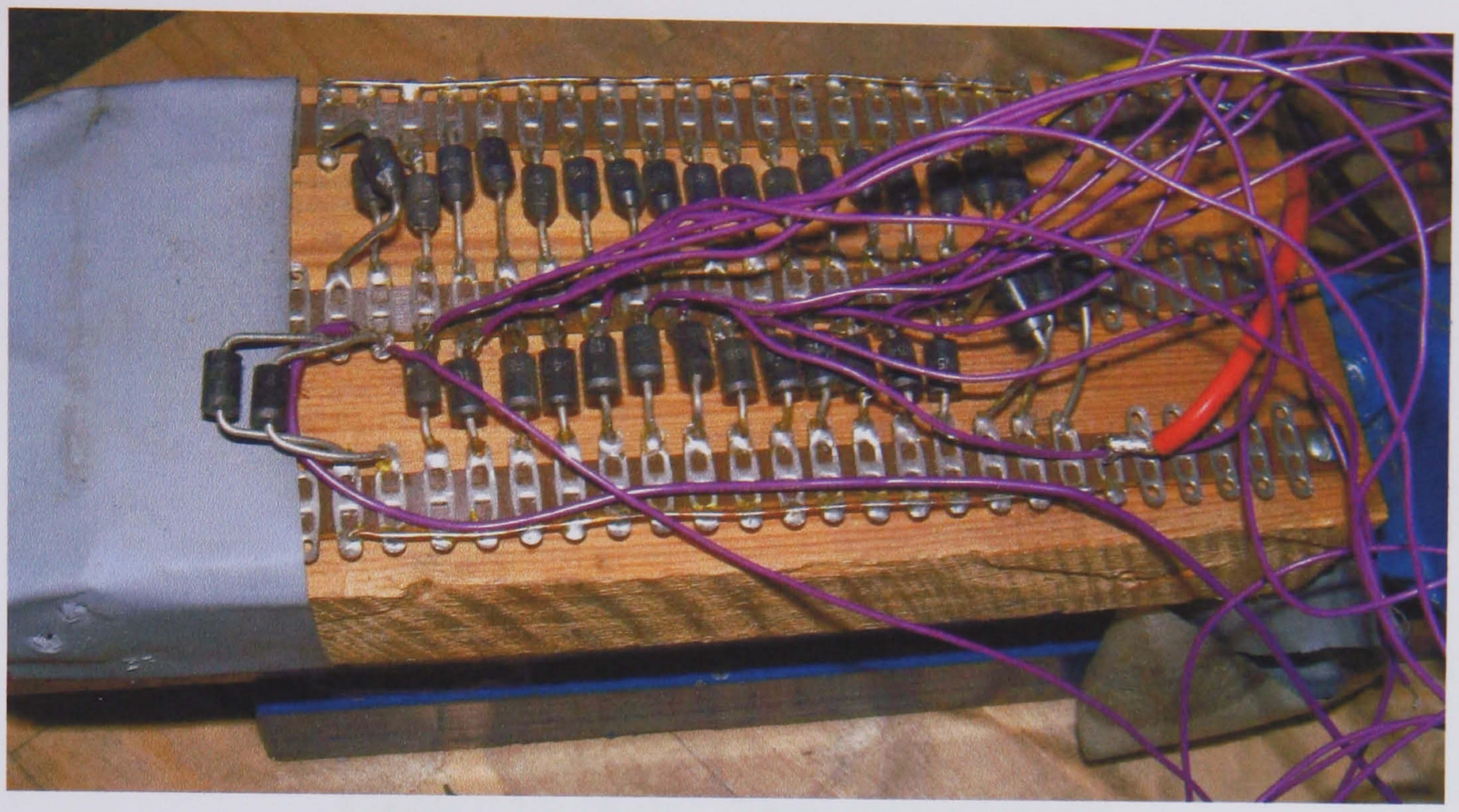

Figure 6.11: SLiM1 rectifier

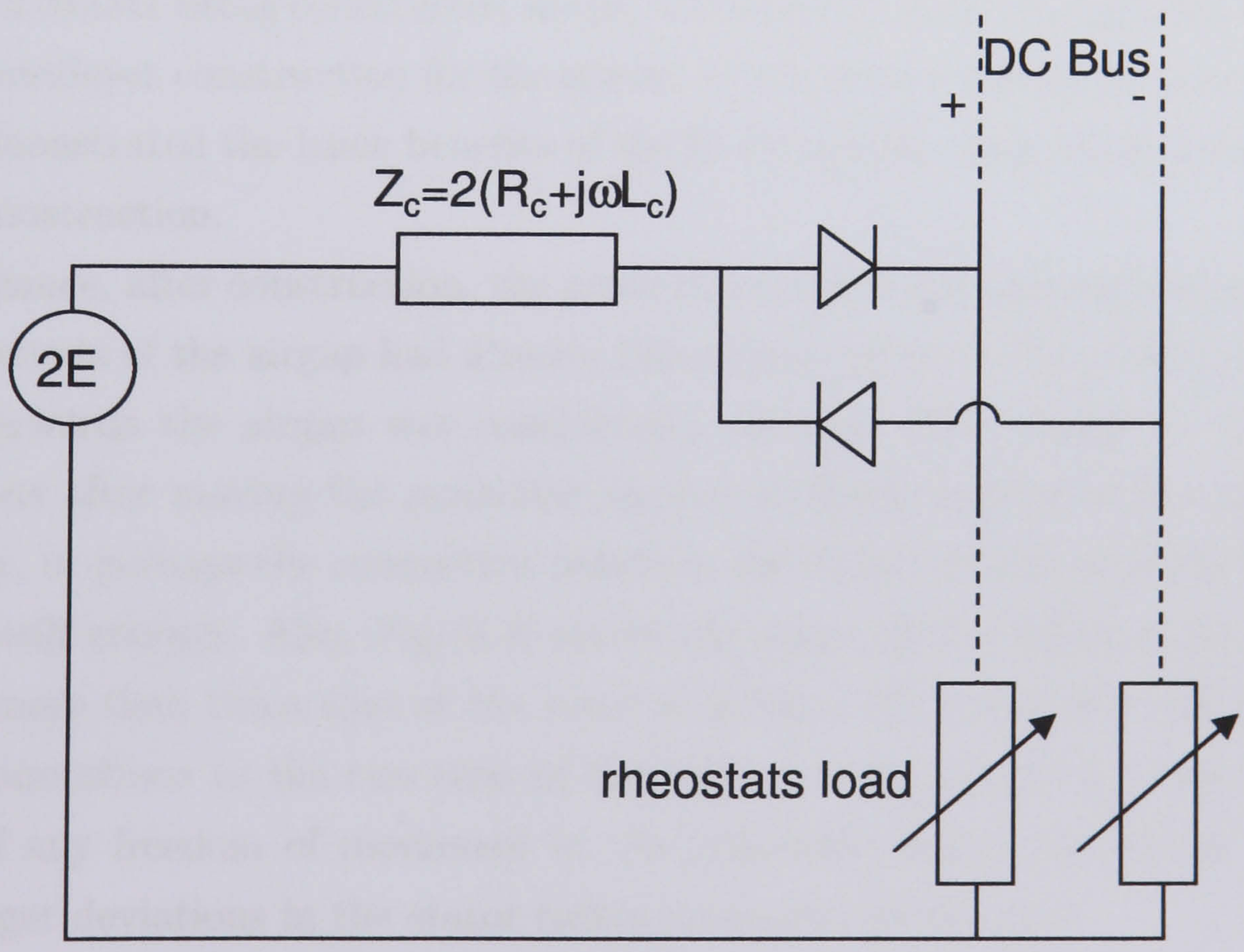

Figure 6.12: SLiM1 circuit diagram

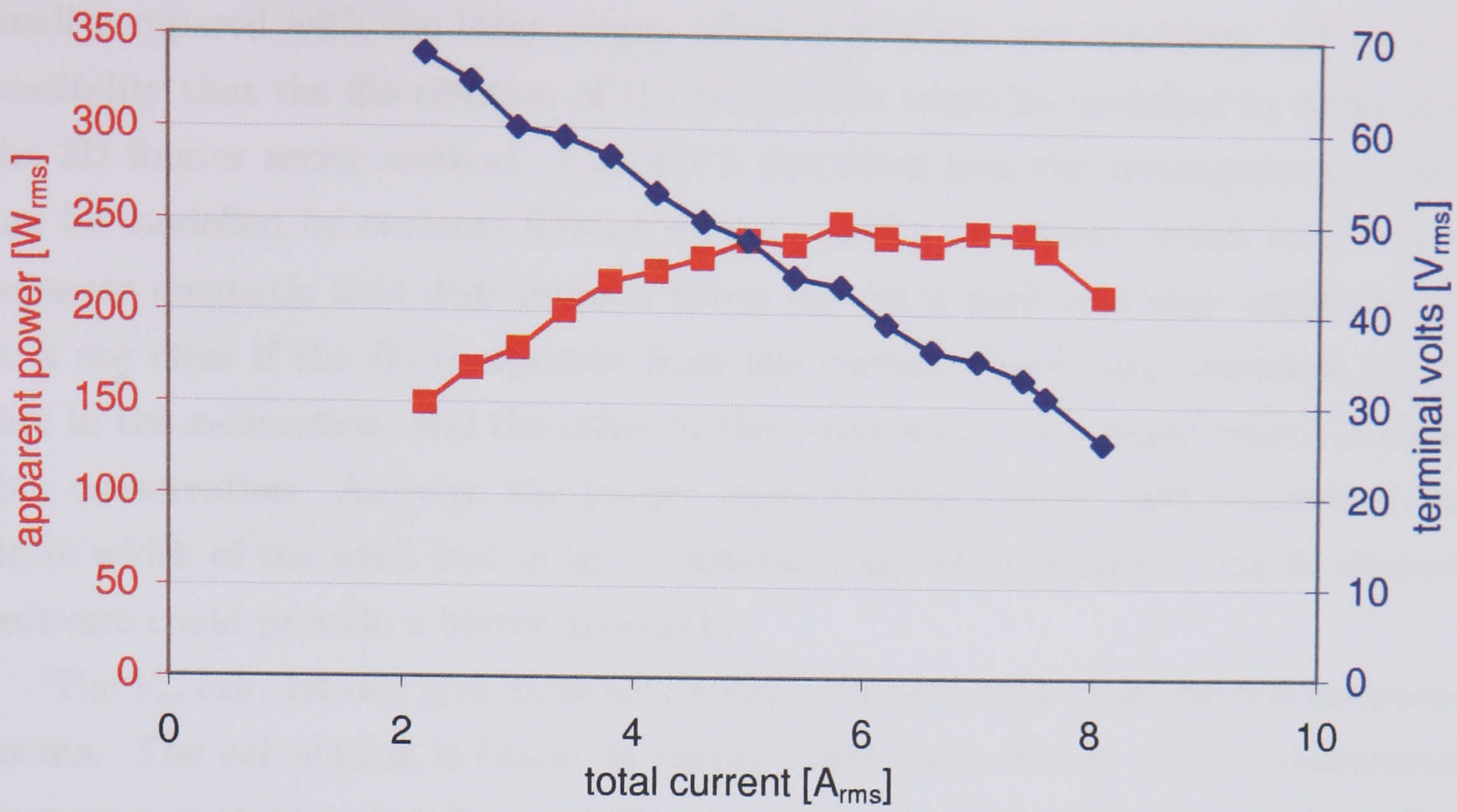

Figure 6.13: SLiM1 power measurements

6.6 Discussion & Conclusions

In spite of SLiM1 being constructed simply with bicycle wheel components and using a poor cantilever construction for the stator, it was robust enough to take power off it. It demonstrated the basic benefits of the SLiM design, these being lightness and simple construction.

By chance, after construction, the generator needed re-mounting. Because some measurements of the airgap had already taken place prior to this, it was discovered that afterwards the airgap was considerably altered. The change in the airgap dimensions after moving the generator implies multiple degrees of freedom in the generator, or perhaps the connection points to the frame, or also possibly the frame was not stiff enough. Also, Fig.(6.3) shows the range of the radius of the stator is 1.8mm, more than twice that of the rotor at 0.7mm. By inspection, the cantilever beams connections to the two rims of the stator are suspected of being the likely source of any freedom of movement in the generator, which also agrees with the much larger deviations in the stator radius compared to the rotor.

The assumption that the return flux in a 3D rotor is uniformly distributed should give a good estimate of the minimum back iron thickness required to avoid saturation. The field distribution adjusts to minimise the reluctance of the path, and hence saturation effects. Any increases in reluctance of the return flux path will be

small compared with the large airgap reluctance of air core machines. There is a possibility that the distribution of the return flux could be modelled by extending the 3D fourier series method. Chapter 5 described how the rectangular magnets can be modelled by currents flowing in the x and y directions, which lead to two separate magnetic field distributions above the rotor back iron that superimpose. It is not clear if the B_z component from one current distribution produces return flux in the x-direction, and the other in the y-direction. This might relate to some flux conservation. Anyway, the fourier series method cannot take account of the finite width of the back iron in the x-direction, and electromagnetic finite element software could provide a better approach.

The V_{oc} calculations give extremely good agreement with experimental measurements. The calculation is based on taking 2,500 terms for B_z as this guaranteed convergence at every point potentially swept by coils, but this still only takes a few seconds on a modern PC. The inductance calculations are more lengthy: for the 5324 elements used as a maximum there are 56 million calculations which takes 11 minutes on a recent PC. Also, due to the strong effect of the rounding of w_{co} it is hard to judge what is happening to the convergence.

The power tests flagged up the issue of vibrations in the SLiM structure, but it is not clear what was exciting the structure. With such a variable airgap, and especially with the ovalised stator, the structure could have been subjected to a rotating torque wave, which would be avoided in a better constructed machine.

Chapter 7

Case Study

Sufficient understanding has been gained to allow the design of a SLiM generator. A 2MW machine is chosen partly because at this size the existing direct drive generators are becoming heavy and large enough to create the sort of problems discussed in Section 1.3, and partly because the generator weight of the Enercon E66 2MW and the Zephyros Z72 1.5MW are known for comparison. Two different SLiM designs are presented, radius 20% & 35% of blade radius i.e. 14.3m and 25m diameter. Both use 2.8m diameter hubs ie 20/11% of the 14.3/25m SLiM respectively. This is to allow fair comparison without the unaccounted for hub weight/costs influencing results. The choice of 2.8m is arbitrary, as no check has been made on the cost versus size of this component. Because the impacts on converter designs etc of varying the voltage and frequency outputs of the SLiM are unclear, these were constrained to be approximately 1000 volts(rms) and 73Hz (ie 420 poles). Airgap (radial) length was chosen to be 10mm for the 14.3m SLiM on the basis that ±20% would be an acceptable airgap range, and ±2mm was estimated as the fabrication tolerance at this size. This compares with an airgap of 3mm for the 4m diameter Zephyros Z72. Therefore, for the 25m SLiM, this airgap was scaled up proportionally with radius to 17.5mm. Spoke rotations are set at the maximum possible for the spoke number, and is 4 for both SLiMs. Spoke number is set at 40, a guess at a compromise between fewer spokes with heavier rims, and more spokes and lighter rims.

7.1 Model Summary

The procedure is as follows:

- The power of a wind turbine can be estimated using

$$P = \frac{1}{2}\rho v_{\infty}^{3} C_p \pi R_{wt}^{2} \tag{7.1}$$

  where P=power, ρ=air density=$1.225kg/m^3$, v_∞=undisturbed upstream wind speed, taken as the rated wind speed, 13m/sec, C_p is the power coefficient, taken as 0.47, πR_{wt}^2 is the swept area, where R_{wt} is the blade radius. This, along with a tip speed ratio of 6 giving tip speed of 78m/sec of the wind turbine, defines the angular frequency:

$$\omega_{mech} = \frac{v_{tip}}{\sqrt{2P/\rho v_{\infty}^{3} C_p \pi}} \tag{7.2}$$

  From these the rpm and the torque required of the generator can be found, the latter from $P = T\omega_{mech}$.

- this torque can then be used in Eq.(4.23) to get spoke cross sectional area. σ_{push} and σ_{pull} are set at the reverse stress fatigue limit of steel, 224MN/m^2, and zero, respectively. Spoke rotation and spoke number is required for geometry. Eq.(4.2) gives the spoke length, so the spoke weight results.

- after choice of the magnet and coil arrangement, V_{oc} waveform and L are calculated by using the models developed in Chapter 6. Coil resistance is calculated in the usual way using coil dimensions and temperature corrected for operation at 60°C. A simple AC circuit constituting a single coil with inductance and resistance supplying a load resistance is adopted for the power calculation. The fundamental, V_1, is extracted from the V_{oc} waveform, I is set to correspond to 4A/mm^2 of copper, representing the coil thermal limit, and the power is calculated as:

$$P_{(rms)} = V_{1(rms)} I_{(rms)} cos\phi \tag{7.3}$$

  The correct power output is arrived at by trial and error adjustment of the magnet and coil arrangement.

- rotor back iron thickness model is calculated.

- the variation in the airgap can be calculated from Eqns.(4.24)&(4.25). and the rim section changed until this is acceptable. After this rim weight can be calculated

- the calculated hoop stress is checked against the buckling hoop stress, both models.

- the net radial field-current force is checked.

7.2 Discussion & Conclusions

Fig.(7.1) shows a breakdown of the weights of key components, where the rim weight column excludes the weight of the back iron, shown in a separate column. Fig.(7.2) shows some of the parameters for the two designs. Points of interest are:

- At approximately 17t, both designs show a drastic reduction in total weight over the existing Enercon and Zephyros machines which are 70t and 50t respectively.

- Whilst the 25m SLiM is the lightest, the difference between the two is not significant in view of the simplicity of the model, so the two SLiMs, even at such different diameters, have similar weights.

- Air gap area in the 25m SLiM is around 40% of the 14.3m SLiM

- Coil weights are very similar, with 25m SLiM coils having double the thickness

- Magnet weight for the 25m SLiM is around 25% less but the back iron weight is halved.

- Rim weights total (excluding back iron) is almost doubled in the 25m SLiM

- However, whilst rotor rim weight increases by around 50% in the 25m SLiM, the stator rim weight more than doubles.

Radial field current interaction forces are insignificant. The 25m SLiM stator rim approaches the critical buckling stress which is cause for concern, but a better understanding of the influences would probably allow this is to be addressed, by changing eg spoke number, rim stiffness, rim cross sectional area, noting that at present the airgap deviation allowed due to spoke tensions is equally shared between stator and rotor rim, but this is an unnecessary constraint.

A short hub length is desirable to limit shaft length and diameter and also tower bending moment. In practice the impact of airgap axial length is small compared with the hub length needed to give adequate spoke cone angle to allow the generator to survive storm wind loading. In the 14.3m diameter SLiM this hub length is 0.9m (c.f. 1.5m total hub length) i.e. 6% of generator diameter, but this rises to 3.3m (3.4m, 26%) for the 25m diameter SLiM. This is with a lateral deflection of 30mm, which leads to the downwind spokes detensioning by about two-thirds.

The simple power calculation used in the case study probably overestimates the power available from the machine. A time step simulation would be necessary for a complete solution to, for example, the simply rectified power circuit of Section 6.5. Many modern generators use active rectifiers to compensate for the voltage drop in the impedance of the generator windings. Due to absence of stator iron, the winding impedance can be small. For example, the 14.3m diameter SLiM has an inductance of 21.6mH which, at thermally rated current, gives a voltage drop of 7% of the fundamental coil voltage V1. This does not justify the expense of an active rectifier.

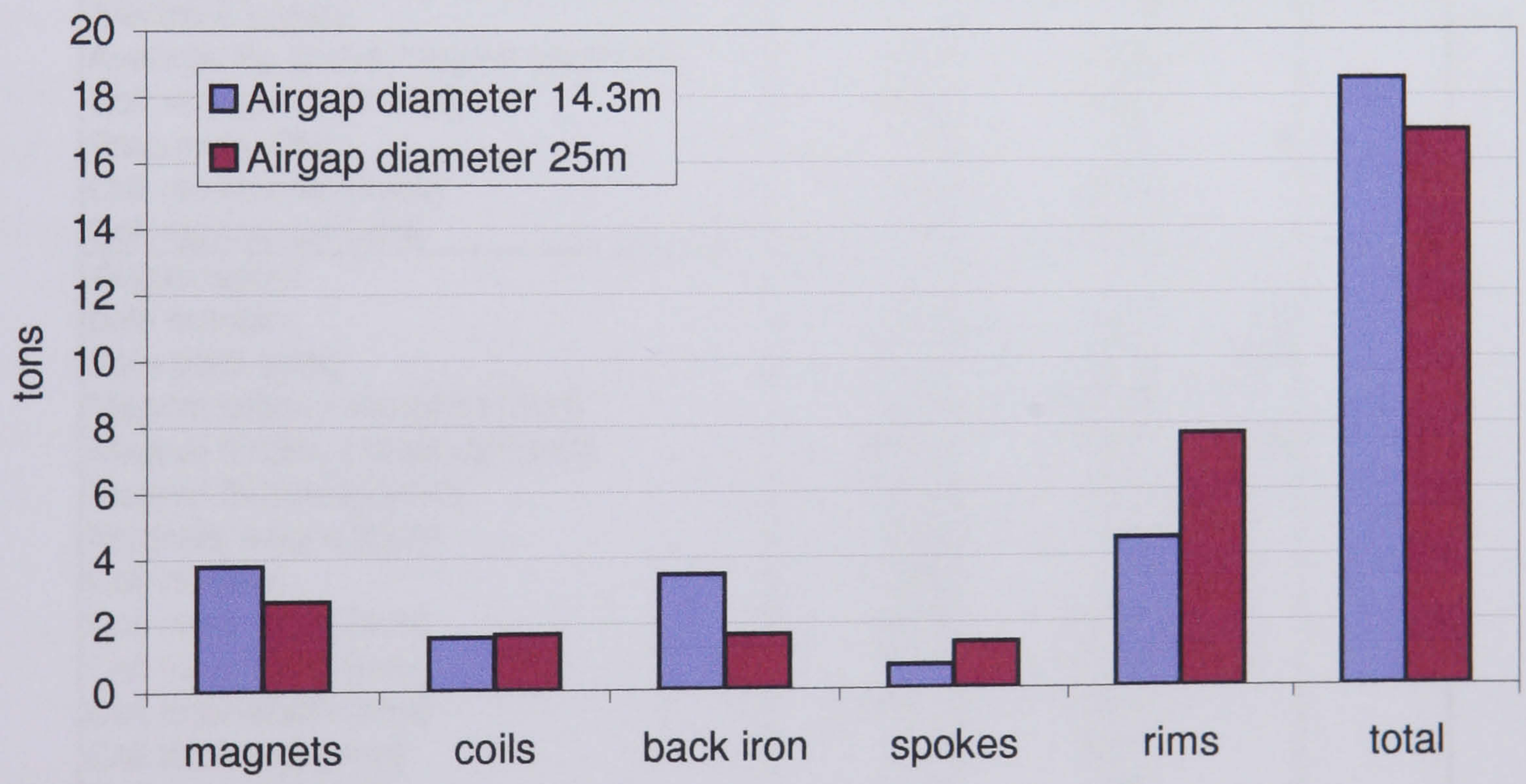

Figure 7.1: Comparisons of component weights for two SLiM diameters

Generator Type	**SLiM**	**SLiM**	**Z72**	**E66**
Output	2MW	2MW	1.5MW	2MW
rpm for this output	21	21	18	22
Airgap Diameter [m]	14.3	25.0	4	5
Structural				
Airgap [mm]	10.0	17.5	3	
Airgap tolerance [+/-mm]	2.0	3.5	0.2	
Spoke rotations	4	4		
Stator spoke number	40	40		
Stator spoke diameter	13.6	13.7		
Stator spokes weight [tons]	0.31	0.56		
Rotor tangential spoke number	20	20		
Rotor tangential spoke diameter [mm]	19.2	19.4		
Rotor tangential spokes weight [tons]	0.31	0.56		
Rotor radial spoke number	10	10		
Rotor radial spoke diameter [mm]	17.4	18.5		
Rotor radial spokes weight [tons]	0.11	0.23		
Stator rim depth [mm]	210	190		
Stator rim weight [tons]	2.94	4.21		
Rotor rim depth [mm]	119	129		
Rotor rim weight (excl. back iron) [tons]	1.6	3.5		
Generator axial length [m]	1.50	3.40	2	
Electro-Magnetic				
Average Bg above magnet centre [T]	0.27	0.28		
Coil voltage V1 [V rms]	1026	1040		
Frequency [Hz]	73	73	9	
Coil resistance [ohms]	2.67	2.81		
Coil inductance [mH]	21.6	50.6		
Airgap layout				
pole number	420	420	60	
Pole pitch [mm]	107.0	187.2	200	
Magnet width, x direction [mm]	85.6	149.8		
Magnet length, y direction [mm]	641.9	149.8	1200	
Magnet thickness [mm]	21.4	37.4		
Magnets weight [tons]	3.80	2.72		
Coil number	360	360		
Coil outer width [mm]	124.8	218.4		
Coil inner width [mm]	57.4	100.5		
Coil total length [mm]	706.1	218.4		
Coil thickness [mm]	17.0	29.7		
Coils weight [tons]	1.60	1.69		
Turns	180	550		
wire diameter [mm]	1.56	1.56		
Back iron thickness [mm]	15.44	18.09		
Back iron weight [tons]	3.47	1.66		
Total weight [tons]	**18.5**	**16.9**	**50**	**70**

Figure 7.2: Parameters of two designs for a SLiM 2MW

Chapter 8

Conclusions & Further Work

8.1 Conclusions

During investigations into the use of laser cut plate in segmental construction of direct drive generators, the structural stiffness and strength requirements, the weight penalty of providing these characteristics, the problems of building even airgaps, and the UMP consequences of this in single sided machines were all highlighted, although the issue of resonance and vibrations was not investigated, which could influence general stiffness requirements. Measurements of UMP in double sided airgap machines showed how large these were.

Using an ironless stator eliminates the costs, weights and eddy current losses associated with the laminated stator, adds to the costs and weights of the permanent magnets, drastically alters the coil requirements and introduces new forces due to the 3D field interaction with the coil current.

SLiM is a new machine structure that offers the potential of large reductions in machine weight with standard materials and low cost manufacturing. Combining it with an ironless stator eliminates the largest force acting on the structure, the airgap closing force.

Characterisation of the way the SLiM structure reacts to the important forces acting on it as a generator has been done, and models developed for the sizing of the rims, spokes and hub length. Field-current interaction forces have been investigated and a simple model has shown them to be small.

A novel 3D model has been developed for the field of a 3D permanent magnet rotor with an ironless stator, thorough experimental verification has shown the accuracy of the model. Convergence has been investigated to ensure appropriate use.

Models have been developed for the open circuit voltage and inductance in modular fractional pitch coils. These have been validated experimentally with the first demonstrator of the concept, SLiM1, which also gave valuable experience in the construction of these machines.

A 2MW case study draws on much of this work in order to find, primarily, the component weights of a large SLiM. This shows that SLiM designs can be 25 to 35% of the weight of existing direct drive generators.

8.2 Further Work

The case studies in no way represent optimised designs at the chosen radii, even if the value judgment were simply minimum weight. The large amount of variables lead to a considerable task in manipulating the various parameters to get the best design, Further work to gain a better understanding of the importance and effects of the various parameters could lead to quite different results to those presented.

No attempt has been made to assess vibration in the structure, or natural frequencies, which are of critical importance, and the 25m SLiM case study showed how it is possible to have buckling instability problems. Both these areas can be addressed in further work and designs can probably be adjusted to deal with them.

The design of SLiM was quite basic with simple rules governing for example rim cross section, and a simplified coil cross section. More detailed examination of the requirements and alternative designs might have significant impacts on the overall performance.

No attempt has been made to assess scaling of SLiM structures. This could give valuable guidance to any optimisation routines, and also highlight where best to apply the technology.

The role of tolerances has not been looked at for SLiM. Airgap tolerances could create problems in a machine in which the airgap field drops off so quickly and alters so drastically with distance from the rotor.

Whilst SLiM is promising to be much lighter than competing machines, it doesn't really solve the problems associated with size, and indeed SLiM might be better at bigger sizes. Manufacturing and assembly solutions will probably turn out to become a significant part of the SLiM concept.

With these large machines, the use of permanent magnets becomes extremely difficult, in spite of eliminating the rotor threading problems of traditional machines with ironed stators. Just transporting and fitting energized magnets to the rotor

iron poses significant problems including personnel safety issues. A possible solution is in-situ magnetisation after most of the generator has been assembled. This has been investigated in [21] and was deemed feasible.

Work is required to develop power take off systems for SLiM with an integrated approach to the design of the electromagnetics and the power converter.

References

[1] **BTM Consult**, I. C. Christensens All 1, DK-6950 Ringkbingpress, Denmark. release for 'International Wind Energy Development World Market Update 2002', http://www.btm.dk

[2] **British Wind Energy Association**, Renewable Energy House 1 Aztec Row, Berners Road London, N1 0PW, UK, http://www.offshorewindfarms.co.uk/seabed-area.html

[3] **Fathiyah, R., Mellot, R., Panagoda, M.**, 'Windmill Design Optimization Through Component Costing', MSc in Industrial Mathematics project report, Michigan State University, May 2001 referencing Grauers, A., 'Design of Direct-Drive Permanent Magnet Generators for Wind Turbines', PhD thesis, Chalmers University of Technology, Gothenburg, Sweden, 1996 http://www.mth.msu.edu/Graduate/msim/MSIMProjectReports/MCP1.May.2001.report.pdf

[4] **Spooner, E., Williamson, A.C., Catto, G.**, 'Modular Design of Permanent-Magnet Generators for Wind Turbines', IEE Proc.-Electr. Power Appl., Vol 143, No. 5, September 1996.

[5] **Spooner, E., Williamson, A.C., Thompson, L.E.**, 'Modular Construction of Large-Diameter, Multipole, Permanent-Magnet Machines', International Conference on Electrial Machines, Vigo, Spain, 1996

[6] **Gordon, P., Spooner, E.**, 'Segmental Construction of Large Modular Permanent-Magnet Machines', International Conference on Electrial Machines. Istanbul, Turkey, September 1998.

[7] **Gordon, P., Spooner, E.**, 'Segmental Construction of Large Modular Permanent-Magnet Machines', International Conference on Electrial Machines. Espoo, Finland, August 2000.

[8] **Hague, B**, 'The Principles of Electromagnetism Applied to Electrical Machines', Dover, 1962.

[9] **Gordon, P., Spooner, E.**, 'PM Machines with Ironless Magnetic Circuits'. 36th Universities' Power Engineering conference (UPEC 2001), Session 8B Electrical Machines III (electronic proceedings), University of Wales, Swansea, UK. September 2001

[10] **Bradley, D.**, 'Structural Analysis of Bicycle Wheels', Final Year Engineering Project Report, Engineering Dept., Durham University, South Rd, Durham, DH1 3LE, UK, April 1993.

[11] **Gavin, H.P.**, 'Bicycle-Wheel Spoke Patterns and Spoke Fatigue', Journal of Engineering Mechanics, Vol. 122, No. 8, p736-742, August 1996

[12] **Price, D., Akers, A.**,'Stiffness Characteristics of Bicycle Wheels', Bike Tech magazine Vol. 4, No. 3, June 1985.

[13] **Pippard, A.J.S., Francis, W.E.**, 'On a Theoretical and Experimental Investigation of the Stresses in a Radially Spoked Wire Wheel under Loads applied to the Rim', Philosophical Magazine Series 7, Vol. 11, No. 69, p233-285, February 1931

[14] **Pippard, A.J.S., Francis, W.E.**, 'The Stresses in a Wire Wheel under Side Loads on the Rim', Philosophical Magazine Series 7, Vol. 14, p436-445, February 1932 Aug. 1932

[15] **Pippard, A.J.S., White, M.J.**, 'The Stresses in a Wire Wheel with non-Radial Spokes under Loads applied to the Rim', Philosophical Magazine Series 7, Vol. 14 No. 90, p209-233, August 1932

[16] **Ryan, A.**, 'Structural Behaviour of a Bicycle Wheel', Final Year Engineering Project Report, Engineering Dept., Durham University, South Rd, Durham, DH1 3LE, UK, April 1995

[17] **Burgoyne, C.J., Dilmaghanian, R.**, 'Bicycle Wheel as Prestressed Structure', Journal of Engineering Mechanics Vol. 119, No. 3, p439-455, March 1993

[18] **Young, W.C., Budynas, R.G.**, 'Roark's Formulas for Stress and Strain' p319, 7th edition, McGraw Hill, 2002

[19] **Timoshenko, S.**, 'Theory of Elastic Stability', 1st edition, McGraw Hill. 1936

[20] **Burton, T., Sharpe, D., Jenkins, N., Bossanyi, E.**. 'Wind Energy Handbook', 1st edition, Wiley, 2001

[21] **Do Hyun Kang, Paul Curiac, Yeon Ho Jeong, Soo Jin Jung**, 'Prospects for Magnetization of Large PM Rotors: Conclusions From a Development Study', IEEE Transactions on Energy Conversion, Vol. 18, No. 3, p409-416. September 2003